UNIVERZITA KOMENSKÉHO V BRATISLAVE

FAKULTA MATEMATIKY, FYZIKY A INFORMATIKY

BARYÓN - ANTIBARYÓNOVÁ ASYMETRIA V CENTRÁLNEJ OBLASTI RAPIDITY NA LHC V EXPERIMENTE ALICE

Dizertačná práca

2012

Mgr. Michal Broz

COMENIUS UNIVERSITY BRATISLAVA

FACULTY OF MATEMATICS, PHYSICS AND INFORMATICS

BARYON – ANTIBARYON ASYMMETRY IN CENTRAL RAPIDITY REGION AT LHC WITH THE ALICE EXPERIMENT

PhD. Thesis

2012

Mgr. Michal Broz

UNIVERZITA KOMENSKÉHO V BRATISLAVE

FAKULTA MATEMATIKY, FYZIKY A INFORMATIKY

BARYÓN - ANTIBARYÓNOVÁ ASYMETRIA V CENTRÁLNEJ OBLASTI RAPIDITY NA LHC V EXPERIMENTE ALICE

Dizertačná práca

Študijný program: Jadrová a subjadrová fyzika

Študijný odbor: 4.1.5 jadrová a subjadrová fyzika

Školiace pracovisko: Katedra jadrovej fyziky a biofyziky

Školiteľ: prof. RNDr. Branislav Sitár DrSc.

Bratislava 2012

Mgr. Michal Broz

Abstrakt

Prvé zrážky protónov na urýchľovači LHC prebehli v období novembra – decembra 2009. Od vtedy sa na všetkých LHC experimentoch podarilo zozbierať veľké množstvo experimentálnych dát. Táto vzorka nám umožňuje skúmať čoraz exotickejšie častice. Napriek tomu že ALICE experiment bol navrhnutý hlavne na skúmanie fyziky ťažkých iónov, má aj bohatý program pre fyziku protón protónových zrážok. Hlavné charakteristiky ALICE detektora sú malé množstvo materiálu v detektore, schopnosť merania v oblasti nízkych priečnych hybností, výborná identifikácia častíc a kvalitné meranie interakčného vertexu.

V tejto práci popisujem výsledky analýzy protón-protónových zrážok pri rôznych energiách zrážok na LHC (√s = 900 GeV, 2.76 TeV and 7 TeV). Zameriavam sa na meranie pomeru baryónov k antibaryónom v centrálnej oblasti rapidity, ktoré je dôležité pre popis prenosu baryónového čísla v rapidite a môže nám niečo povedať o nositeľovi baryónového čísla ako aj o samotnej štruktúre baryónu. Konkrétne pomery $\bar{p}/p$, $\bar{\Lambda}/\Lambda$, $\overline{\Xi^+}/\Xi^-$ a $\overline{\Omega^+}/\Omega^-$budú prezentované ako funkcia rapidity, priečnej hybnosti a multiplicity nabitých častíc v interakcii. Výsledky porovnám s predpoveďami viacerých teoretických modelov. V závere bude diskutovaná závislosť antibaryón-baryónového pomeru v centrálnej oblasti rapidity na energii zrážky a podivnosti skúmaných baryónov.

Abstract

The Large Hadron Collider (LHC) provided the first proton-proton collisions in the period of November-December 2009. Since then, a large data sample has been recorded by all LHC experiments. This event sample allows us to study more and more exotic particles and events. The ALICE (A Large Ion Collider Experiment) experiment, though designed primarily to study heavy ion collisions, has a rich proton-proton physics program. The characteristic features of ALICE are its very low-momentum cut-off, the low material budget and the excellent particle identification (PID) and vertexing capabilities.

In this thesis, I discuss the results from the analysis of proton-proton collisions at the different LHC energies ($\sqrt{s}$ = 900 GeV, 2.76 TeV and 7 TeV). I concentrate on the antibaryon-to-baryon ratio study which is of great importance for description of baryon number transport and it can allow to determine the carrier of the baryon number as well as to give an information on baryon structure itself. In particular, the multiplicity, rapidity and transverse momentum dependence of the $\bar{p}/p$, $\bar{\Lambda}/\Lambda$, $\overline{\Xi^+}/\Xi^-$ and $\overline{\Omega^+}/\Omega^-$ ratios will be shown. The results will be compared with different theoretical predictions. Finally, the energy and strangeness dependence of the mid-rapidity ratios will be presented.

Contents

List of Tables

Introduction

It is not obvious which partons in the proton carry its baryon number. In model where the baryon number of the incident baryon is associated with valence quarks and transferred to a more central rapidity region by diquark exchange the mechanism is attenuated exponentially with the rapidity interval over which the baryon charge is moved. Alternatively, when baryon number is carried by gluonic field, baryon number flow can be rapidity independent due to a purely gluonic mechanism. When the baryon number is carried by gluons, there can be nonzero asymmetry in central rapidity. This is accounted for models where the three valence quarks of the proton are fragmented independent but are joined by strings to a baryonic gluon field configuration, the so-called string junction. These two theories can be tested experimentally by measuring the antibaryon-baryon asymmetry in central rapidity region.

ALICE has several features that make it an important contributor to proton–proton physics at the LHC. Its design allows particle identification over a broad momentum range, powerful tracking with good resolution from 100 MeV/c to 100 GeV/c, and excellent determination of secondary vertices. These, combined with a low material budget and a low magnetic field, will provide unique information about low-pt phenomena in pp collisions at the LHC.

The first chapter is dedicated to brief summary of present knowledge of baryon number nature. Two models of baryon structure are described and several processes of baryon number transfer in high enegy collision driven by these models are disscused. In this chapter I am describing a motivation for study of various properties connected to baryon number transport.

The second chapter is giving an outlook of experimental aparatus used in this measurement - the ALICE detector. Various detector subsystems are desribed and part of the chapter is dedicated to track reconstruction and particle identification procedures used after the measurement.

Detailed description of analysis procedure is placed in the chapter number three. Procedure to extract uncorrected yields for four baryon species and technical details connected to background are described in the first part. The second part is dedicated to

corrections which were used to emend the systematical effects caused by differences of the interaction cross sections for baryons and antibaryons and nuclei.

Results – the fully corrected antibaryon-to-baryon ratios for four baryon species as a function of rapidity, transverse momentum, and the mid-rapidity ratios as a function of strangeness, rapidity interval and charged particle multiplicity are presented in the last chapter.

1 Baryon number

1.1 Carrier of baryon number

It is not obvious which partons in the baryon carry its baryon number. In QCD, quarks carry color, flavor electric charge and isospin. Naive approach leads to association of baryon number with valence quarks. This consequence comes from the definition of baryon number of hadronic system. The definition is:

D: Baryon number of hadronic system is given by the number of quarks minus number of antiquarks divided by three.

Experimental fact is that baryon number is conserved in closed system. Density of valence quarks in a baryon of flavor *i* carrying a momentum fraction *x* is defined as

$$q_i^v(x) = q_i(x) - \overline{q_i}(x), \qquad (1.1)$$

then

$$\sum_i \int_0^1 dx\left(q_i(x) - \overline{q_i}(x)\right) = \sum_i \int_0^1 dx.q_i^v(x) = 3, \qquad (1.2)$$

this also motivates the association of baryon number with valence quarks. However, this later assumption is not dictated by the structure of QCD, and therefore does not to need be true.

It looks pretty clear and right, but let`s look on this reaction

$$\pi^- + p \to \Omega^- + K^+ + 2K^0, \qquad (1.3)$$

you can see that baryon number is conserved in the reaction. Quark diagram for this reaction is:

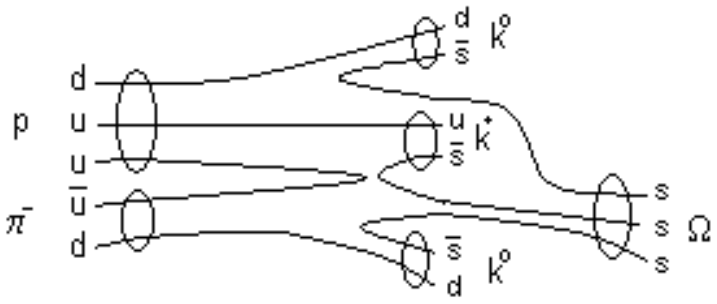

Figure 1.1: Quark diagram for process (1.3). None of incident quarks appear in final baryon

as you can see none of the valence quarks in the initial proton appear as valence quark in Ω^- . Thus baryon number must be carried by the other partons in the proton: gluons.

Another example which creates doubt that valence quarks carries baryon number is central collision of heavy ions. What happens through the collision? Substantial faction of colliding nuclei is stored in the valence quarks. We know that energy loss of quark propagating through a heavy nucleus is small and energy independent [1] [2] [3]. The number is $\Delta E \approx 10 GeV$. So, high energy quark cannot be stopped by soft interaction. The valence quarks pass through the collision region losing only small fraction of their energy on gluon radiation by soft collisions. So, if valence quarks are carriers of baryon number, they will sweep the baryon number to fragmentation region. Many softer quark - antiquark pairs and gluons are left behind. After propagation through a heavy nucleus the initial valence quarks completely lose their identity as nucleon constituent. The fragmentation jets are created which consist mostly of mesons and a small number of baryon - antibaryon pairs. Therefore the baryon number carried by colliding nuclei is not to be found in the beam fragmentation region but is stuck in collision region. As you can see something is wrong.

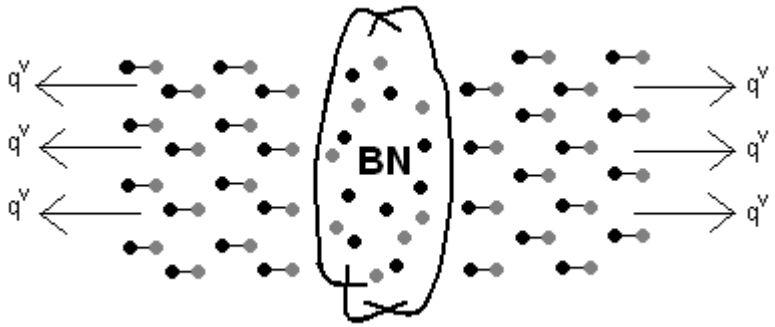

Figure 1.2: Picture illustrating final state folowing central collision of reativistic heavy nuclei. Grey and black circles coresponds to quarks and antiquarks. The valence quarks q^v escaping the collision region produced jets. Baryon number (BN) remains in collision

The valence quarks readily survive this collision and remain in fragmentation regions while baryon number does not. Because the baryon number is stopped along with gluons it appears that gluon may carry the baryon number.

1.2 Nature of baryon number

1.2.1 The string configurations of the color fields in hadrons

The string configurations of the color fields in meson and in baryon are quite different. A meson looks like a quark - antiquark pair connected by a color flux tube [1]. Quark and antiquark are in state of color triplet, antitriplet respectively. The final color state of this configuration is given by color algebra:

$$\{3\} \otimes \{\bar{3}\} = \{1\} \oplus \{8\}, \qquad (1.4)$$

where the color singlet is realized in nature. This fact is known as confinement of quarks in hadrons.

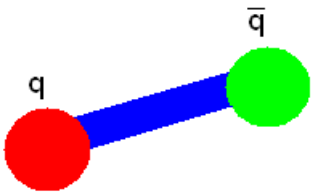

Figure 1.3: String configuration of a meson

Two models of baryon structure were developed in the past. The first one Constituent quark model [4] introduced the baryon as quark-diquark pair. In this model the valence quarks are carriers of baryon number, each valence quark has BN=1/3. Gluons are without baryon number. Diquark in this model is solid structure and can't be divided in the collision.

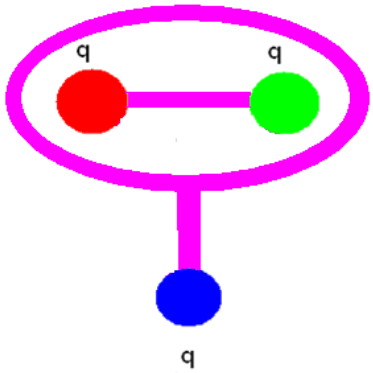

Figure 1.4: String configuration of a baryon in the constituent quark model: quark – diquark pair.

In the string junction model [5], configuration of strings in baryon having minimal energy has a form of the Mercedes - Benz star and the point where the strings joint is called the string junction [6]. One can imagine the parton cloud of a valence quark as quark - antiquark chain. In the baryon this valence quark is accompanied by valence diquark. The valence diquark is in a state of color antitriplet what is given by following equation

$$\{3\} \otimes \{3\} = \{\bar{3}\} \oplus \{6\}. \qquad (1.5)$$

So the color state of diquark is the same as color state of antiquark. Diquark is accompanied with quark in a state of color triplet and final color state is also given by (1.4).

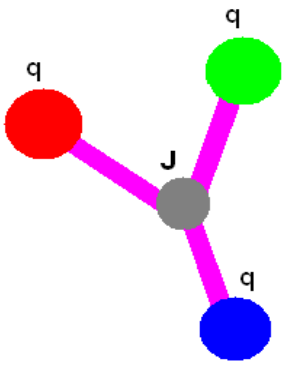

Figure 1.5: String configuration of a baryon in the string junction model. The point where the strings joint is called string junction (J).

In string junction model, the baryon number is carried by string junction. So for the valence quarks BN = 0 and for the string junction BN =1.

This was stable color states of baryon. Let`s look on the color states which can be created in hadronic collisions. As one can see from full baryon color decomposition also another color states are available

$$\{3\}\otimes\{3\}\otimes\{3\}=\{1\}\oplus\{8\}\oplus\{10\}. \qquad (1.6)$$

These color state can be created in higher Fock components of baryon since Fock state decomposition of baryon contains components with few sea quark - antiquark pairs

$$|B\rangle=|3g^{v}\rangle+|3g^{v}q^{s}\bar{q}^{s}\rangle+|3g^{v}2q^{s}2\bar{q}^{s}\rangle..., \qquad (1.7)$$

where color degrees of freedom of the sea quarks allow the valence configuration in non - singlet state. Interesting are these states: color octet and color decuplet.

1.2.2 Annihilation of baryon number

Experiments on baryon number annihilation via $p+\bar{p}\to mesons$ were carried out in 1970. Important conclusion is that if baryon number is associated with gluonic configuration, it will be rather uniformly distributed in rapidity and that the $p\bar{p}$ annihilation cross section will not vanish at high energy.

The first claim that the $p\bar{p}$ annihilation cross section is energy independent at high energies was made by Gotsman and Nussinov [7]. They employed a string junction model, and suggested that annihilation results from the overlap of gluonic string junction a string

antijunction followed by rearrangement of the gluonic strings as is illustrated in Figure 1.6. They made a natural assumption that this process is energy independent in analogy to non-annihilation collisions corresponding to crossing of the strings. The annihilation cross section was estimated by assuming that string junction has a size of the order of the transverse dimension of the strings ~ *0.2 - 0.3 fm*. With this assumption they found $\sigma_{ann}^{\bar{p}p} \approx 1-2mb$.

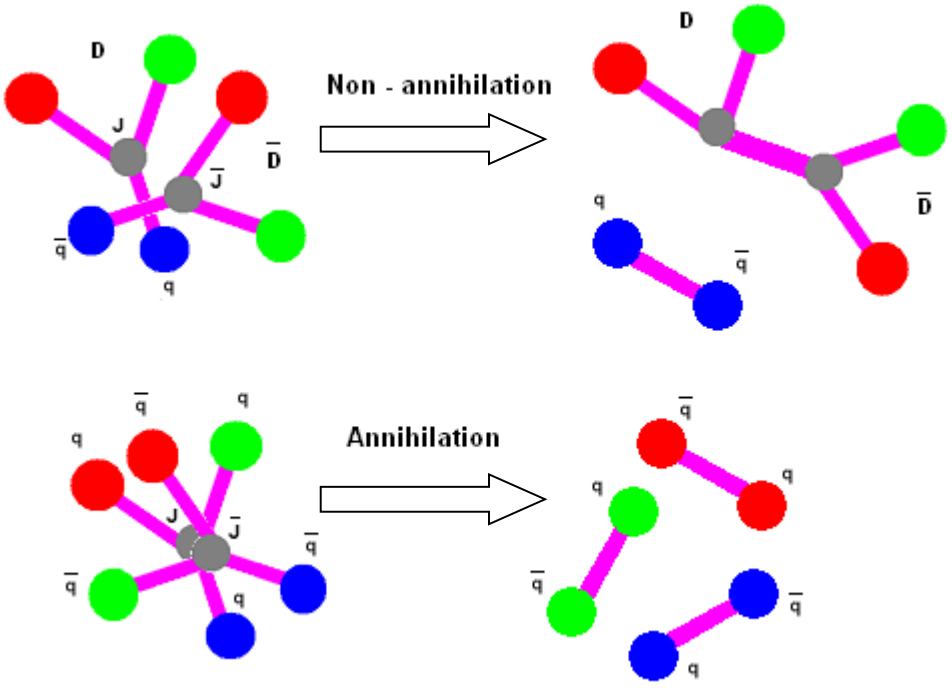

Figure 1.6 : Picture shows interaction of a baryon consisted of diquark (D) and a quark with antibaryon. Crossing of the strings in the impact parameter plane leads to non - annihilation final state with two strings. Annihilation corresponds to overlap of string junction (J) with string antijunction (J) leading to three string production

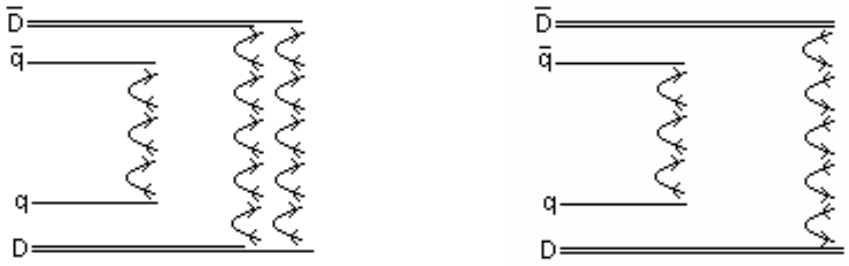

Figure 1.7: Baryon - antibaryon interaction once again. Picture shows three string final state which leads to annihilation (left) and two string, non - annihilation final state (right).

1.3 Baryon number transport

In inelastic non-diffractive proton-proton collision at very high energy, the incoming projectile breaks up into several hadrons that typically emerge, after the collision, at small angles close to the original beam direction. The deceleration of the incoming proton, or more precisely of the conserved baryon number associated with the beam particles, is often called ‘‘baryon-number transport’’ and has been debated theoretically for some time [5], [6], [10-15].

Most of the (anti-) baryons at midrapidity is created in baryon-antibaryon pair production, implying equal yields. Any excess of baryons over antibaryons is therefore associated with the baryon-number transfer from the incoming beam. Note that such a study has not been carried out in high-energy proton-antiproton colliders (SpS, Tevatron) because of the symmetry of the initial system at midrapidity.

There is a possibility to investigate baryon transport over very large rapidity intervals by measuring the mid-rapidity antibaryon-to-baryon asymmetry, which can be defined as

$$A_{BN}(y) = \frac{N_{BN} - N_{\overline{BN}}}{N_{BN} + N_{\overline{BN}}}, \qquad (1.8)$$

where $N_{BN}, N_{\overline{BN}}$ is the density of produced baryon, antibaryon number which is a function of rapidity *y*. Asymmetry is talking about absolute difference between baryons and antibaryons. Corresponding variable for relative difference is antibaryon-to-baryon ratio, which can be defined as

$$R_{BN}(y) = \frac{N_{\overline{BN}}}{N_{BN}}. \qquad (1.9)$$

Both variables are equivalent and the relation is the following

$$A_{BN}(y) = \frac{N_{BN} - N_{\overline{BN}}}{N_{BN} + N_{\overline{BN}}} = \frac{1 - \frac{N_{\overline{BN}}}{N_{BN}}}{1 + \frac{N_{\overline{BN}}}{N_{BN}}} = \frac{1 - R_{BN}}{1 + R_{BN}}. \qquad (1.10)$$

The baryon number transport can be described in the framework of Regge phenomenology [23] with using the two baryon models described in section 1.2.1. In this framework the probability to transfer the baryon number over rapidity interval Δy is [10]

$$\propto \sqrt{s}^{\alpha-1} \approx e^{(\alpha-1)\Delta y} \qquad (1.11)$$

where $\Delta y = y_{beam} - y_{baryon}$ and α is a constant which depends on the configuration in which the baryon number is transported and is identified in the Regge model as the intercept of the trajectory for the corresponding exchange in the *t* channel.

A kinematical explanation can be given for the baryon stopping in high energy collision. Let`s consider an ultra - relativistic proton-proton collision in its center - of - mass frame, which coincides with the lab frame in collider experiments.

At sufficiently high energies, the valence quark distribution will be Lorentz - contracted to thin pancakes with thickness

$$z_V \cong \frac{1}{x_V P}, \qquad (1.12)$$

where *P* is the c. m. momentum in the collision, and $x_v \sim 1/3$ is a typical fraction of the proton`s momentum carried by valence quark. The typical time needed for the interaction of valence quarks from different protons with each other during collision is given by the characteristic interquark distance in impact parameter plane,

$$t_{\text{int}} = const \approx 1\,fm. \qquad (1.13)$$

However, the time available for this interaction in the collision is only

$$t_{coll} \approx z_V \cong \frac{1}{x_V P}, \qquad (1.14)$$

It is therefore clear that at sufficiently high energies when $t_{coll} << t_{int}$, the valence quarks of the colliding protons do not have time to interact during collision and go through each other, populating the fragmentation regions.

In the composite quark model diquark is solid structure and cannot be broken. As a consequence the final baryon is produced around this diquark every time, the baryon number is transported in the diquark configuration [8], [9]. This is the only one existing process in composite quark model. Only one string can be broken in this model. Diquarks in general retain a large fraction of the proton momentum and therefore stay close to beam rapidity, typically within one or two units, as dictated by negative value of α for diquark configuration and also motivated by formulas (1.13) and (1.14). Therefore, additional processes have been proposed to transport the baryon number over larger distances in rapidity. These processes took place in string junction model.

In the string junction model we have a possibility to break one, two or even all the three strings. This leads to two additional processes.

In the string junction model, the baryon number is carried by string junction [5], [6], [10]. The string junction contains an infinite number of gluons which therefore by virtue of momentum conservation should carry on the average an infinitely small fraction $x_s << x_v$ of the proton`s momentum. We therefore expect that the string junction configuration may not be Lorenz contracted to a thin pancake even at asymptotically high energies, since

$$z_S \cong \frac{1}{x_S P} >> z_V . \qquad (1.15)$$

In this case the string junction will always have enough time to interact, and we may expect to find stopped baryons in the central rapidity region even in a high energy collision. The last process when all three string are broken and final baryon is created around string junction with presence of three sea quarks is often called “pure gluonic” process [11-13] because all the valence quarks were moved away.

α ≈	
Diquark (CQM)	-1/2
SJ accompanied by diquark	-1/2
SJ accompanied by quark [10] [14]	1/2
SJ itself [10] [13]	1/2
SJ itself [11], [12]	1

Table 1.1: α values for different processes in string junction and composite quark model of a baryon. Two values for SJ itslef process coresponds to different teoretical predictions

Considering the string junction model of the baryon, two marginal values of J were debated for pure gluonic process of baryon number transport. These two concepts result in a significantly different BN distribution with rapidity (BN transport), when the proton interacts inelasticaly at high energies.

- If we take the α for pure gluonic process close to 1, then the process is not or just slightly suppressed at large values of Δy and as a consequence we can see non-zero asymmetry at high energies. The value equal to unity induce antibaryon-to-baryon ratio converging at high energies to non-unity value [12].

- Another possibility is that α = 0.5. This induces vanishing baryon number transport and antibaryon to baryon ratio at 7 TeV close to unity. This topic will be discussed in detail in chapter 1.4.1.

Why then is the leading baryon effect of gross feature of high - energy *p-p* collisions? The reason may be following: The string junction, connected to all three of the valence quarks, is confined inside baryon, whereas proton-proton collisions become on the average more and more peripheral at high energies. Therefore in typical high - energy collision, the string junctions of the colliding baryons pass far away from each other in the impact parameter plane and do not interact. One can however select only central events, triggering on high multiplicity of the produced hadrons. In this case, we expect that the string junctions will interact and may be stopped in the central rapidity region. Even at very high energies there can be more baryons than antibaryons.

Let's have a look on the diagrams for different processes in proton-proton collisions. As we said before, for constituent quark model, we have only one process and final baryon(s) are formed around the diquarks. There can be also pair production of baryon/antibaryon pairs, but this is of course BN symmetric.

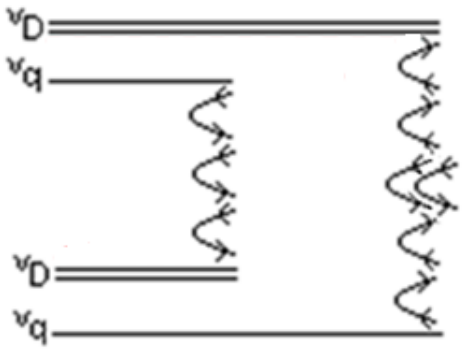

Figure 1.8: Quark diagram with one string breakage process in composite quark model in proton-proton collision. Baryon pair production on broken string is shown here.

In string junction model we have similar process for string junction connected to diquark. Diagram looks similar

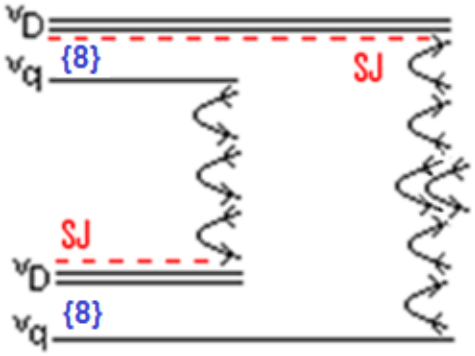

Figure 1.9: Quark diagram of proton-proton collision showing baryon number transport with string junction model. Valence quarks of both baryons are in color octet state and BN is transported in diquark-string jucntion configuration

Incident protons are in this case in color octet state and diquark is in color inti-triplet state.

Another possible event diagram is on Figure 1.10. Both incident protons are again in color octet state, but one of the diquarks turn into sextet state. String junction is in this case for upper proton accompanied with quark only and final baryon is made of one valence and two see quarks.

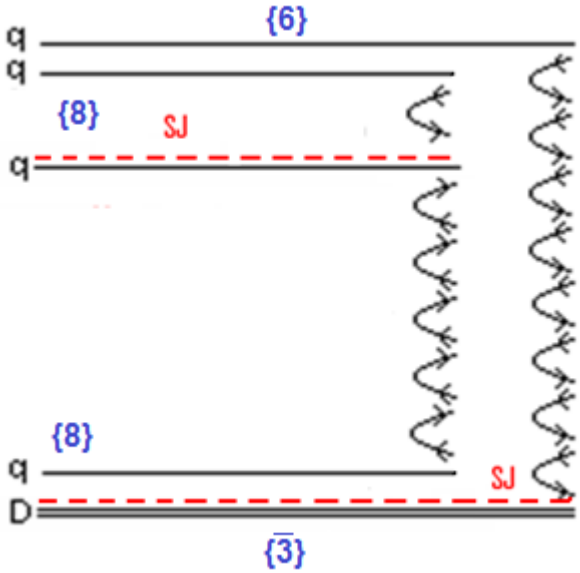

Figure 1.10: Quark diagram of proton-proton collision showing baryon number transport with string junction model. Valence quarks of both baryons are in color octet state, but the diquark of upper baryon turned to sextet color state. BN is transported in quark-string junction configuration (upper) and diquark-string jucntion configuration (lower)

Lower proton is in the same state as before, so the second string junction is accompanied by a diquark.

The last process is shown in the diagram on the Figure 1.11. The upper proton is in state of color decuplet and all three valence quarks are free and string junction is transporting baryon number by itself. Final baryon is formed around string junction from sea quarks.

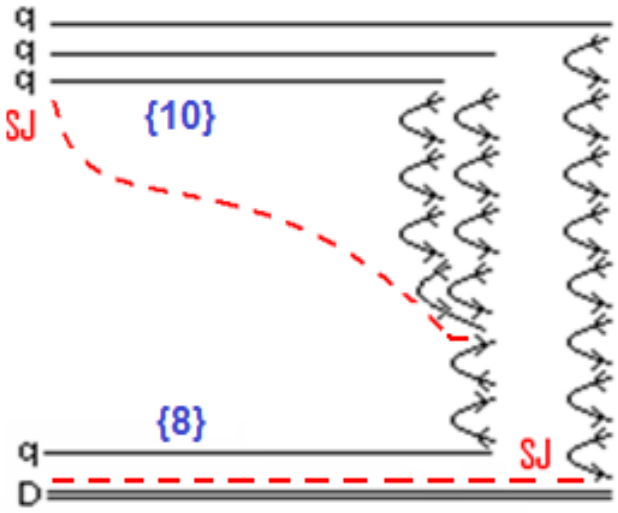

Figure 1.11: Quark diagram of proton-proton collision showing baryon number transport with string junction model. Valence quarks of upper baryon are in color decuplet state. BN is transported in string junction-itself configuration (upper) and diquark-string jucntion configuration (lower)

Lower quark is again in color octet state, but in the collision we can have all possible combinations of the processes. This means that there are three other diagrams for proton-proton collisions which are not figured here.

1.3.1 Parameterization of rapidity interval dependence of antibaryon-to-baryon ratio

A rough approximation of the Δy dependence of the ratio R can be derived in the Regge model, where baryon pair production at very high energy is governed by Pomeron exchange and baryon transport by string-junction exchange [13]. The relevant diagrams that contribute to the production of both antibaryons and baryons are given in Figure1.12.

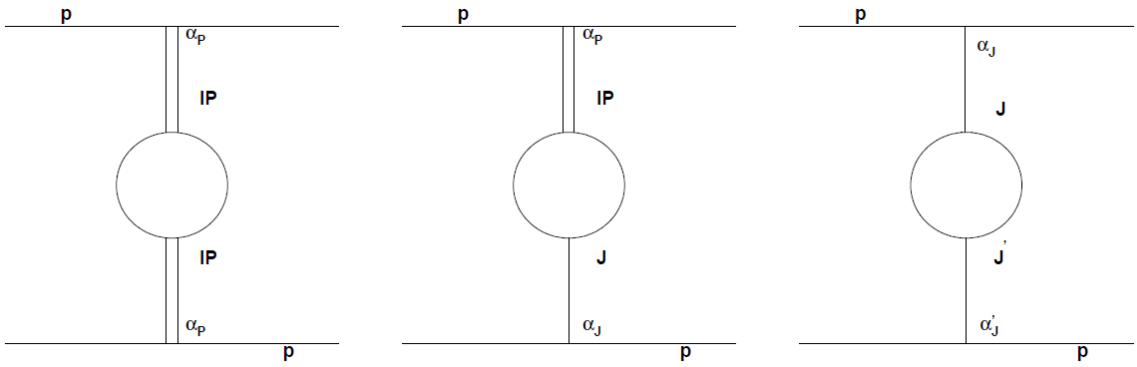

Figure 1.12: Diagrams types contributing to baryon (all) and antibaryon (first one). α values are coresponding to different BN transport processes in string junction or constituent quark model.

Here we consider that pomeron intercept α_p = 1.2 [16] and α_j and α_j‘ are string junction intercepts as summarized in Table 1.1 in all possible combinations.

Antibaryons are coming only from pair production (left diagram on Figure 1.12), therefore:

$$N_{\bar{B}} \approx e^{2(\alpha_p - 1)\Delta y} \qquad (1.16)$$

Baryons are created in pair production too but in addition can be transferred from one or both beams. Therefore:

$$N_B \approx e^{2(\alpha_p - 1)\Delta y} + \sum_i e^{(\alpha_p - 1)\Delta y} . e^{(\alpha_j^i - 1)\Delta y} + \sum_{i,k} e^{(\alpha_j^i - 1)\Delta y} . e^{(\alpha_j^k - 1)\Delta y} \qquad (1.17)$$

Using (1.16) and (1.17) we can derive formula for antibaryon to baryon ratio as a function of rapidity interval Δy

$$1/R = \left(1 + \sum_i C_i e^{(\alpha_j^i - \alpha_p)\Delta y}\right)^2 \qquad (1.18)$$

where *i* = 1, 2 ,3 means string junction accompanied by diquark, quark or flying itself.

If we use only two first diagrams and only α_j = 0.5, formula (1.17) takes the simple form

$$N_B \approx e^{2(\alpha_p - 1)\Delta y} + C.e^{(\alpha_p - 1)\Delta y}.e^{(\alpha_j - 1)\Delta y} \qquad (1.19)$$

and ratio takes the simple form [17]

$$1/R = 1 + C.e^{(\alpha_j - \alpha_p)\Delta y} \qquad (1.20)$$

We can fit function (1.18) to the data, using as value for the Pomeron intercept α_p = 1.2 and string junction intercepts as summarized in Table 1.1, whereas constants, which determines the relative contributions of the diagrams, are adjusted to the measurements from NA49 [18], ISR [19] and RHIC [20].

The constituent quark model can describe the low energy points from NA49 and ISR, but is starting to be off even for higher ISR energies. We can see that this model clearly overestimates the measured ratio from RHIC experiments at √s = 200GeV

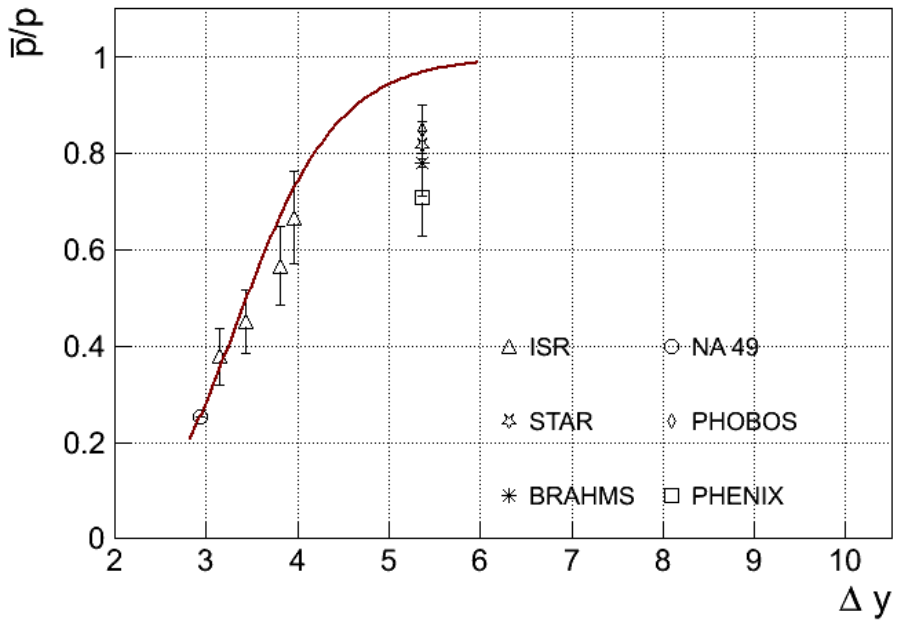

Figure 1.13: Antiproton-to-proton ratio as a function of rapidity gap Δy. Different experimental points are fitted by function (1.18) considering the constituent quark model

For string junction model, the situation is much better. By adding the processes with more string breakage, especially process with string junction accompanied by quark we can describe all the experimental measurements.

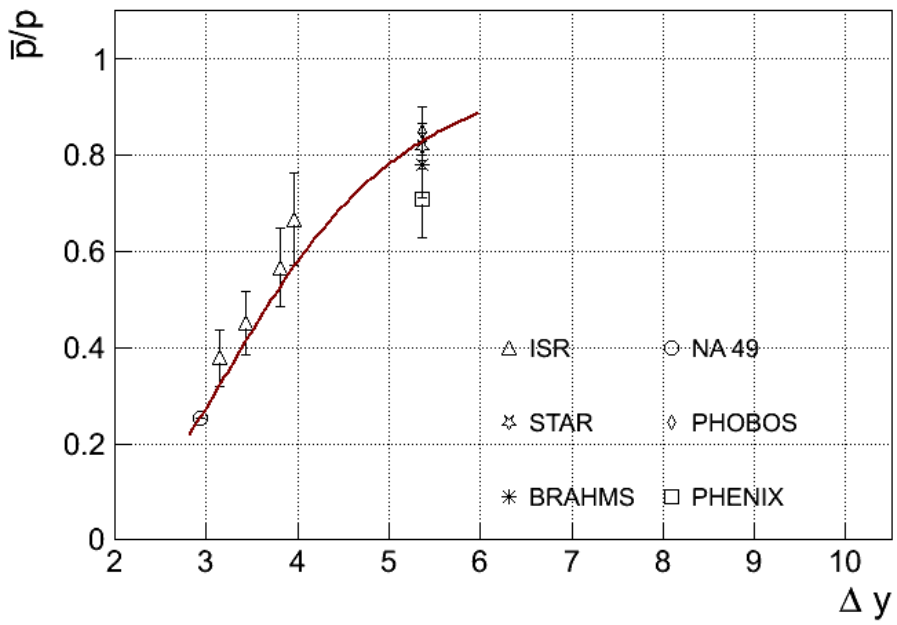

Figure 1.14: Antiproton-to-proton ratio as a function of rapidity gap Δy. Different experimental points are fitted by function (1.18) considering the string junction model

Thanks to this argument we can make a statement that even at intermediate energies we can see clear disagreement between amounts of transported baryon number predicted by constituent quark model and experimental data. In contrast string junction model driven function is describing the data well.

1.4 Motivation for measurement of different properties of the antibaryon – to baryon ratio

1.4.1 Mid rapidity ratio for high energies

At LHC energies we can investigate the convergence of the antibaryon to baryon ratio. Considering the string junction model of the baryon two marginal values of α_j were debated for pure gluonic process of baryon number transport. These two concepts result in a significantly different BN distribution with rapidity (BN transport), when the proton interacts inelasticaly at high energies. We can use the parameterization with function (1.18) including all possible values for α: -½ for diquark-SJ, ½ for quark-SJ and 1 for SJ itself. The two concepts result for significantly different value for adjusted constant corresponding to $\alpha = 1$.

If we take the last α as close to 1, then the last process is not or just slightly suppressed at large values of Δy and as a consequence we can see non-zero asymmetry at 7TeV. The prediction of QGSM [14] for α_j = 0.9 with parameterization with function (1.18) you can see on Figure 1.15.

α_j value equal to unity induce antibaryon to baryon asymmetry converging at high energies to non-zero value. Contribution of the process with α = 1 is significant. The constant corresponding to α = 1 is 0.2 ± 0.03.

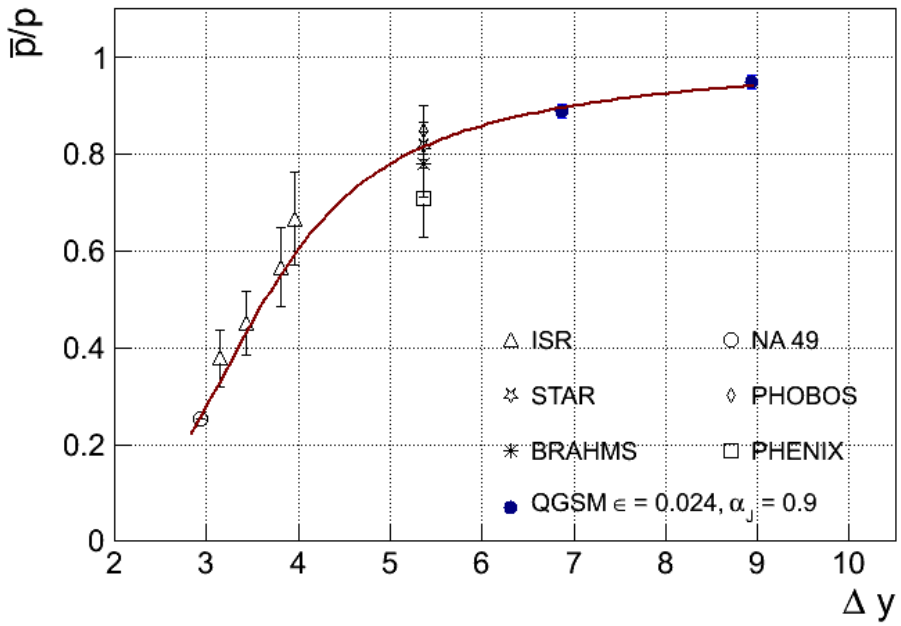

Figure 1.15: Antiproton-to-proton ratio as a function of rapidity gap Δy. Experimental measured values are showed together with prediction of QGSM [14] for α_j = 0.9 at √s = 900GeV and 7TeV.Points are fitted by function (1.18) considering the string junction model.

Another possibility is that α_j = 0.5. This induces vanishing baryon number transport and antibaryon to baryon ratio at 7TeV close to unity. This possibility with corresponding fit is showed on Figure 1.16.

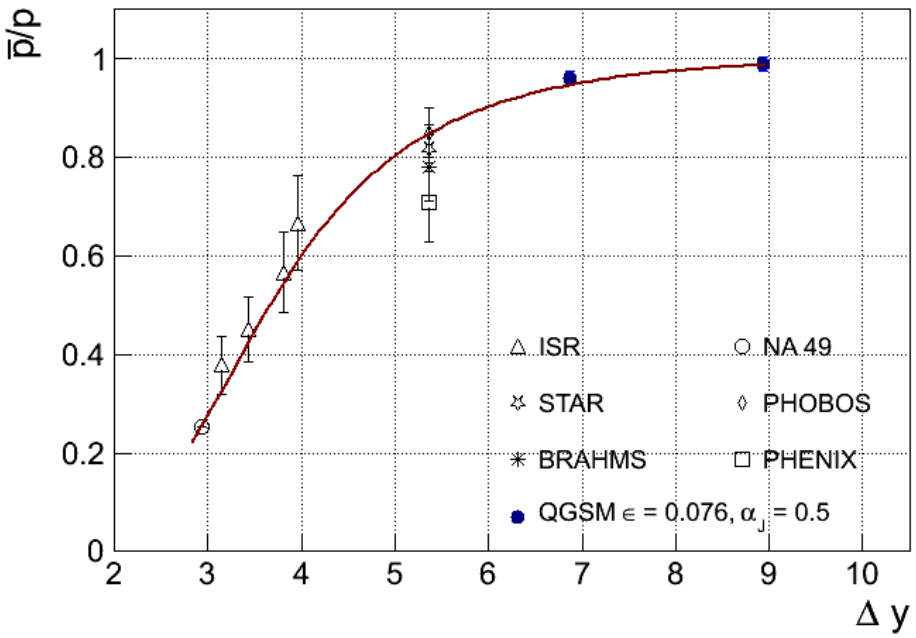

Figure 1.16: Antiproton-to-proton ratio as a function of rapidity gap Δy. Experimental measured values are showed together with prediction of QGSM [14] for $\alpha_j = 0.5$ at $\sqrt{s}$ = 900GeV and 7TeV.Points are fitted by function (1.18) considering the string junction model.

From the parameterization we can see that contribution of the process with α = 1 is negligible. The constant corresponding to α = 1 is -0.02 ± 0.04. This time we can describe the behavior using only two terms with for α: -½ for diquark-SJ, ½ for quark-SJ. We are taking the α for SJ-itself as ½ and since it is the same value as for quark-SJ, we don't need third term in (1.18).

1.4.2 Strangeness dependence

Strangeness dependence is driven by fact that colliding particles are protons but by string breakage, also strange quarks can be created from the sea and resulting baryon is therefore strange or even multistrange. This fact itself is giving a limitation on amount of baryon number transport for strange particles.

Considering a proton as the baryon produced and decelerated in event all possible combinations of valence quarks (accompanying the string junction) and transported from projectile into product are allowed. When we consider a strange baryon as a product, for example Λ, the number of combinations is lower because one strange quark has to be

created from the sea. In case of multistrange baryons, the diquark process is even completely forbidden.

The relative factors (relative to p) for different processes in case of Λ, Ξ and Ω are summarized in the table.

	Diquark	quark	SJ itself
Λ	2/5	3/5	1
Ξ	0	1/5	1
Ω	0	0	1

Table 1.2: Relative factors for strange baryons with respect to proton for different processes of baryon number transport

Since the number of processes is decreasing the total baryon number transport is smaller and this leads to increase of antibaryon to baryon ratio as a function of strangeness of final baryon. Precisely said the antibaryon to baryon ratio is a function of absolute difference of strangeness of projectile and final baryon.

The increase of a ratio with strangeness was measured by STAR [21] experiment and can be seen on Figure 1.17.

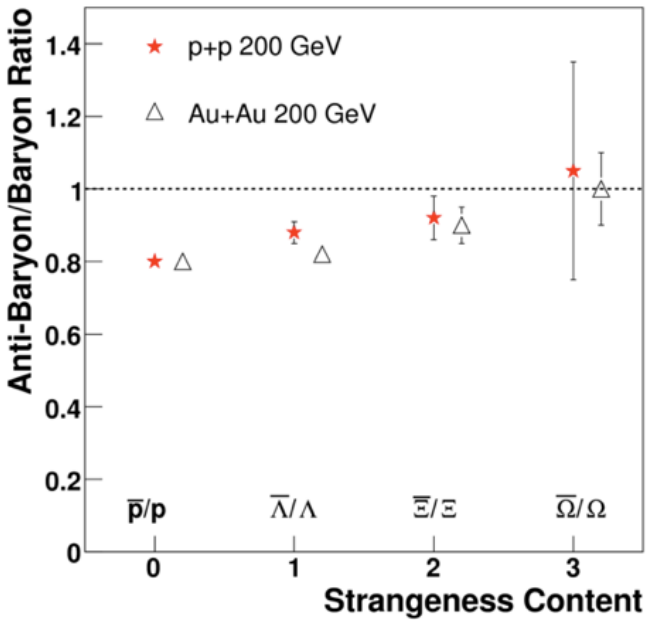

Figure 1.17: Antibaryon-to-baryon ratio for different strangeness contens as measured by STAR [21] experiment at √s = 200GeV in proton-proton and heavy ion collions.

At the LHC we are working with much higher energies, and thus the ratio in general will be closer to unity and difference between different baryons will be smaller.

1.4.3 Transverse momentum and multiplicity dependence

Transverse momentum can be seen as an indicator of collision hardness. Particles with higher transverse momentum are coming from harder collisions.

Harder collisions have in general also higher multiplicity of produced particles, so these two variables: transverse momentum and multiplicity are in some meaning similar.

As was said in previous sections, overall multiplicity coming from event with presence of different baryon number transport process is proportional to number of broken strings. Due to this, in high multiplicity sample we have higher probability to find events with baryon number transported by string junction itself.

Similar explanation can be done for transverse momentum. So in general, antibaryon to baryon ratio can decrease as a function of transverse momentum and/or multiplicity.

At mid rapidity, antibaryon to baryon ratio was measured by many experiments, but the decrease was not seen. Latest result in proton-proton collisions is from STAR experiment [21] at √s = 200GeV

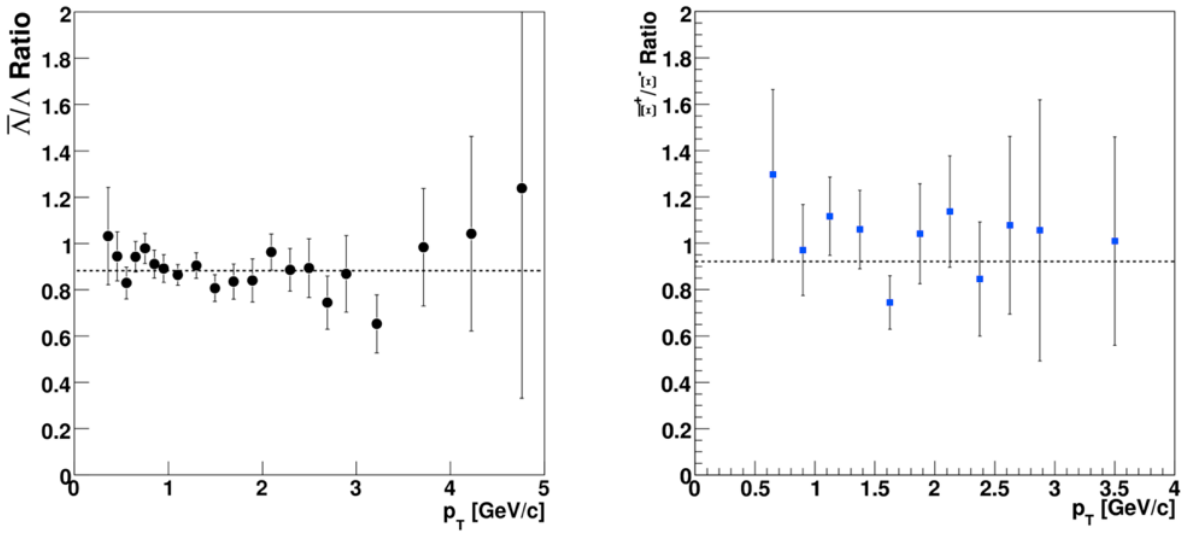

Figure 1.18: $\bar{\Lambda}/\Lambda$ (left) and $\overline{\Xi^+}/\Xi^-$(right) ratio as a function of transverse momentum. Measurement of STAR experiment [21] in proton-proton collisions at √s = 200GeV.

At ALICE we are able measure this dependence with high precision.

1.4.4 Rapidity dependence

Rapidity dependence of the ratio is direct consequence of formula (1.11). The further from central region we are, the higher the probability of BN transport is. Due to this the ratio has to decrease as a function of rapidity, if the measured interval around central rapidity is large enough.

This effect was measured for $\bar{\Lambda}/\Lambda$ ratio at 900GeV and 7TeV by LHCb experiment [22] which is due to its rapidity acceptance ideal for this measurement.

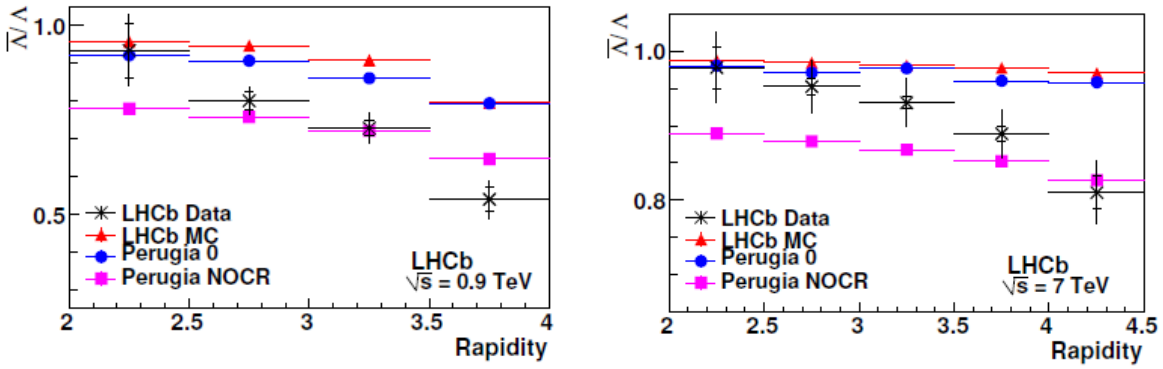

Figure 1.19: $\bar{\Lambda}/\Lambda$ ratio as a function of rapidity. Measurement of LHCb experiment at $\sqrt{s}$ = 900GeV (left) and 7TeV(right).

In ALICE we can see the ratio in central rapidity up to |y|<1 at maximum due to acceptance of the detector (see Chapter 2). We are interested if central region is flat and if we can see any decrease even this small interval.

1.5 Objectives of the thesis

Driven by motivations described in previous section, this thesis has the following goals: To analyze the antibaryon-to-baryon ratio in the data of proton-proton collisions measured by ALICE experiment at LHC energies $\sqrt{s}$ = 900GeV, 2.76TeV and 7TeV for the baryons – proton, Λ, charged Ξ and charged Ω and find out:

- central rapidity ratio values – the convergence in Δy

- behavior of the ratio in rapidity, transverse momentum and charged particle multiplicity
- possible strangeness dependence

2 ALICE

2.1 ALICE Experiment

ALICE is a general-purpose heavy-ion experiment designed to study the physics of strongly interacting matter and the quark–gluon plasma in nucleus–nucleus collisions at the LHC. The detector consists of a central part, which measures event-by-event hadrons, electrons and photons, and of a forward spectrometer to measure muons. The central part, which covers polar angles from 45° to 135° over the full azimuth, is embedded in the large L3 solenoidal magnet. It consists of: an Inner Tracking System (ITS) [24] of high-resolution silicon detectors; a cylindrical Time-Projection Chamber (TPC) [25]; three particle identification arrays of: Time-Of-Flight (TOF) detector [26], a single-arm ring imaging Cherenkov (HMPID) [28] and Transition-Radiation Detector (TRD) [27]; and a single-arm electromagnetic calorimeter (PHOS) [29]. The forward muon arm [30] consists of a complex arrangement of absorbers, a large dipole magnet, and fourteen planes of tracking and triggering chambers. Several smaller detectors (ZDC, PMD, FMD, T0, and V0) for global event characterization and triggering are located at forward angles. An array of scintillators (ACORDE) on top of the L3 magnet will be used to trigger on cosmic rays.

The ALICE experiment, shown in figure 3.1 [31], consists of a central detector system, covering mid-rapidity ($|\eta| < 0.9$) over the full azimuth, and several forward systems. The central system is installed inside a large solenoidal magnet which generates a magnetic field of 0.5 T. The central system includes, from the interaction vertex to the outside, six layers of high-resolution silicon detectors (Inner Tracking System—ITS), the main tracking system of the experiment (Time-Projection Chamber—TPC), a transition radiation detector for electron identification (Transition-Radiation Detector—TRD), and a particle identification array (Time-Of-Flight—TOF). The central system is complemented by two small-area detectors: an array of ring-imaging Cherenkov detectors for the identification of high-momentum particles (High-Momentum Particle Identification Detector—HMPID), and an electromagnetic calorimeter consisting of arrays of high-density crystals (PHOton Spectrometer— PHOS). The large rapidity systems include a muon spectrometer, a photon counting detector (Photon Multiplicity Detector—PMD, on

the opposite side), an ensemble of multiplicity detectors (Forward Multiplicity Detector—FMD) covering the large rapidity region (up to η = 5.1). A system of scintillators and quartz counters (T0 and V0) will provide fast trigger signals, and two sets of neutron and hadron calorimeters, located at 0° and about 115m away from the interaction vertex, will measure the impact parameter (Zero-Degree Calorimeter—ZDC). An absorber positioned very close to the vertex shields the muon spectrometer. The spectrometer consists of a dipole magnet, five tracking stations, an iron wall (muon filter) to absorb remaining hadrons, and two trigger stations behind the muon filter.

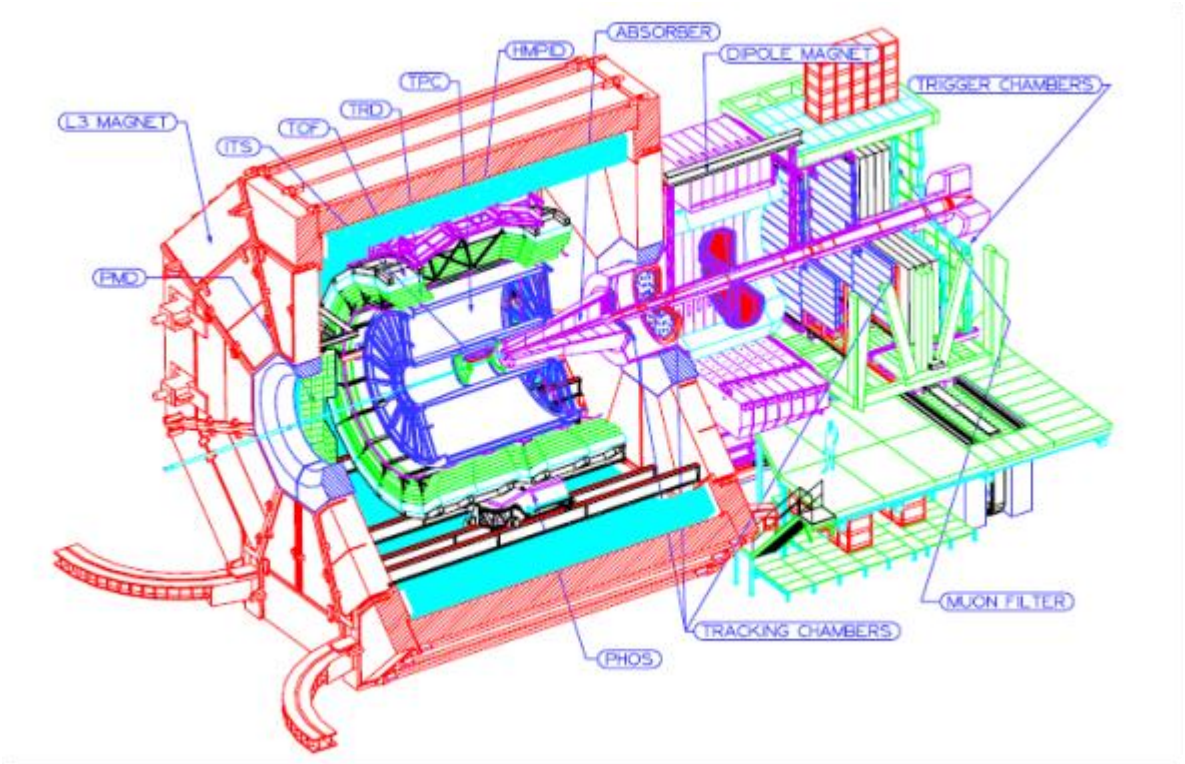

Figure 2.1: Picture of ALICE experiment detector. Central detectors and forward systems are shown.

2.1.1 Inner Tracking System

The Inner Tracking System (ITS) [24] consists of six cylindrical layers of silicon detectors, located at radii, r = 4, 7, 15, 24, 39 and 44 cm. It covers the rapidity range of $|\eta| < 0.9$ for all vertices located within the length of the interaction diamond ($\pm 1\sigma$), i.e. 10.6 cm along the beam direction. The number, position and segmentation of the layers are optimized for efficient track finding and high impact-parameter resolution. In particular, the outer radius is determined by the necessity to match tracks with those from the Time-

Projection Chamber (TPC), and the inner radius is the minimum allowed by the radius of the beam pipe (3 cm). The first layer has a more extended coverage ($|\eta| < 1.98$) to provide, together with the Forward Multiplicity Detectors (FMD), a continuous coverage in rapidity for the measurement of charged-particles multiplicity. Because of the high particle density, up to 80 particles cm^{-2}, and to achieve the required impact parameter resolution, pixel detectors have been chosen for the innermost two layers, and silicon drift detectors for the following two layers. The outer two layers, where the track densities are below 1 particle cm^{-2}, will be equipped with double-sided silicon micro-strip detectors. With the exception of the two innermost pixel planes, all layers will have analogue readout for particle identification via dE/dx measurement in the non-relativistic ($1/\beta^2$) region. This will give the ITS stand-alone capability as a low-p_t particle spectrometer.

The tasks of the ITS are:

- to localize the primary vertex with a resolution better than 100 μm;
- to reconstruct the secondary vertices from decays of hyperons and D and B mesons;
- to track and identify particles with momentum below 100 MeV;
- to improve the momentum and angle resolution for the high-p_t particles which also traverse the TPC;
- to reconstruct, albeit with limited momentum resolution, particles traversing dead regions of the TPC.

The ITS contributes to the global tracking of ALICE by improving the momentum and angle resolution obtained by the TPC. This is beneficial for practically all physics topics addressed by the ALICE experiment.

2.1.2 Time Projection Chamber

The Time-Projection Chamber (TPC) [25] is the main tracking detector of the ALICE central barrel and, together with the other central barrel detectors has to provide charged-particle momentum measurements with good two-track separation, particle identification, and vertex determination. The phase space covered by the TPC ranges in pseudo-rapidity $|\eta| < 0.9$ (up to $|\eta| < 1.5$ for tracks with reduced track length and momentum resolution); in p_t up to 100 GeV/c is reached with good momentum resolution. In addition, data from the central barrel detectors will be used to generate a fast online

High-Level Trigger (HLT) for the selection of low cross-section signals. All these requirements need to be fulfilled at the Pb–Pb design luminosity, corresponding to an interaction rate of 8 kHz, of which about 10% are to be considered as central collisions. For these we assume the extreme multiplicity of $dN_{CH}/d\eta$ = 8000, resulting in 20 000 charged primary and secondary tracks in the acceptance, an unprecedented track density for a TPC.

The TPC design is ‘conventional’ in overall structure but innovative in many details. The TPC is cylindrical in shape and has an inner radius of about 85 cm, an outer radius of about 250 cm, and an overall length along the beam direction of 500 cm.

The detector is made of a large cylindrical field cage, filled with 88m3 of Ne/CO2 (90%/10%), which is needed to transport the primary electrons over a distance of up to 2.5m on either side of the central electrode to the end-plates. The drift gas Ne/CO2 (90%/10%) is optimized for drift speed, low diffusion, low radiation length and hence low multiple scattering, small space-charge effect, and ageing properties. The drawback of Ne/CO2 is that this mixture is a ‘cold’ gas, with a steep dependence of drift velocity on temperature.

Multi-wire proportional chambers with cathode pad readout are mounted into 18 trapezoidal sectors of each end-plate. The overall acceptance covered by the TPC is $|\eta| < 0.9$ for full radial track length and matches that of the ITS, TRD, and TOF detectors; for reduced track length (and poorer momentum resolution), an acceptance up to about $|\eta| = 1.5$ is accessible.

The material budget of the TPC is kept as low as possible to ensure minimal multiple scattering and secondary particle production. Thus both the field cage and drift gas are made of materials with small radiation length. The TPC material is about 3.5% of a radiation length for tracks with normal incidence.

The field cage is based on a design with a central high-voltage electrode and two opposite axial potential dividers which create a highly uniform electrostatic field in the common gas volume. Because of the Ne/CO2 (90%/10%) gas mixture used in the TPC, the field cage will have to be operated at very high-voltage gradients, of about $400 Vcm^{-1}$, with a high voltage of 100 kV at the central electrode which results in a maximum drift time of about 90 μs.

The readout chambers instrument the two end-caps of the TPC cylinder with an overall active area of 32.5 m^2. The chambers are multi-wire proportional chambers with cathode pad readout. Because of the radial dependence of the track density, the readout is segmented radially into two readout chambers with slightly different wire geometry adapted to the varying pad sizes mentioned below. The radial distance of the active area is from 84.1 to 132.1 cm (and from 134.6 to 246.6 cm) for the inner (and outer) chamber, respectively. The readout chambers are normally closed by a gating grid for electrons coming from the drift volume and they are opened only by the L1 trigger (6.5 μs after the collision) for the duration of one drift-time interval, i.e. of about 90 μs. This helps to prevent space charge due to positive ions from drifting back from the multiplication region for non-triggered interactions and background.

A laser system with some hundred straight tracks in all regions of the drift space will allow precise position inter-calibration for the readout chambers and monitoring of temperature and space-charge distortions.

2.1.3 Transition Radiation Detector

The main goal of the ALICE Transition-Radiation Detector (TRD) [27] is to provide electron identification in the central barrel for momenta greater than 1 GeV/c, where the pion rejection capability through energy loss measurement in the TPC is no longer sufficient. As a consequence, the addition of the TRD significantly expands the ALICE physics objectives [31] [32].

The TRD will provide, along with data from the TPC and ITS, sufficient electron identification to measure the production of light and heavy vector-meson resonances and the dilepton continuum in Pb–Pb and pp collisions. In addition, the electron identification provided by the TPC and TRD for p_t > 1 GeV/c can be used, in conjunction with the impact-parameter determination of electron tracks in the ITS, to measure open charm and open beauty produced in the collisions.

A similar technique can be used to separate directly produced J/ψ mesons from those produced in B-decays. These secondary J/ψ's could potentially mask the expected J/ψ yield modification due to quark–gluon plasma formation; their isolation is, therefore, of crucial importance for such measurements.

Furthermore, since the TRD is a fast tracker, it can be used as an efficient trigger for high transverse momentum electrons. Such a trigger would considerably enhance the recorded Υ yields in the high-mass part of the dilepton continuum as well as high-p_t J/ψ.

2.1.4 Time-Of-Flight Detector

The Time-Of-Flight (TOF) detector of ALICE [26] is a large area array that covers the central pseudo-rapidity region ($|\eta| < 0.9$) for Particle Identification (PID) in the intermediate momentum range (from 0.2 to 2.5 GeV/c). Since the majority of the produced charged particles are emitted in this range, the performance of such a detector is of crucial importance for the experiment [31].

The measurement and identification of charged particles in the intermediate momentum range will provide observables which can be used to probe the nature and dynamical evolution of the system produced in ultra-relativistic heavy-ion collisions at LHC energies. The TOF, coupled with the ITS and TPC for track and vertex reconstruction and for dE/dx measurements in the low-momentum range (up to about 0.5 GeV/c), will provide event-by-event identification of large samples of pions, kaons, and protons.

The TOF-identified particles will be used to study relevant hadronic observables on a single-event basis. In addition, at the inclusive level, identified kaons will allow invariant mass studies, in particular the detection of open charm states and the φ meson. A large-coverage, powerful TOF detector, operating efficiently in extreme multiplicity conditions, should have an excellent intrinsic response and an overall occupancy not exceeding the 10–15% level at the highest expected charged-particle density ($\mathrm{d}N_{\mathrm{CH}}/\mathrm{d}\eta = 8000$). This implies a design with more than 105 independent TOF channels. Since a large area has to be covered, a gaseous detector is the only choice. In the framework of the LAA project at CERN an intensive R&D program has shown that the best solution for the TOF detector is the Multi-gap Resistive-Plate Chamber (MRPC). The key aspect of these chambers is that the electric field is high and uniform over the whole sensitive gaseous volume of the detector. Any ionization produced by a traversing charged particle will immediately start a gas avalanche process which will eventually generate the observed signals on the pick-up electrodes. There is no drift time associated with the movement of the electrons to a region

of high electric field. Thus the time jitter of these devices is caused by the fluctuations in the growth of the avalanche.

2.1.5 High-Momentum Particle Identification Detector

The High-Momentum Particle Identification Detector (HMPID) [28] is dedicated to inclusive measurements of identified hadrons for $p_t > 1$ GeV/c. The HMPID was designed as a single-arm array with an acceptance of 5% of the central barrel phase space. The geometry of the detector was optimized with respect to particle yields at high-p_t in both pp and heavy-ion collisions at LHC energies, and with respect to the large opening angle (corresponding to small effective size particle emitting sources) required for two-particle correlation measurements. HMPID will enhance the PID capability of the ALICE experiment by enabling identification of particles beyond the momentum interval attainable through energy loss (in ITS and TPC) and time-of-flight measurements (in TOF).

The detector was optimized to extend the useful range for π/K and K/p discrimination, on a track-by-track basis, up to 3 and 5 GeV/c respectively.

The HMPID is based on proximity-focusing Ring Imaging Cherenkov (RICH) counters and consists of seven modules of about 1.5×1.5 m^2 each, mounted in an independent support cradle. The cradle will be fixed to the space frame in the two o'clock position.

2.1.6 Photon Spectrometer

The PHOton Spectrometer [29] is a high-resolution electromagnetic spectrometer which will detect electromagnetic particles in a limited acceptance domain at central rapidity and provide photon identification as well as neutral mesons identification through the two-photon decay channel.

The main physics objectives are the following:

- Testing thermal and dynamical properties of the initial phase of the collision, in particular the initial temperature and space–time dimensions of the hot zone,

through measurement of direct single-photon and diphoton spectra and Bose–Einstein correlations of direct photons.

- Investigating jet quenching as a probe of deconfinement, through measurement of high-pt π0 spectrum, and identifying jets through γ–jet and jet–jet correlations measurements. The principal requirements on PHOS include the ability to identify photons, discriminate direct photons from decay photons and perform momentum measurements over a wide dynamic range with high energy and spatial resolutions.

2.1.7 Forward muon spectrometer

Hard, penetrating probes, such as heavy-quarkonia states, are an essential tool for probing the early and hot stage of heavy-ion collisions. At LHC energies, energy densities high enough to melt the Υ(1s) will be reached. Moreover, production mechanisms other than hard scattering might play a role [30]. Since these additional mechanisms strongly depend on charm multiplicity, measurements of open charm and open beauty are of crucial importance (the latter also represents a potential normalization for bottomium).

The complete spectrum of heavy quark vector mesons, as well as the φ meson, will be measured in the μ+μ− decay channel by the ALICE muon spectrometer. The simultaneous measurement of all the quarkonia species with the same apparatus will allow a direct comparison of their production rate as a function of different parameters such as transverse momentum and collision centrality. In addition to vector mesons, also the unlike-sign dimuon continuum up to masses around 10 GeV c^{-2} will be studied.

Since at LHC energies the continuum is expected to be dominated by muons from the semi-leptonic decay of open charm and open beauty, it will also be possible to study the production of open (heavy) flavours with the muon spectrometer. Heavy-flavour production in the region $-2.5 < \eta < -1$ will be accessible through measurement of e–μ coincidences, where the muon is detected by the muon spectrometer and the electron by the TRD.

2.2 Track reconstruction with central detectors

In this part we focus on the track and vertex reconstruction in the central part of the ALICE detector, which includes Inner Tracker System (ITS), Time Projection Chamber (TPC), Transition Radiation Detector (TRD), Time-Of-Flight detector (TOF), High Momentum Particle Identification Detector (HMPID) and Photon Spectrometer (PHOS).

Track reconstruction is one of the most challenging tasks in this experiment. It is of great importance to precisely determine the momentum of particles as close as possible to the point of their generation (main interaction point or secondary decay vertices). Also, the track reconstruction procedure should be capable of a precise extrapolation of the tracks to the detectors providing the particle identification information (TOF, HMPID, PHOS) that are, in the case of ALICE, situated far away from the main interaction point.

For various kinds of physics analysis of the data, knowledge about the position where the particle was generated (the primary and secondary vertices) is necessary. The reconstruction software should provide such information.

Wherever it is not specified explicitly as different, we refer to the 'global ALICE coordinate system'. It is a right-handed coordinate system with the *z* axis coinciding with the beam-pipe axis and going in the direction opposite to the muon arm, the *y* axis going up, and the origin of coordinates defined by the intersection point of the *z* axis and the central membrane plane of TPC.

We also use the following terms:

- *Digit:* This is a digitized signal (ADC count) obtained by a sensitive pad of a detector at a certain time.
- *Cluster:* This is a set of adjacent (in space and/or in time) digits that were presumably generated by the same particle crossing the sensitive element of a detector.
- Reconstructed *space point:* This is the estimation of the position where a particle crossed the sensitive element of a detector (often, this is done by calculating the center of gravity of the 'cluster').

- Reconstructed *track:* This is a set of five parameters (such as the curvature and the angles with respect to the coordinate axes) of the particle's trajectory together with the corresponding covariance matrix estimated at a given point in space.

2.2.1 Primary-vertex reconstruction

The reconstruction of the primary-vertex position in ALICE is done either using the information provided by the silicon pixel detectors, which constitute the two innermost layers of the ITS, or using reconstructed tracks.

2.2.2 Track-finding strategy

Depending on the way, the information is used; the tracking methods can be divided into two large groups: global methods and local methods. Each group has advantages and disadvantages.

With the global methods, all the track measurements are treated simultaneously and the decision to include or exclude a measurement is taken when all the information about the track is known. Typical algorithms belonging to this class are combinatorial methods, Hough transform, templates and conformal mappings. The advantages are the stability with respect to noise and miss-measurements and the possibility to operate directly on the raw data. On the other hand, these methods require a precise global track model. Such a track model can sometimes be unknown or does not even exist because of stochastic processes (energy losses, multiple scattering), non-uniformity of the magnetic field etc. In ALICE, global tracking methods are being extensively used in the High-Level Trigger (HLT) software. There, we are mostly interested in the reconstruction of the high-momentum tracks only, the required precision is not crucial, but the speed of the calculations is of great importance.

Local methods do not need the knowledge of the global track model. The track parameters are always estimated 'locally' at a given point in space. The decision to accept or to reject a measurement is made using either the local information or the information coming from the previous 'history' of this track. With these methods, all the local track peculiarities (stochastic physics processes, magnetic fields, detector geometry) can be naturally accounted for. Unfortunately, the local methods rely on sophisticated space point

reconstruction algorithms (including unfolding of overlapped clusters). They are sensitive to noise, wrong or displaced measurements and the precision of space point error parameterization. The most advanced kind of local track-finding methods is Kalman filtering [33].

In ALICE we require a good track-finding efficiency and a reconstruction precision for tracks down to p_t = 100MeV/c. Some of the ALICE tracking detectors (ITS, TRD) have a significant material budget. Under such conditions one cannot neglect the energy losses or the multiple scattering in the reconstruction. There are also rather big dead zones between the tracking detectors which complicates finding the continuation of the same track. For all these reasons, it is the Kalman-filtering approach that has been our choice for the offline reconstruction since the very beginning.

The reconstruction begins with cluster finding in all of the ALICE central detectors (ITS, TPC, TRD, TOF, HMPID and PHOS). Using the clusters reconstructed at the two pixel layers of the ITS, the position of the primary vertex is estimated and the track finding starts. As described later, cluster-finding as well as the track-finding procedures performed in the detectors have some different detector-specific features. Moreover, within a given detector, because of high occupancy and a big number of overlapped clusters, the cluster finding and the track finding are not completely independent: the number and positions of the clusters are finally determined only at the track-finding step.

The general tracking strategy is the following. We start from our best tracker device, i.e. the TPC, and from the outer radius where the track density is minimal. First, the track candidates (‘seeds’) are found. Because of the small number of clusters assigned to a seed, the precision of its parameters is not enough to safely extrapolate it outwards to the other detectors. Instead, the tracking stays within the TPC and proceeds towards the smaller TPC radii. Whenever possible, new clusters are associated with a track candidate in a ‘classical’ Kalman-filter way and the track parameters are more and more refined. When all of the seeds are extrapolated to the inner limit of the TPC, the tracking in the ITS takes over. The ITS tracker tries to prolong the TPC tracks as close as possible to the primary vertex. On the way to the primary vertex, the tracks are assigned additional, precisely reconstructed ITS clusters, which also improves the estimation of the track parameters.

After all the track candidates from the TPC are assigned their clusters in the ITS, a special ITS stand-alone tracking procedure is applied to the rest of the ITS clusters. This procedure tries to recover the tracks that were not found in the TPC because of the p_t cut-off, dead zones between the TPC sectors, or decays.

At this point the tracking is restarted from the vertex back to the outer layer of the ITS and then repeated towards the outer wall of the TPC. For the track that was labeled by the ITS tracker as potentially primary, several particle-mass-dependent, time-of-flight hypotheses are calculated. These hypotheses are then used for the particle identification (PID) with the TOF detector. Once the outer radius of the TPC is reached, the precision of the estimated track parameters is sufficient to extrapolate the tracks to the TRD, TOF, HMPID and PHOS detectors. Tracking in the TRD is done in a similar way to that in the TPC. Tracks are followed till the outer wall of the TRD and the assigned clusters improve the momentum resolution further. Next, the tracks are extrapolated to the TOF, HMPID and PHOS, where they acquire the PID information. Finally, all the tracks are refitted with the Kalman filter backwards to the primary vertex (or to the innermost possible radius, in the case of the secondary tracks).

The tracks that passed the final refit are used for the secondary vertex (V^0, cascade, kink) reconstruction. There is also an option to reconstruct the secondary vertices 'on the fly' during the tracking itself. The potential advantage of such a possibility is that the tracks coming from a secondary vertex candidate are not extrapolated beyond the vertex, thus minimizing the risk of picking up a wrong track prolongation. The reconstructed tracks (together with the PID information), kink, V0 and cascade particle decays are then stored in the Event Summary Data (ESD).

Every detector, if it contributes to the reconstruction of a track, improves the reconstruction quality of this track. However, the requirement of being reconstructed in as many detectors as possible reduces the statistics of such tracks. The overall software track-finding efficiency is still rather high (about 90% practically at any momenta), but the physical track-finding efficiency is much more dependent on the number of contributing detectors. This is true both for the case of the high multiplicity events and pp events, because the physical efficiency is mainly defined by the particle decays, presence of dead zones, and interactions with the material.

2.2.3 Secondary-vertex reconstruction

The V^0 finding procedure starts with the selection of secondary tracks: tracks which have a too small impact parameter with respect to the primary vertex are eliminated. Then, one has to combine each 'secondary' track with all the other 'secondary' tracks having an opposite charge. Two different cuts are applied for the positive track ($b+$) and the negative track ($b-$) impact parameters. Such pairs of tracks are rejected if the distance of closest approach (DCA) in space between the two tracks is larger than a given value. The minimization of the distance between the tracks is performed numerically using a 3-dim helix track parameterization. There is also a possibility to minimize a 'normalized DCA' which takes into account the possible difference in the reconstructed track position in the transverse plane and along the beam direction. This increases slightly the precision of the reconstructed V^0 position, especially for the high momentum V^0's. This position is supposed to be on the line corresponding to the DCA while the distance between a track and the vertex is proportional to the norm of the covariance matrix of the track parameters.

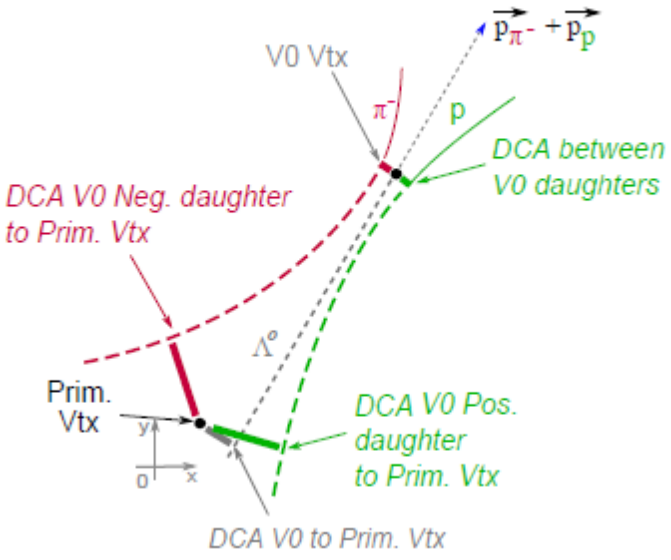

Figure 2.2: Picture ilustrating reconstruction of secondary (decay) vertex of V^0 track (Λ). Topological parameters used in reconstruction procedure are also shown.

Once the vertex position is defined, only the secondary vertices inside a given fiducial volume are kept. The inner boundary of this fiducial area is limited by the expected particle density and the tracking precision which, in turn, is mainly defined by the multiple scattering on the pixel layers of the ITS. It can be shown that, assuming a particle density

of $dN_{CH}/d\eta$ = 4000 and being given the current material budget together with the present tracking software, one can hardly go deeper than 0.9 cm from the primary interaction point. The outer limit was initially imposed by the radius of the beam pipe (3 cm), however there is a possibility to extend this limit up to the inner radius of the TPC.

Finally, the V^0 finding procedure checks whether the momentum of the V^0 candidate points well back to the primary vertex. Hence we extrapolate the two tracks of this candidate to the points of the DCA and calculate the V^0 momentum as the sum of the track momenta taken at those points. Then we apply a cut on the cosine of the angle (pointing angle) between the V^0 momentum (P) and a vector I connecting the primary vertex and the V^0 vertex positions ($\cos\Theta_p$).

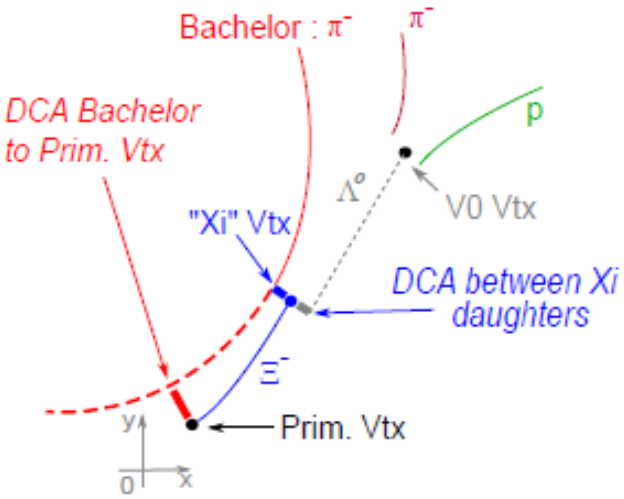

Figure 2.3: Picture ilustrating reconstruction of secondary (decay) vertex of a cascade (Ξ).

The cascade finding procedure, used to reconstruct the Ξ^- and Ω^- baryons and their corresponding antiparticles, starts with looking for all V^0 candidates. Since the Λ's we want to reconstruct here come from cascade particle decay, they do not have to point on the main collision vertex. The condition on the pointing angle is consequently loose. In order to achieve substantial background suppression at this level, we select only the V^0 candidates having a large impact parameter ($b_V{}^0$). Then, the V^0 candidates found within the Λ mass window have to be combined with all possible secondary tracks (bachelor candidates). The impact parameter (b_b) of the bachelor must also be large enough to have a good rejection of primary particles.

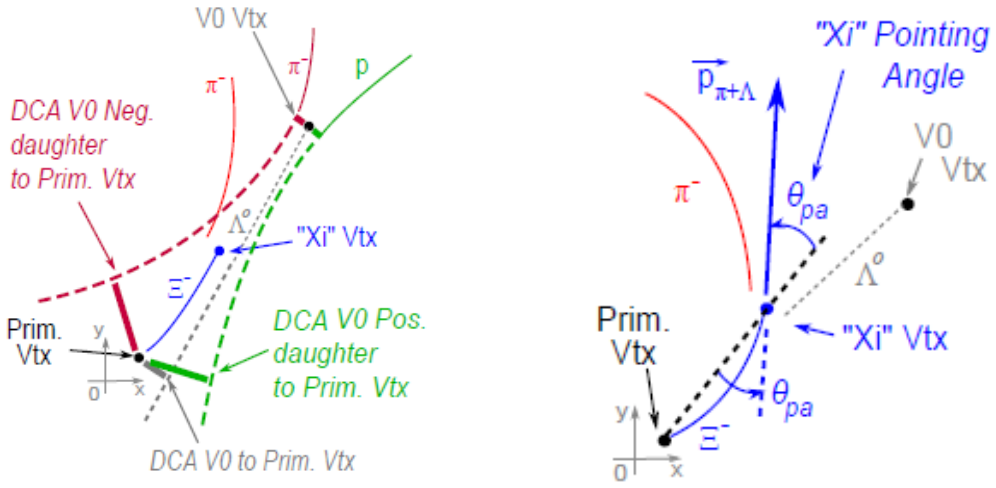

Figure 2.4: Pictures showing topological variables used during cascade secondary vertex reconstraction procedure.

A V^0 bachelor association is accepted if the distance of closest approach (DCA) between the bachelor track (helix) and the V^0 mother trajectory (straight line) is small enough. Finally, we check whether this cascade candidate points well back to the primary vertex. The cascade finding is limited to the same fiducial region as the one used for V^0 reconstruction. Hence, both the cascade decay and the successive Λ decay have to be between r = 0.9 cm and a variable upper limit.

2.3 Charged particle identification

The ALICE experiment is able to identify particles with momenta from about 0.1GeV/c and up to a few GeV/c by combining different detecting systems that are efficient in some narrower and complementary momentum sub-ranges and up to a few Tens GeV/c by using the dE/dx relativistic rise in the TPC [32]. In this Section we will focus on the charged particle identification (PID) capabilities of the central ALICE detectors: The ITS, TPC, TRD and TOF.

In order to identify any stable charged particle, including charged hadrons, it is necessary to determine its charge Ze and its mass m. The charge sign is obtained from the curvature of the particle's track. Since the mass cannot be measured directly, it has to be deduced from other variables. These are in general the momentum p and the velocity $\beta = v/c$, where one exploits the basic relationship

$$p = \gamma m v \rightarrow m = \frac{p}{c\beta\gamma} \qquad (2.1)$$

Here c is the speed of light in vacuum and γ is the relativistic Lorentz factor. The momentum is obtained by measuring the curvature of the track in the magnetic field. The particle velocity is obtained by means of one of the following methods:

- measurement of the energy deposit by ionization
- time-of-flight (TOF) measurements
- detection of Cherenkov radiation
- detection of transition radiation

Each of these methods provides PID not only for charged hadrons, but also for charged leptons.

2.3.1 Ionization measurements

Ionization of matter by charged particles is the primary mechanism underlying most detector technologies. The characteristics of this process, along with the momentum measurement, can be used to identify particles. When a fast charged particle passes through matter, it undergoes a series of inelastic Coulomb collisions with the atomic electrons of the material. As a result, the atoms end up in excited or ionized states, while the particle loses small fractions of its kinetic energy. The average energy loss per unit path length $\langle dE/dx \rangle$ is transformed into the average number of electron-ion pairs (or electron-hole pairs for semiconductors) $\langle N_i \rangle$ that is produced along the length x along the particle's trajectory [34]:

$$x\langle {}^{dE}/_{dx} \rangle = \langle N_i \rangle W, \qquad (2.2)$$

where W is the average energy spent for the creation of one electron-ion (electron- hole) pair. W exceeds the ionization energy E_i of the material, because some fraction of the energy loss is dissipated by excitation, which does not produce free charge carriers.

The interactions of the charged particle with the atomic electrons can be modeled in terms of two components: primary and secondary interactions. In primary interactions direct processes between the charged particle and atomic electrons lead to excitation or ionization of atoms, while secondary processes involve subsequent interactions.

The primary interactions can be characterized by the Rutherford cross-section for energies above the highest atomic binding energy, where the atomic structure can be ignored. In this case the particle undergoes elastic scattering on the atomic electrons as if they were free. According to the steeply falling Rutherford spectrum most of the primary electrons emitted in such collisions have low energy. However, a significant probability for producing primary electrons with energies up to the kinematic limit for the energy transfer E_{max} exists. E_{max} is given by

$$E_{max} = \frac{2\beta^2\gamma^2 m_e c^2}{1 + x^2 + 2\gamma x} \qquad (2.3)$$

where m_e is the electron mass, $x = m_e/m$ and m is the mass of the incident particle. In such collisions, characterized by a very small impact parameter, the energy transferred to the electron will be larger than E_i and the resulting *δ-rays* or *knock-on electrons* produce additional ionization in secondary interactions. *δ-rays* can even leave the sensitive volume of the detector, but a magnetic field may force them to curl up close to the primary charged particle's track. In this case they will contribute to a measurement of the deposited energy. In collisions with large impact parameter the atomic electrons receive much less energy, which is used for excitation without the creation of free charges.

The first calculation for the average energy loss per unit track length based on the quantum mechanical principles of the scattering theory was introduced by Hans Bethe. The well-known Bethe-Bloch formula is modified to yield the restricted (average) energy loss by neglecting higher energy *δ-electrons* through the introduction of an upper limit for the energy transfer in a single collision E_{cut}

$$\left\langle \frac{dE}{dX} \right\rangle \approx \frac{Z^2}{\beta^2}\left(\log \frac{\sqrt{2m_e c^2 E_{cut}}\beta\gamma}{I} - \frac{\beta^2}{2} - \frac{\delta}{2} \right) \qquad (2.4)$$

Here Ze is the charge of the incident particle and I is the effective excitation energy of the absorber material measured in eV. δ is the density effect correction to the ionization energy loss

2.3.2 Particle identification with ITS

The measurement of the energy loss in thin silicon detectors can be used for particle identification (PID) in the non-relativistic region. Four of the six ITS layers (two silicon

strip and two drift detector layers) provide the *dE/dx* measurement that can be combined with the other PID detector measurements. In the case of low-momentum particles or particles that are not reconstructed in the TPC, the ITS is the only source of the PID information. For each track reconstructed in the ITS truncated mean *dE/dx* is calculated.

2.3.3 Particle identification with TPC

Charged particles travelling through the TPC ionize the detector's gas. The Bethe–Bloch equation

$$\langle dE/dx \rangle = \frac{C_1}{\beta^2}\left(\ln(C_2\beta^2\gamma^2) - \beta^2 + C_3\right) \qquad (2.5)$$

with detector-specific constants C_1, C_2, and C_3, relates the mean energy loss per path length, dE/dx, to the velocity β of the particle. This constants are including lot of detector specific effects and its determination is a complex task [40]. Combining the momentum information with the measured dE/dx value yields the particle mass, its identity. Figure 2.5 shows the momentum dependence of the mean energy loss for electrons, muons, pions, kaons, and protons reconstructed in the ALICE TPC. The mean value of the dE/dx distribution at a fixed momentum is Gaussian with the standard deviation determined by the detector properties and the quality of a reconstructed track.

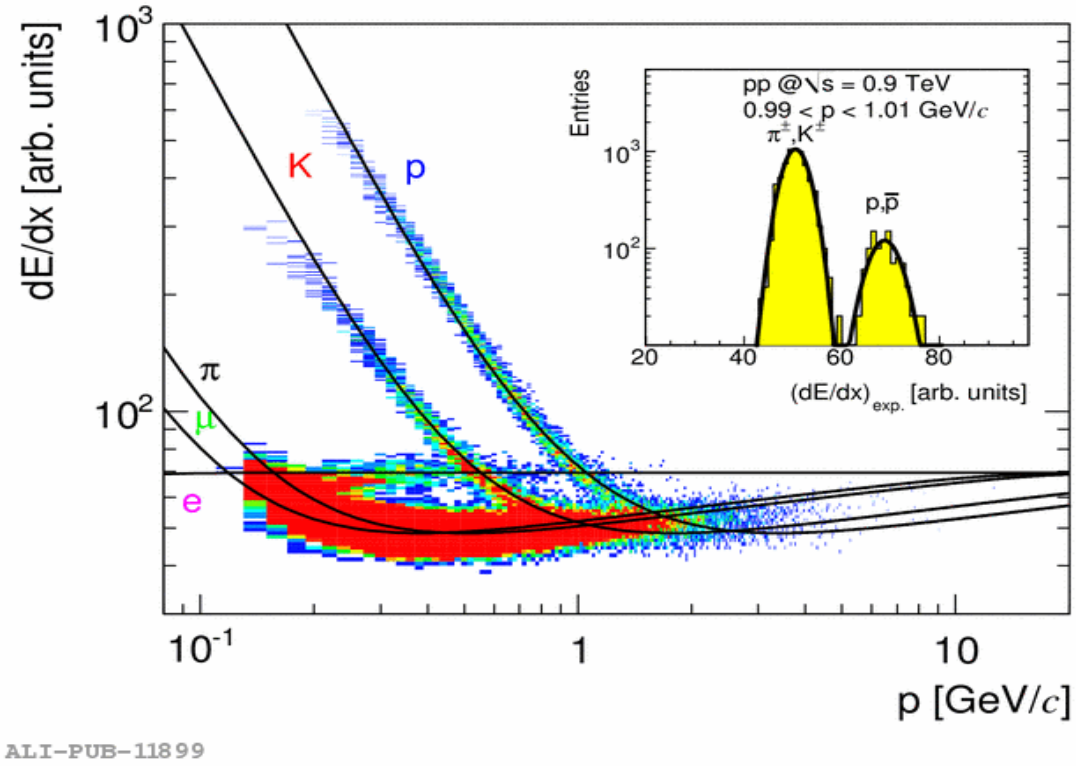

Figure 2.5: The measured ionization per unit length as a function of particle momentum (both charges) in the TPC gas. The curves correspond to expected energy loss for different particle types. The inset shows the measured ionization for tracks with 0.99< p <1.01 GeV/c. The lines are Gaussian fits to the data. Measured by ALICE experiment in proton-proton collisions at √s = 900GeV [17].

2.3.4 Particle identification with TRD

An important task of the TRD is to supplement the TPC electron/pion identification by a pion rejection factor of the order of 100 at momenta in excess of 1GeV/*c*. In addition, by measurement of energy loss, the TRD will improve the identification of other charged particles. In addition to the electron identification, the TRD will also improve the identification of the hadrons. This is done by measuring the d*E*/d*x* in a way similar to that used for the ITS and the TPC.

2.3.5 Particle identification with TOF

Time-Of-Flight (TOF) detector is designed to identify charged particles at intermediate momenta in the ALICE central acceptance ($|\eta| < 0.9$). The starting sample for the track-TOF signal-matching procedure consists of all the TPC tracks which can be successfully extrapolated from the TPC outer wall (at a radius 2.6 m) to the TOF inner radius (3,7 m).

The matching procedure is then organized in two stages:

- In the first step, each track is propagated through the TOF detector, until its extrapolation crosses one of the preselected TOF pads. The time signal of this pad is then associated to the track.
- In the second step, the same procedure, but with a looser criterion, is applied to all those tracks whose extrapolation did not fall within the active area of any of the preselected TOF pads. In particular, the TOF signal closest to the track trajectory is associated, provided that its distance is smaller than a predefined value $d_{\max}$. In Pb–Pb collisions, a distance $d_{\max}$ = 3 cm, which optimizes the ratio between the matching efficiency and contamination in central events, is used. In the case of pp collisions, which are characterized by a much lower charged track density, a more inclusive cut is applied, $d_{\max}$ = 9 cm.

During both steps, the association of the tracks is performed according to the ordering in momentum mentioned above; moreover, once a TOF signal is assigned to a track, it is flagged to prevent any further association to other tracks, to avoid ambiguous track-time assignments.

After the track–TOF signal matching step, the procedure for TOF Particle Identification (PID) is applied to all the reconstructed tracks that have been associated to a signal on the TOF system. For all the reconstructed tracks matched with a signal on the TOF system, the correlation between the track momentum and the mass is:

$$M = \frac{p}{\beta\gamma} = p\sqrt{\frac{(ct_{TOF})^2}{l^2} - 1} \tag{3.2}$$

calculated from the measured time-of-flight t_{TOF}, the reconstructed track length l, and the track momentum p.

3 Analysis and Corrections

Antibaryon-to-baryon ratio was analyzed for four baryon species: Proton, Λ, Ξ and Ω. Three of them Λ, Ξ and Ω, called also hyperons are unstable and contains strange quarks. Strange baryons in ALICE are reconstructed using their weak decay topology in charged particles only. Basic characteristics of analyzed baryons are summarized in the Table 3.1.

	Mass(MeV/c^2)	cτ(cm)	Charged decay	B.R.
$\boldsymbol{p(uud)}$	938.27		-	
$\boldsymbol{\bar{p}(\overline{uud})}$				
$\boldsymbol{\Lambda(uds)}$	1115.68	7.89	$\Lambda \rightarrow p + \pi^-$	0.64
$\boldsymbol{\bar{\Lambda}(\overline{uds})}$			$\bar{\Lambda} \rightarrow \bar{p} + \pi^+$	
$\boldsymbol{\Xi^-(dss)}$	1321.71	4.91	$\Xi^- \rightarrow \Lambda + \pi^-$	0.99
$\boldsymbol{\overline{\Xi^+}(\overline{dss})}$			$\overline{\Xi^+} \rightarrow \bar{\Lambda} + \pi^+$	
$\boldsymbol{\Omega^-(sss)}$	1672.45	2.46	$\Omega^- \rightarrow \Lambda + K^-$	0.68
$\boldsymbol{\overline{\Omega^+}(\overline{sss})}$			$\overline{\Omega^+} \rightarrow \bar{\Lambda} + K^+$	

Table 3.1: Main characteristics of the analyzed particles

Raw measurements, which come from the experiment, are distorted by systematical effects. We need to correct our measurements to these effects to see the real physics. As a consequence of symmetries of the experiment, many detector effects such as the acceptance, the reconstruction and the particle identification ones are the same for particles and anti-particles and thus cancel out in the ratio. They should definitely be considered in the case we want to extract the particle spectra. The systematical effects which do not disappear in ratio, and for which are we going to correct are:

- Absorption
- Contamination by secondary particles
- Cut efficiency

We will be talking about each effect in more detail in dedicated sections.

3.1 Analysis procedure

The analysis is running on the Event Summary Data (ESD) [32] files where reconstructed tracks and also reconstructed secondary vertices – V^0 and cascade, are

stored. In the following dedicated sections we will give an outlook on the analysis for 4 baryon species – primary protons, Λ baryons and Ξ/Ω cascades. By the analysis we mean route from tracks and vertices in ESD to raw, uncorrected ratios (spectra).

Analysis in general is performed in two dimensional phase space with coordinates in rapidity and transverse momentum.

3.1.1 Protons

As was implemented in *AliProtonAnalysisBase* class, we can analyze events and tracks in four different cases: TPC standalone tracking, Hybrid TPC tracking, Full Hybrid TPC tracking and Global tracking.

At the track level, selection criteria were imposed in order to ensure that the quality of the accepted track is the nominal. For a track to be considered, it has to fulfill certain criteria based on the resolution values, the reconstruction flags and the track's relation to the primary vertex. The final imposed cut values are the result of a detailed study performed with the help of the *AliProtonQAAnalysis* class. The track quality criteria are imposed in order to have mainly a sample with reasonable track resolutions.

3.1.1.1 TPC standalone tracking

In the TPC standalone approach, we rely on the first iteration of the tracking which was described before, where the track is extrapolated from the outer to the inner TPC radius. These track parameters are stored in the ESD as a separate data member called *fTPCInner*. In order to retrieve this information, one has to call the *GetTPCInnerParam* function of the *AliESDtrack*, which returns an *AliExternalTrackParam* object.

In parallel, the primary vertex is calculated from these TPC only tracks. In order to retrieve the information of this vertex, one has to call the *GetPrimaryVertexTPC* function of the *AliESDEvent* object. This returns an *AliESDVertex* object from where we can access all the necessary vertex information.

3.1.1.2 Hybrid TPC tracking

The Hybrid TPC approach is based on the TPC tracking described in the previous paragraph. The main difference is that this time the primary vertex information comes from

the Silicon Pixel Detector (SPD) which provides a much more accurate estimation. This means that the TPC tracks have to be related to the SPD vertex (*GetPrimaryVertexSPD*) this time.

In addition, in order to better constrain the track, we request to have some associated ITS clusters. By doing this we reduce significantly the contamination from secondary protons and anti-protons in our track sample. These secondary, are either the products of decay or emerge from the interaction of particle with the detector material.

3.1.1.3 Full Hybrid TPC tracking

The Full Hybrid TPC approach is based on the Hybrid TPC tracking described in the previous paragraph. The main difference is that this time in order to better constrain the track distance to closest approach (*dca*) value we are we rely on full information which comes from tracking (*AliESDtrack*) to extrapolate the track to primary vertex. As a result of this, we can get much better resolution on this variable – decrease of σ of the peak by factor 10.

3.1.1.4 Global tracking

In global tracking approach we rely on full information which comes from tracking. These track parameters are stored in the ESD as *AliESDtrack*. Primary vertex is also calculated from full information. In order to retrieve the information of this vertex, one has to call the *GetPrimaryVertex* function of the *AliESDEvent* object. This returns an *AliESDVertex* object from where we can access all the necessary vertex information.

3.1.1.5 Particle identification

To identify the proton tracks in the sample we are using correlation of particle momenta and specific ionization of the TPC gas.

Two approaches for particle identification with standalone TPC were developed: N-σ approach and Ratio approach both based on *dE/dx* measurement.

The transverse momentum coverage of the analysis is determined by the contamination of the proton sample by another particle species which is starting at ~1 *GeV/c*

N-σ approach

This PID approach is based on defining N-σ area around proton band.

$$N = \frac{\left| dE/dx_{\exp} - dE/dx_{BB} \right|}{dE/dx_{BB} . R} \qquad (3.1)$$

where $dE/dx_{\exp}$ experimental value of ionization losses of a track is, dE/dx_{BB} is ionization loses taken from Bethe-Bloch formula for momentum of a track and expected particle (e,μ, K, p, . . .) mass and *R* is a detector resolution.

This value is obtained for each TPC track, and then a cut is applied on it:

$$N \leq N_{\max} \qquad (3.2)$$

On Figure 3.1 are momentum slices of *dE/dx* in arbitrary units for momenta intervals from 0.4 Gev/c until 1GeV/c. Peak corresponding to proton is the one on the right hand side – you can see, that we can distinguish between proton peak and other particles in all used momentum interval. In N-σ approach we are selecting tracks which are in N_{max} interval from center of peak corresponding to dE/dx_{BB} value.

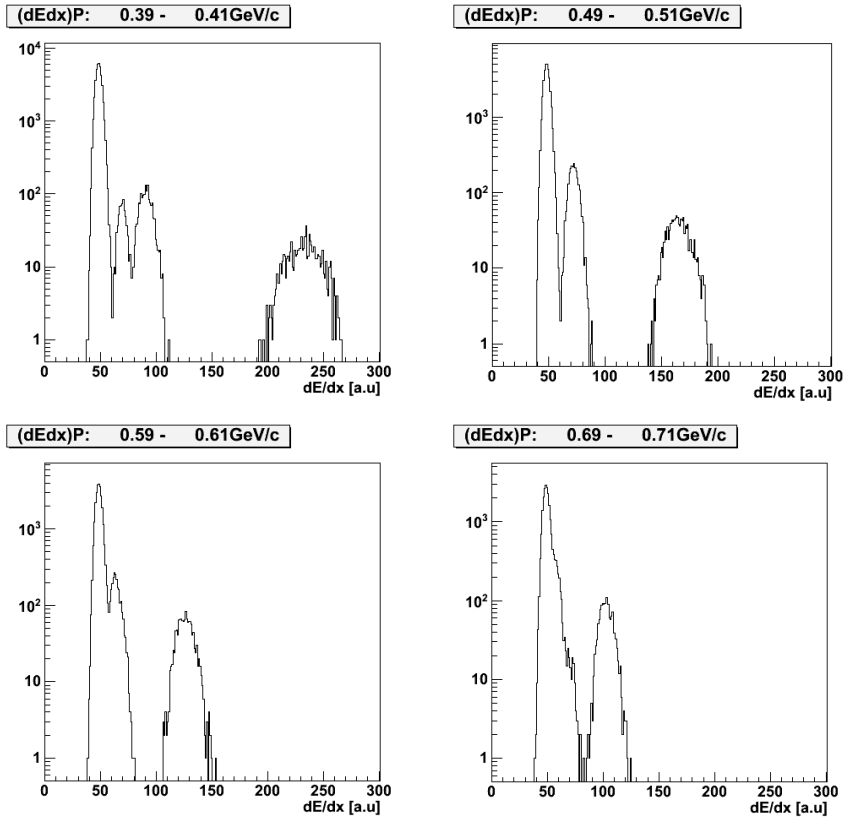

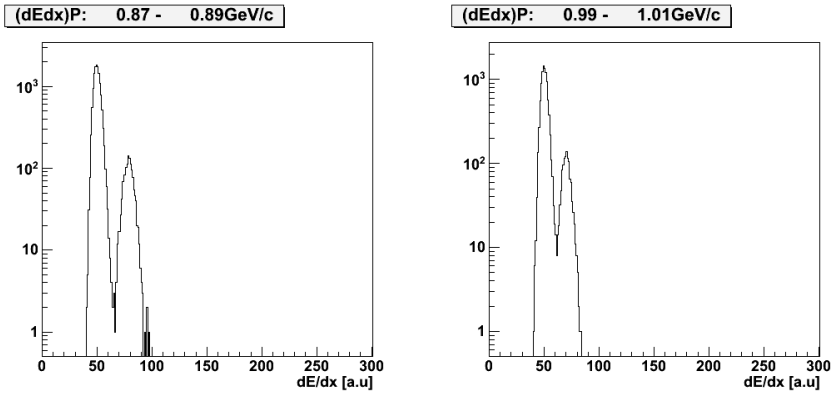

Figure 3.1: The measured ionization per unit length in arbitrary units for different particle momenta intervals. Right hand peak is corresponging to (anti)protons.

Ratio approach

This PID approach is based on variable:

$$Z = \ln\left(\frac{dE/dx_{\exp}}{dE/dx_{BB}}\right), \qquad (3.3)$$

where $dE/dx_{\exp}$ is experimental value of ionization losses for a track and dE/dx_{BB} is ionization loses taken from Bethe-Bloch formula for momentum of a track and expected particle (e,μ, K, p, . . .) mass.

This value is obtained for each TPC track, and then a cut is applied on it:

$$Z \geq Z_{\min} \qquad (3.4)$$

On Figure 3.2 are momentum slices of *dE/dx* in arbitrary units for momenta intervals from 0.4 *Gev/c* until 1 *GeV/c*. Peak corresponding to proton is the one on the right hand side – you can see, that we can distinguish between proton peak and other particles in all used momentum interval. In Ratio approach we are selecting track which have *Z* under Z_{min} value. For example Z_{min} = - *0.2*.

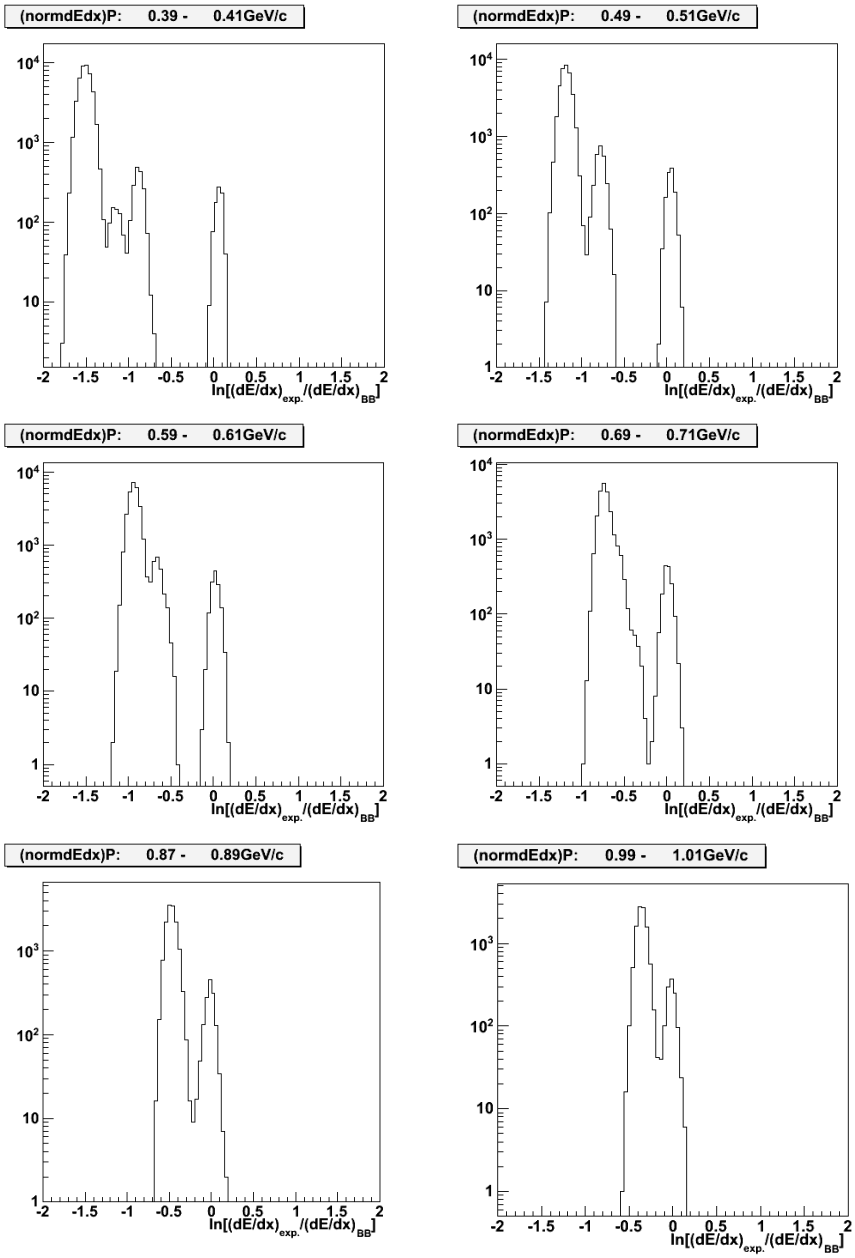

Figure 3.2: Logaritm of the ratio of measured ionization per unit length to expected energy loss of proton for different particle momenta intervals. Right hand peak (around zero) is corresponging to (anti)protons.

After selection of proper high quality track and applying the particle identification with proton hypothesis on it we have a raw uncorrected antiproton-proton ratio as a function of rapidity and transverse momentum

3.1.2 Λ hyperons

Event summary data provides us reconstructed V^0 candidates with all the parameters. The V^0 vertexer with default topological selections is running during reconstruction procedure. Functionality of the vertexer is described in the Section 2.2.3. User can set his own topological selections directly to the vertexer and rerun it in the analysis code or select default V^0s.

The V^0 candidate sample contains the following parts

- Λ baryons
- K^0_s mesons
- γ conversions
- combinatorial background

These parts are visible in the plot often used in V^0 and cascade analysis – the Armenteros Podolanski plot. Historically the Armenteros Podolanski variables have been used to analyze particle decays, in particular those with a V^0 topology such the charged decay modes of Λ and K^0_S. The definitions of the α and p_{tArm} are actually quite simple:

$$\alpha = \frac{p_L^+ - p_L^-}{p_L^+ + p_L^-} \qquad (3.5)$$

where p_L is the momentum component of the + or – daughter parallel to the momentum vector of the parent (in the laboratory frame). p_{tArm} is then the component perpendicular to the parent momentum vector and thus the same in the rest frame of the decay as the lab frame and hence also the same for the + and – daughters.

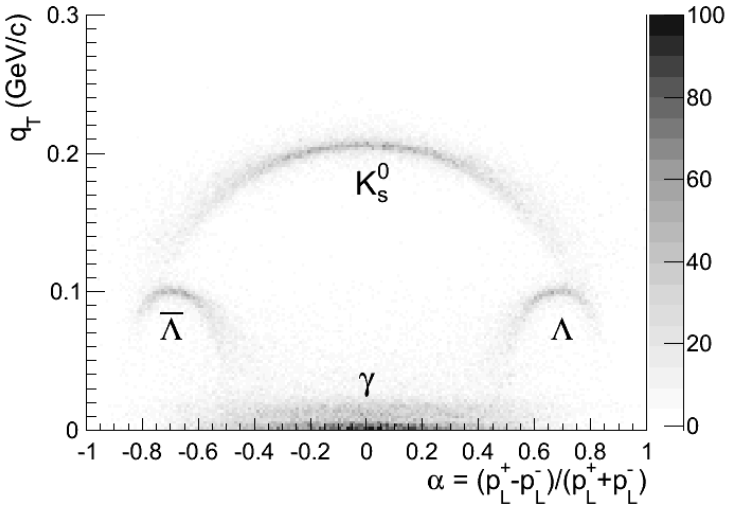

Figure 3.3: Armenteros – Podolanski space for reconstructed V^0 tracks. Different particle species are shown [35].

The goal of proper topological selections is to decrease combinatorial background, which lies all over Armenteros-Podolanski space.

Identification of Λ baryons from the rest of the V^0 candidates is performed using invariant mass spectrum with Λ mass hypothesis. Λ signal is clearly visible and can be easily distinguished from the background.

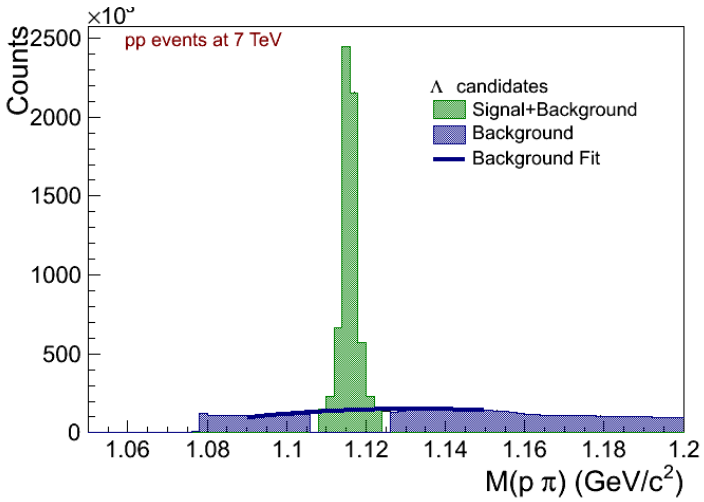

Figure 3.4: Picture ilustrating extraction of signal and background from invariant mass distribution of Λ. Areas cosidered as signal+background (green) or pure background (blue) are shown. The line corresponds to polynomial fit of background areas.

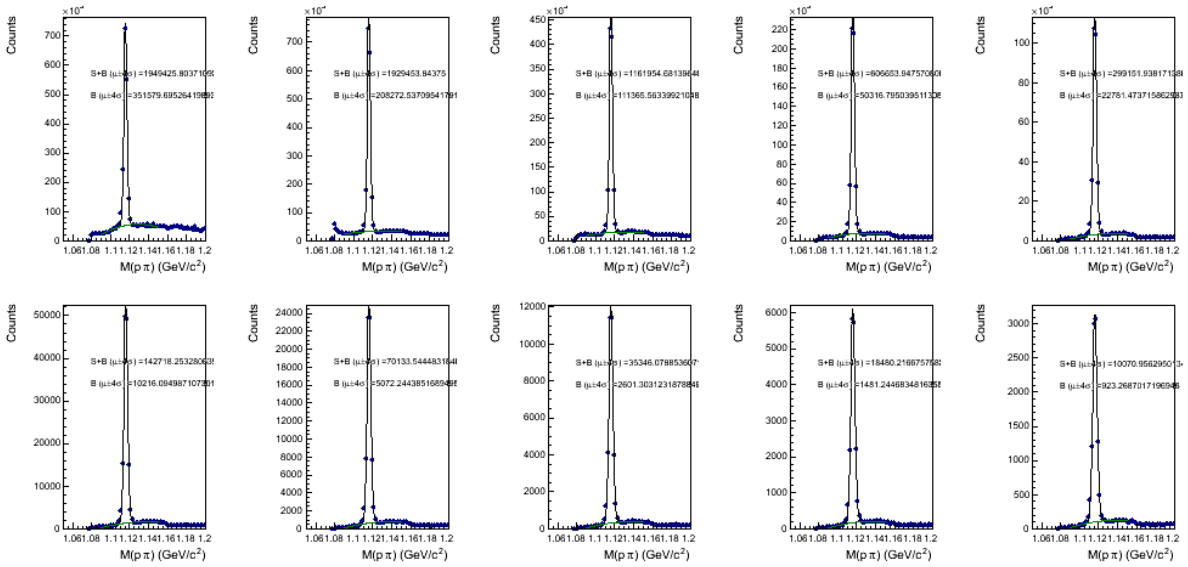

Figure 3.5: Invariant mass distribution with Λ hypothesis for different transverse momenta intervals.

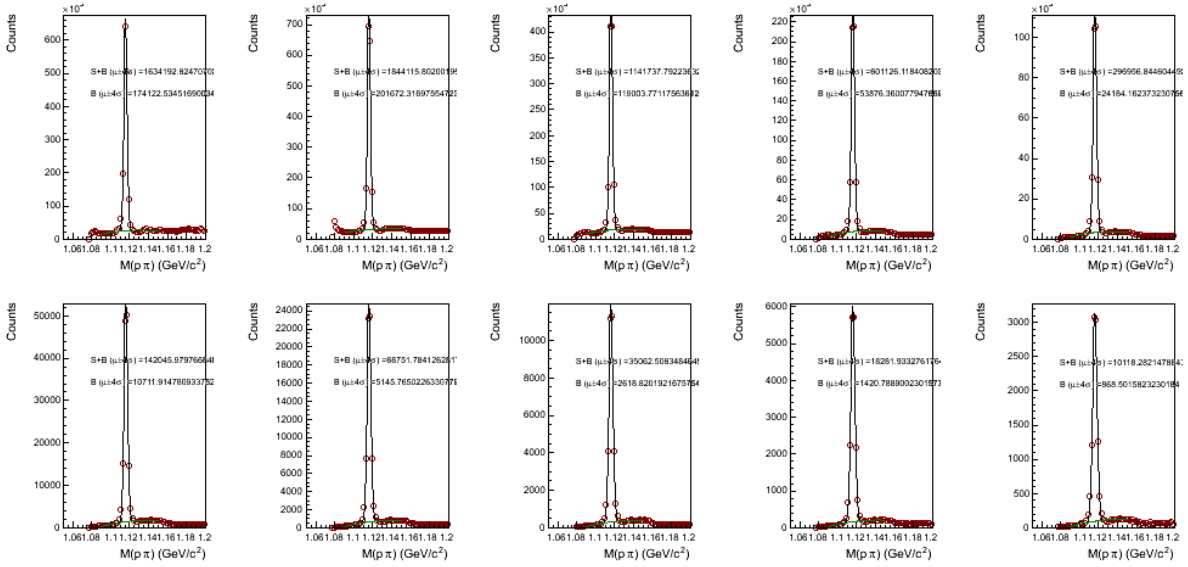

Figure 3.6: Invariant mass distribution with $\bar{\Lambda}$ hypothesis for different transverse momenta intervals.

As a first step, the invariant mass distribution is fitted by sum of Gaussian and second order polynom. Here we are extracting Gaussian mean and width (sigma) of Gaussian peak, which are used afterwards in Signal/Background extraction procedure.

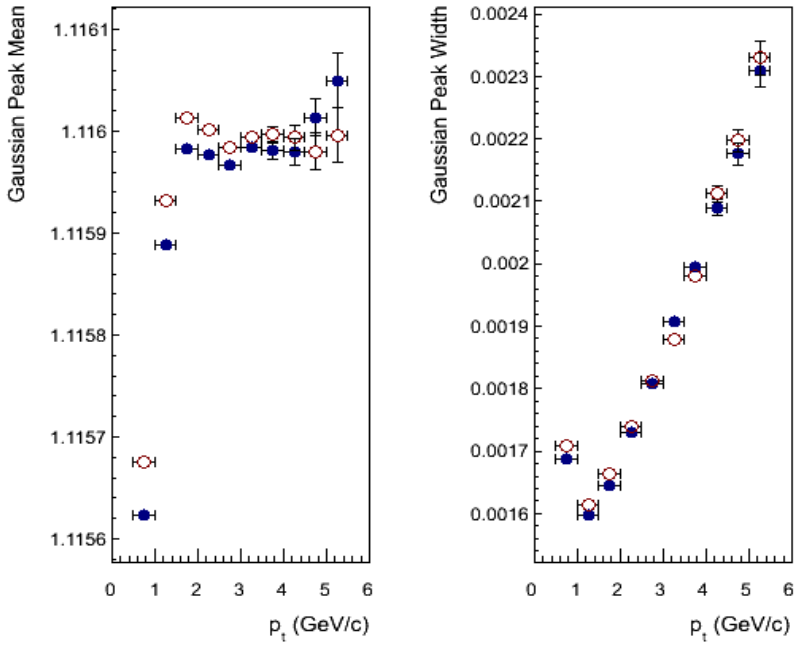

Figure 3.7: Gausian mean and width of the peak in invariant mass distribution for Λ(full points) and $\bar{\Lambda}$ (open points) as a function of V^0 transverse momentum

Three methods were developed for signal/background evaluation: Bin counting method, and two methods using fit with different functional forms.

Bin counting

As Signal + Background we are using an integral of Invariant mass histogram in 4σ area around mean of Gaussian peak. We assume that in areas farther then 6σ from mean of Gaussian peak is pure background – this assumption is coming from Monte Carlo simulation. The overall height of background is evaluated in these areas, as an average of Bins content. Overall height is then used to evaluate the Background in 4σ area around mean of Gaussian peak.

Fit with split function

As Signal + Background we are using an integral of Invariant mass histogram in 4σ area around mean of Gaussian peak. We assume that in areas farther then 6σ from mean of Gaussian peak is pure background – this assumption is coming from Monte Carlo simulation. The background areas are fitted by simultaneously by splitted function, second order polynom. Splitted function means that we are rejecting points closer than 6σ from mean of the peak from the fit. Parameters from such a fit are then used to extrapolate the

function into 4σ area around mean of Gaussian peak. Background is evaluated from this extrapolated function.

Fit with sum of Gaussian and second order polynom

Signal/Background in this case is extracted directly from the first fit by Gaussian and second order polynom sum. As Signal + Background we are using an integral of Invariant mass histogram in 4σ area around mean of Gaussian peak. As Background we are using an integral of the 2order polynom from the fit in 4σ area around mean of Gaussian peak.

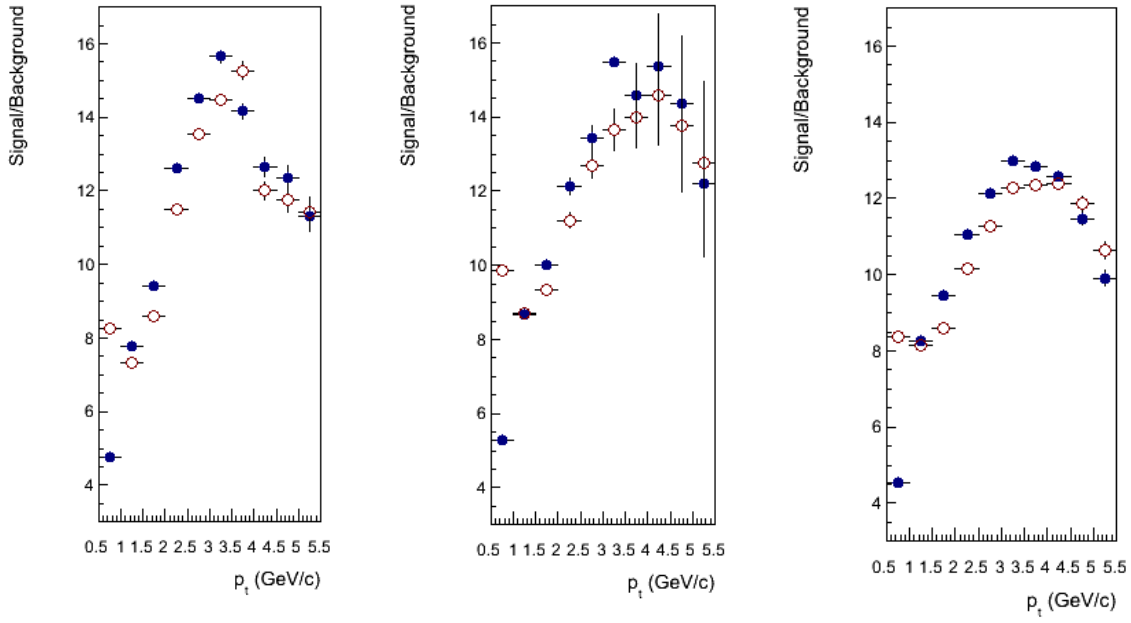

Figure 3.8: Signal-to-background ratio for Λ(full points) and $\bar{\Lambda}$ (open points) as a function of V^0 transverse momentum. Values are evaluated using „Fit with sum of Gaussian and second order polynome" (left), „Fit with split function"(middle) and „Bin counting"(right) method.

The comparison of signal-to-background ratio as a function of transverse momentum extracted using methods described before you can see on Figure 3.8. Large difference in the ratio between particle and antiparticle visible up to ~1GeV/c is due to secondary protons created in material which are increasing combinatorial background for Λ. We will talk about this effect in detail latter in the dedicated section.

3.1.3 Cascades Ξ and Ω

Event summary data provides us reconstructed cascades with all the parameters. The cascade vertexer with default topological selections is running during reconstruction procedure. Functionality of the vertexer is described in the Section 2.2.3. User can set his own topological selections directly to the vertexer and rerun it in the analysis code or select default cascades.

Cascades candidate sample contains Ξ and Ω baryons plus combinatorial background. These parts are visible in Armenteros – Podolanski plot for cascades – Figure 3.9.

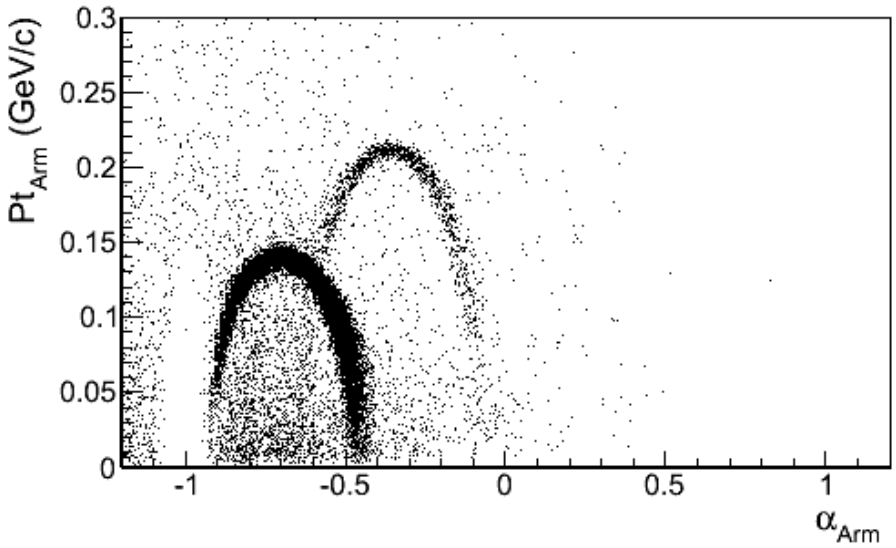

Figure 3.9: Armenteros – Podolanski space for reconstructed cascade tracks. Band with higher statistics (left one) coresponds to Ξ, the low statistics band (right one) to Ω

Here all particles are on one side. We can multiply x axis by charge of the cascade and then we will see particles sorted by charge on both sides of the plot.

Identification of Ξ and Ω baryons is performed using invariant mass spectrum with proper mass hypothesis. Ξ and Ω signal is clearly visible and can be easily distinguished from the background.

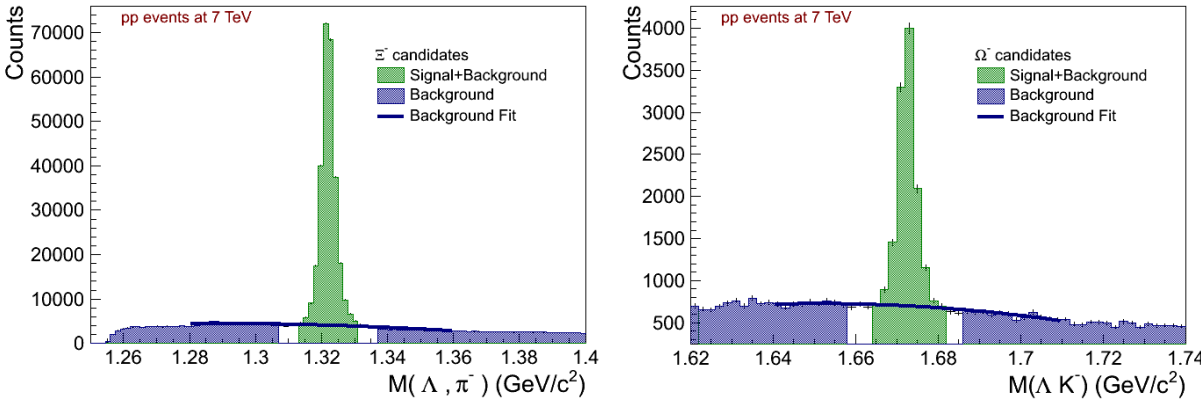

Figure 3.10: Picture ilustrating extraction of signal and background from invariant mass distribution of Ξ^- (left) and Ω^- (right). Areas cosidered as signal+background (green) or pure background (blue) are shown. The line corresponds to polunomial fit of background areas.

The same methods for Signal/Background extraction as are used for Λ and were described in previous section are used for Ξ and Ω too.

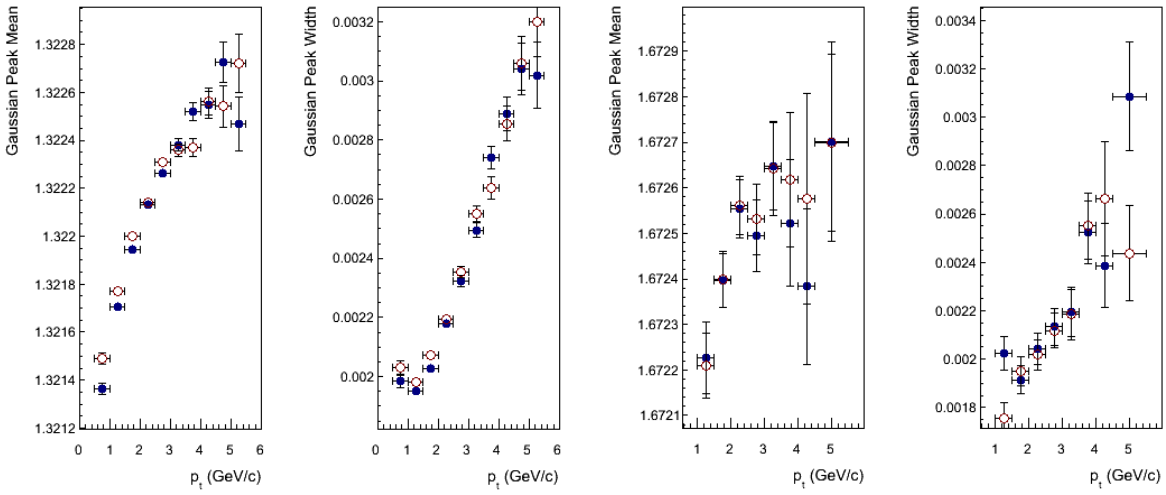

Figure 3.11: Gausian mean and width of the peak in invariant mass distribution for Ξ^- (full points left) and Ξ^+ (open points left) or Ω^- (full points right) and Ω^+ (open points right) as a function of cascade transverse momentum

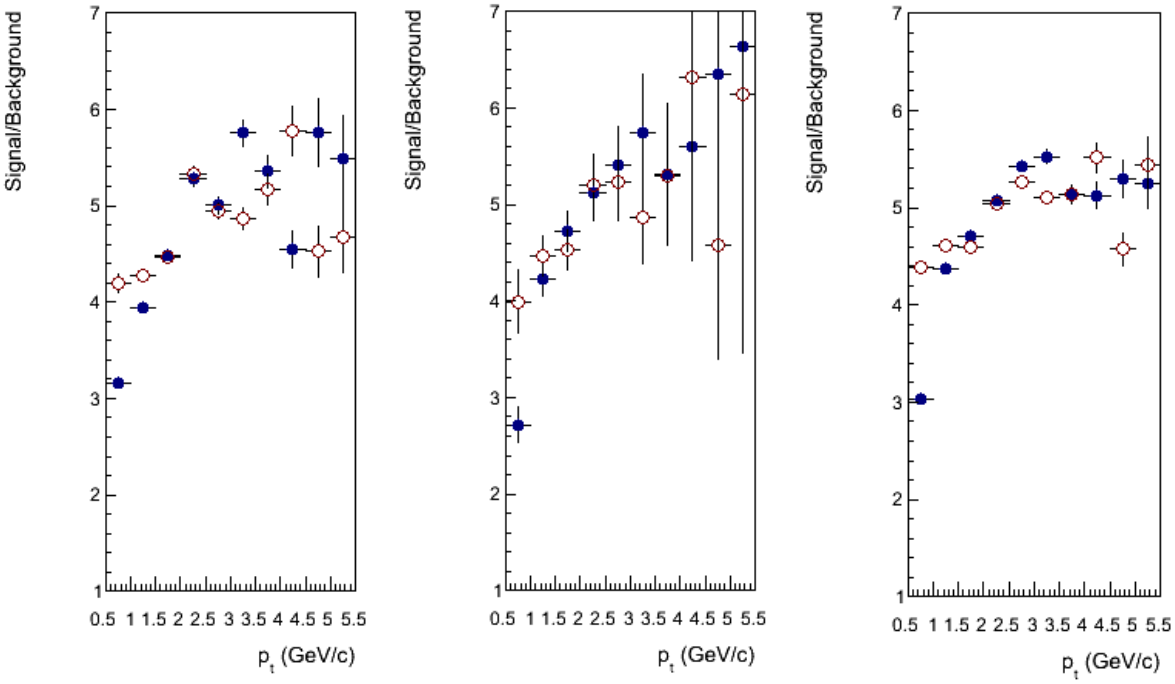

Figure 3.12: Signal-to-background ratio for Ξ^- (full points) and Ξ^+ (open points) as a function of cascade transverse momentum. Values are evaluated using „Fit with sum of Gaussian and second order polynome" (left), „Fit with split function"(middle) and „Bin counting"(right) method.

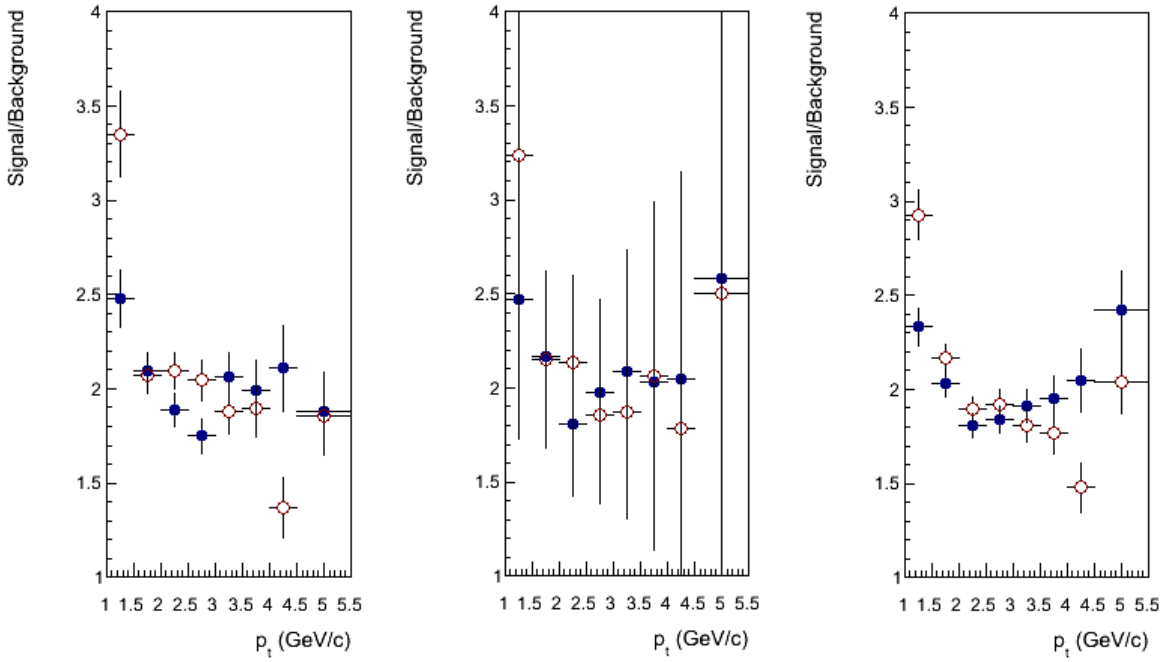

Figure 3.13: Signal-to-background ratio for Ω^- (full points) and Ω^+ (open points) as a function of cascade transverse momentum. Values are evaluated using „Fit with sum of

Gaussian and second order polynome“ (left), „Fit with split function“(middle) and „Bin counting“(right) method.

It is clear from the previous plots that disadvantage of the second method – fit with splited function is quite large uncertainty. This method is used only for cross checks. Bin counting method is robust with respect to statistical errors in the input distributions and thus will be used in situations where small statistics is a serious problem. We will use the third method, the fit with sum of Gaussian and second order polynom as a default method in all situations where we have good enough statistics for stable fit.

3.1.4 Attempt to decrease the background

Background is increasing in a way to higher rapidity and lower transverse momentum so the highest values are in the high rapidity – low p_t corners of the phase space. Several methods were used to decrease the background

- Particle identification of daughter tracks
- Cut on K^0_s invariant mass in case of Λ
- Cut in Ξ invariant mass in case of Ω

Particle identification is applied for all daughter tracks and is based on correlation of particle momenta and specific ionization of the TPC gas. The way we are using this is the same as for protons and was described before. This time we are using also pion and kaon band.

Particle identification for daughter tracks helps to decrease combinatorial background in general for all hyperons and also K^0_s – Λ contamination and Ξ – Ω contamination coming from regions in Armenteros Podolanski plots where the areas of different particles overlap. Significant decrease we can see in the region of γ conversions.

Cut on invariant mass of complementary particle for Λ and Ω is removing all candidates which fall into $10 MeV/c^2$ area around nominal value of the K^0_s or Ξ mass.

Effect of these additional cuts for Λ in the corner bin $0.6 < y < 0.8$ and $p_t > 0.6$ GeV/c you can see on the Figure 3.14.

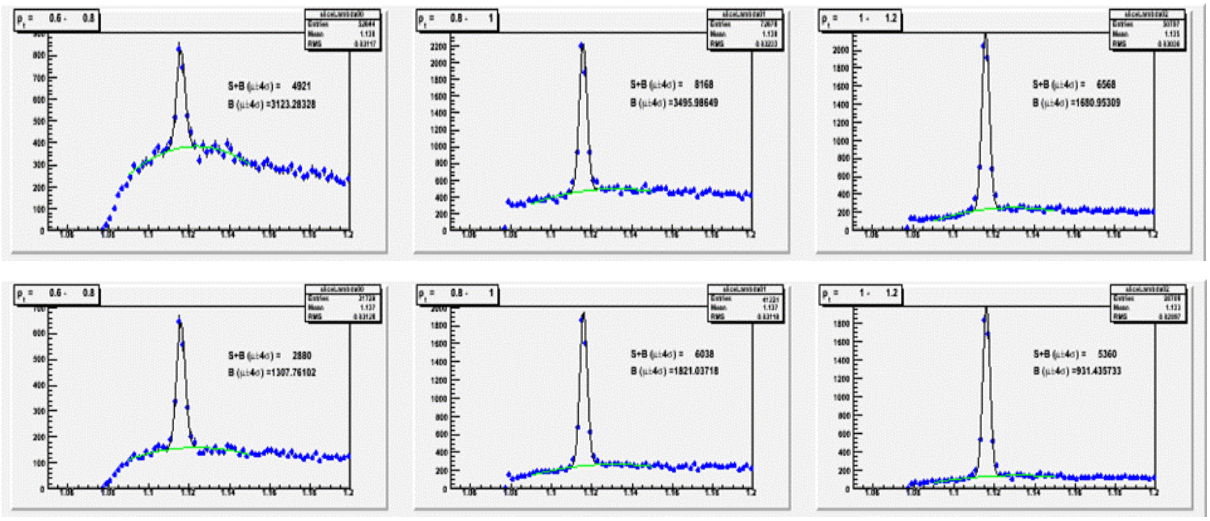

Figure 3.14: Picture ilustrating decrease of combinatorial background in invariant mass distribution with Λ hypothesis by using particle identification and cut of on K^0_s mass. Three lowest bins in transverse momentum are shown before (up) and after (down) additional selections.

Using these selections we can decrease the background in the problematic regions more than two times. Effect is nicely visible on the Armenteros Podolanski plot, Figure 3.15.

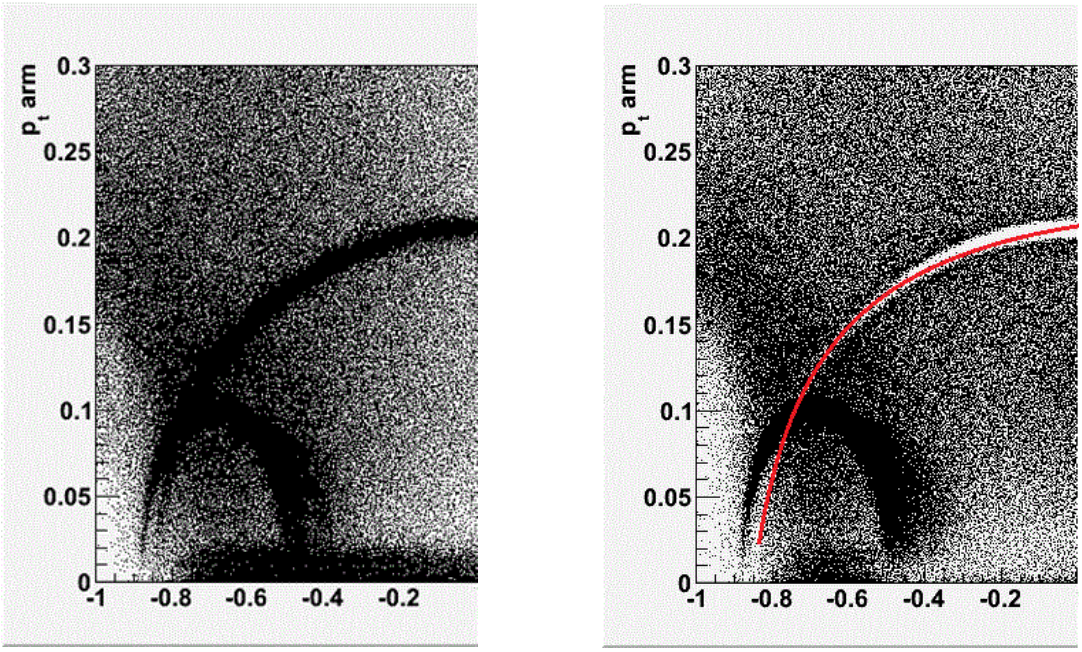

Figure 3.15: Picture ilustrating cut in invariant mass distribution with K^0_s mass hypothesis excluding candidates in 10MeV/c2 area around K^0_s nominal mass, before (left) and after (right) the cut . Λ candidates are in overlap area are not fully affected.

The rest part of γ conversions in |α| around 0.7 are electron – positron pairs with large asymmetry in momentum between these two. Such a electrons falls into momentum regions *p<0.1 GeV/c* and *p>1 GeV/c* where proton band and electron band in *dE/dx* overlaps and thus these electron-positrons are misidentified and remains as a contamination.

Another interesting effect is that cut excluding the V^0 candidates consistent with the K^0 mass, under the hypothesis that the daughters are both pions, did not cut through the Λ population in the Armenteros-Podolanski diagram. The reason of this is that Armenteros-Podolanski diagram is not relativistic invariant.

By considering the decay in the rest frame with an angle θ one can write the p_{tArm} variable as $p.sin\theta$ and α as

$$\alpha = \frac{2p_{cms}}{\beta . M} . \cos\Theta + \frac{m_1 - m_2}{M} \qquad (3.6)$$

One can then produce a plot with θ varying from 0 to π showing the allowed values for the case where β approaches 1

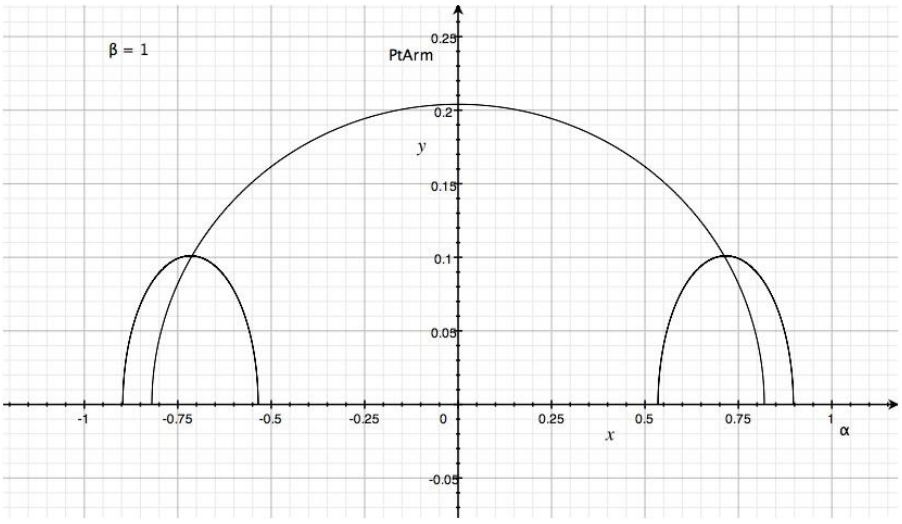

Figure 3.16: Curves corresponding to Λ and K^0_s decays in Armenteros – Podolanski space for β = 1. K^0_s line is intersecting the Λ lines.

The approximation *β=1* is good for fixed-target and cosmic ray experiments but in a collider at central rapidity the typical momenta are such that this is not true, especially at the lowest p_t. Below is the plot for *β=0.8* where it can be seen that K^0 are no longer

intersecting the other particles. In this case cutting those candidates consistent with the K^0 invariant mass will not cut out any real Λ candidates.

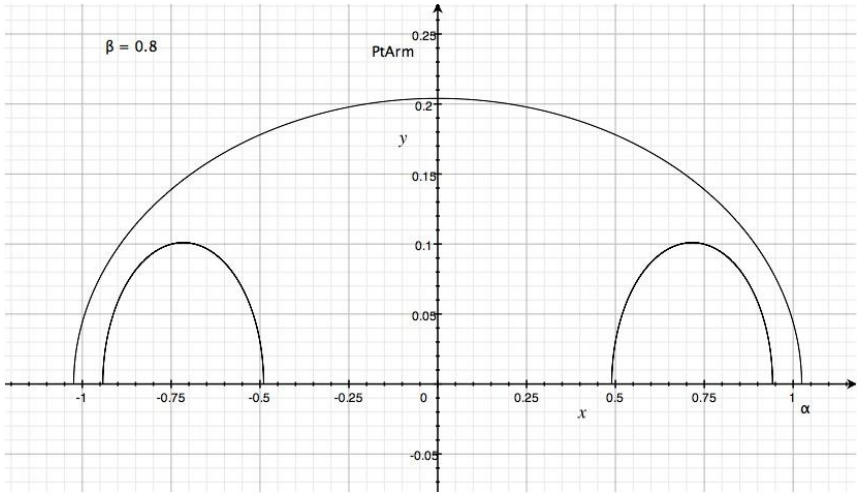

Figure 3.17: Curves corresponding to Λ and K^0_s decays in Armenteros – Podolanski space for β = 0.8. K^0_s line is intersecting the Λ lines.

β=0.8 corresponds to a total momentum of 550 MeV for K^0_s or 1.5 GeV for Λ so not a particularly extreme case.

3.2 Corrections

The TPC [25] of the ALICE experiment is symmetric around mid-rapidity and has full azimuthal coverage. As a consequence, many detector effects such as the acceptance, the reconstruction and the particle identification ones are the same for particles and anti-particles and thus cancel out in the ratio. However, there is a mechanism that causes differences and needs to be taken into account.

Technically, the correction matrices are stored in histograms the binning of which is set in such a way to match the one used in the actual analysis. The latter is chosen to be as close to the variable's resolution as possible but also to give a reasonably low statistical error.

3.2.1 Absorption effects

By absorption we mean the interaction of either the baryon or the anti-baryon with another particle resulting into the disappearances of the first. For unstable hyperons by

absorption we mean absorption of mother and all daughters – if mother or one of the daughters were absorbed, then hyperon is considered as unreconstructible. This mechanism is directly related to the interaction cross section of the particle with the material. On Figure 3.18 you can see distribution of absorption vertex in *xy* and z planes for protons and antiprotons. Number of absorption vertices corresponds to amount of absorption. One can clearly see higher absorption for antiprotons.

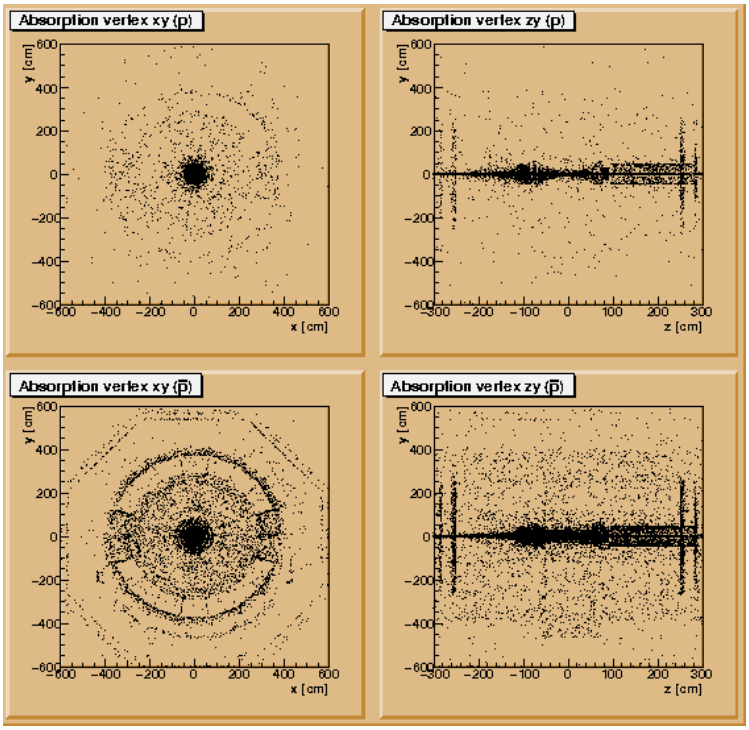

Figure 3.18:Absorption vertex distribution in xy and zy plane for protons and antiprotons. Stronger absorption in case of antiprotons is evident.

To derive absorption correction maps for charged stable particles – proton, kaons and pions, we are looping over simulated data and accumulate information on the 2-dimensional y-p_t grids using AliCFContainer-type object. We are using 3-level AliCFContainer with these stages: Generated Monte Carlo particles (protons), reconstructible proton tracks and reconstructed tracks. Following criteria (cuts) are used to choose inputs to the stages (see Figure 3.19):

- Generated Monte Carlo particles: Primary particles with rapidity and transverse momentum in the selected interval corresponding to data phase space.
- Reconstructible particles: Particles which belongs to "Generated MC particles" which have at least one track reference in TPC.

- Reconstructed tracks: Reconstructed tracks which belong to particle from "Generated MC particles". To choose these tracks we are using *AliESDTrack::GetLabel()* function, which provides connection between ESD and MC.

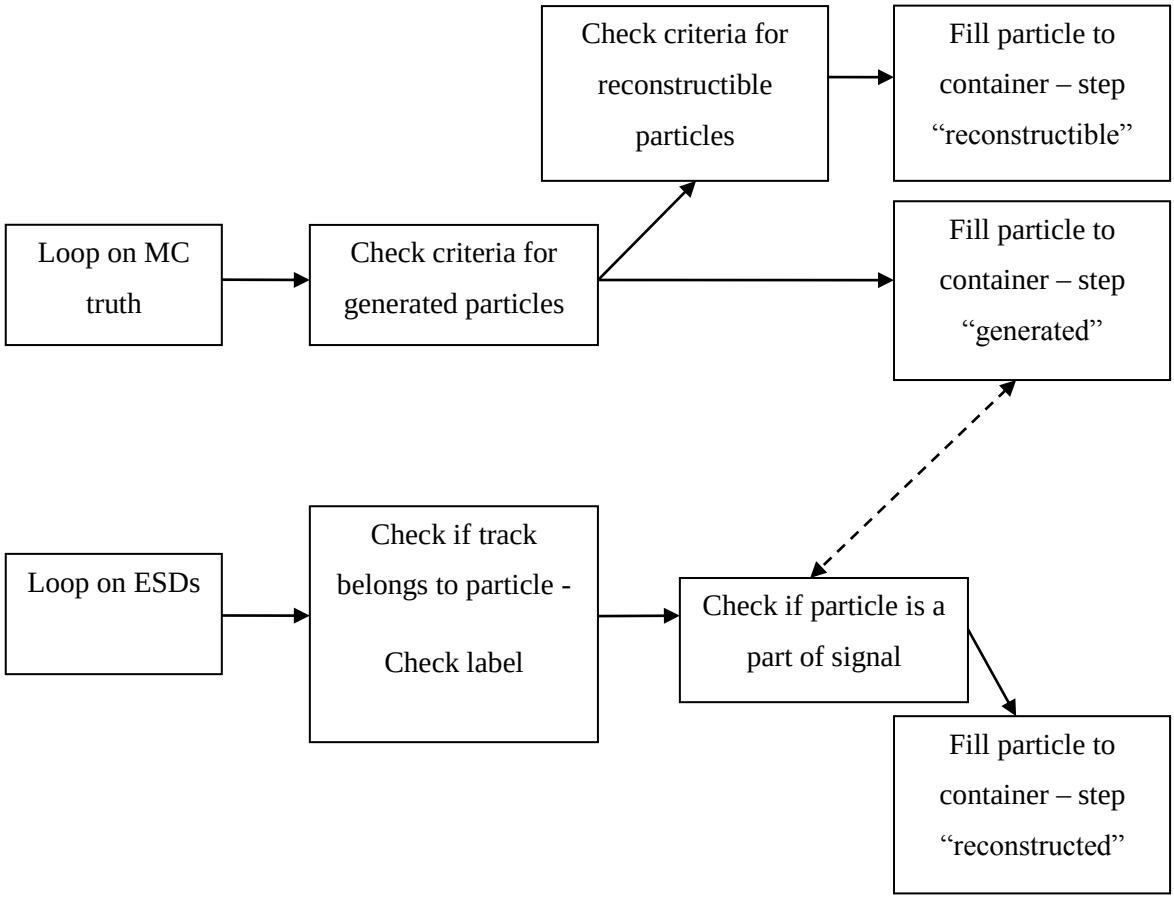

Figure 3.19: Diagram ilustrating absorption efficiency extraction procedure

After that the correction maps, are derived and stored in AliCFEffGrid-type objects. Absorption correction efficiency is obtained as ratio of stages 3 and 1:

$$\varepsilon = \frac{N_{reconstructed}}{N_{generated}}. \qquad (3.7)$$

Since the macroscopic inelastic cross section is different for different baryon species – protons, Λ, Ξ and Ω, as you can see on the Figure 3.19, we have to quantitate also absorption of unstable baryons before decay.

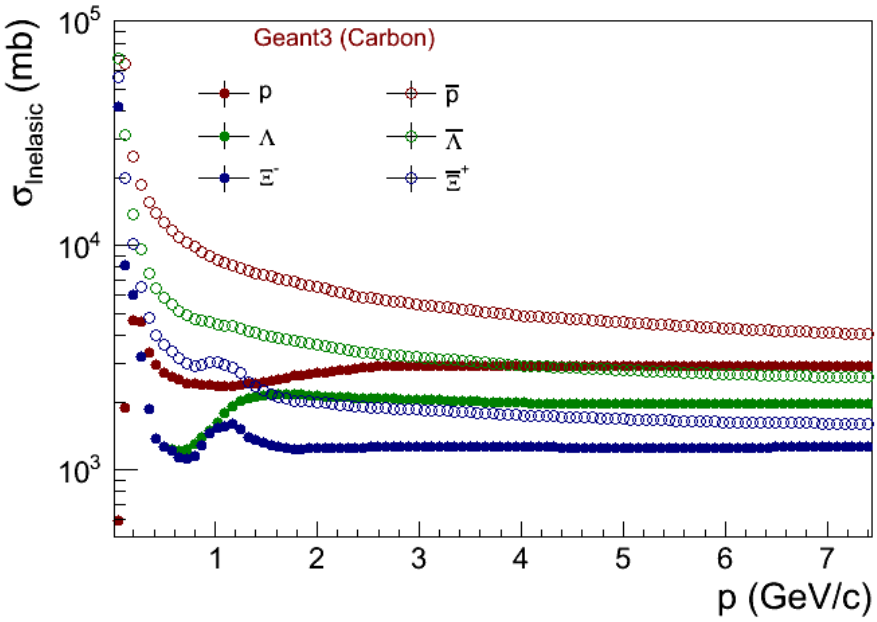

Figure 3.20: Particle – Carbon inelastic cross section as a function of particle momentum. Curves were extracted from Geant3.

To derive absorption correction maps for mother particles – Λ, Ξ and Ω before decay we are looping over simulated data and accumulate information on the 2-dimensional y-p_t grids using AliCFContainer-type object. We are using 2-level AliCFContainer with these stages: Generated Monte Carlo particles and Reconstructible particles. Following criteria were used to choose inputs to the stages:

- Generated Monte Carlo particles: Primary particles with rapidity and transverse momentum in the selected interval corresponding to data phase space.
- Reconstructible particles: Particles which belongs to "Generated MC particles" which have all the proper daughter particles with respect to the measurable decay mode.

Absorption correction efficiency is obtained as ratio of stages 2 and 1:

$$\varepsilon = \frac{N_{reconstructible}}{N_{generated}}. \qquad (3.8)$$

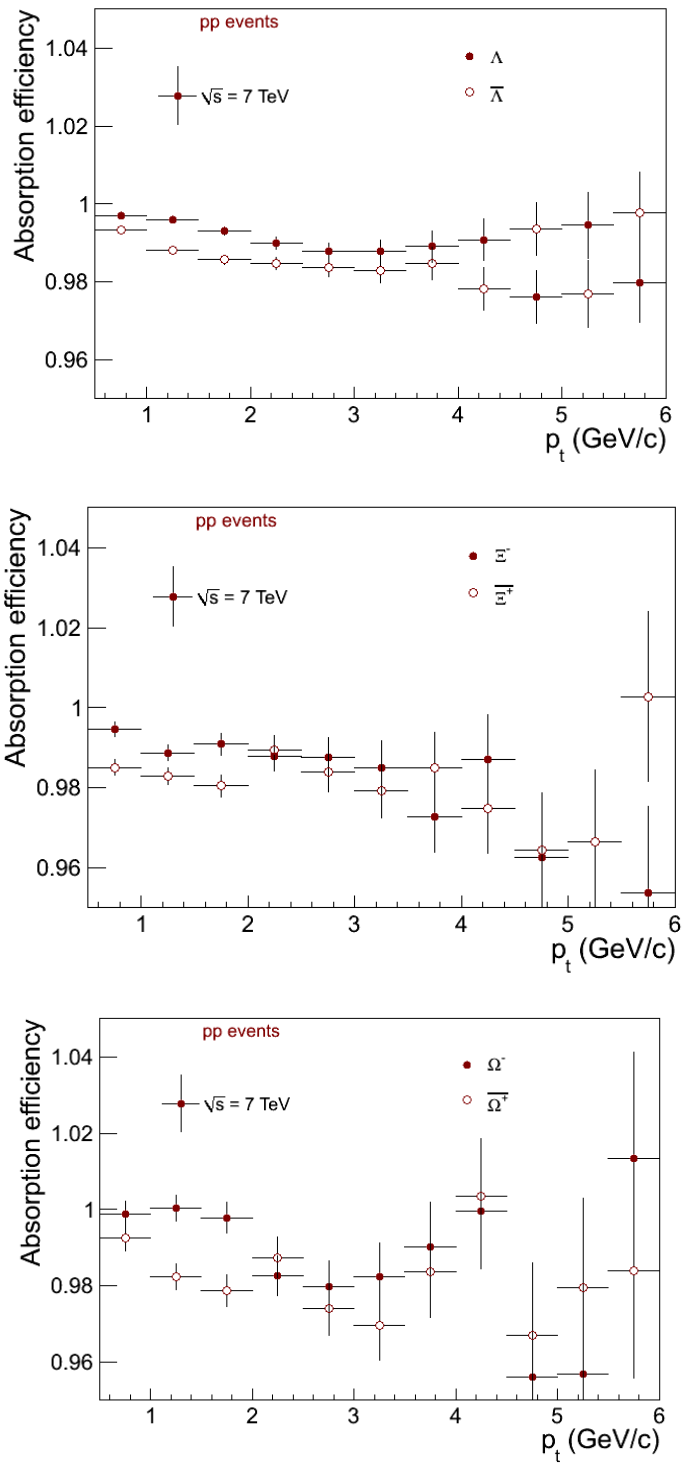

Figure 3.21: Absorption efficiency of Λ (up), Ξ(middle) and Ω(down) mothers before decay. Full point corresponds to particles, open points to antiparticles

As you can see on the Figure 3.21 absorption effect for mother particles is quite small. This is due to short track of the mother. Λ is crossing only SPD, Ξ even only first SPD layer. We can see that absorption effect vanishes at $p_t \sim 4GeV/c$. Due to large uncertainties in the

absorption efficiencies of mother particles we chooses to use only overall corrections for the ratio which are summarized in the Table 3.1.

Mother absorption correction factors		
Λ	Ξ	Ω
1,005	1,01	1,01

Table 3.2: Correction factors for absorption of mother particles in ratio

3.2.2 Cross section effect in the absorption

The absorption correction factors rely, among other things, on the proper description of the inelastic cross-sections used as input by the transport model (GEANT3 [36]). In order to study in detail the uncertainties originating from the different models, full simulations using different transport codes (i.e.GEANT3, FLUKA [37]), were performed. The antiproton – nucleus inelastic cross section which these models used as input were compared to the experimental measurements [38]. It was found that the cross sections used as input in GEANT3 overestimate the experimentally measured cross sections, whereas FLUKA describes the data very well. This is illustrated in Figure 3.22, where the macroscopic inelastic cross section of antiproton – nucleus (up) and proton- nucleus (down), is plotted as a function of the (anti)proton's momentum.

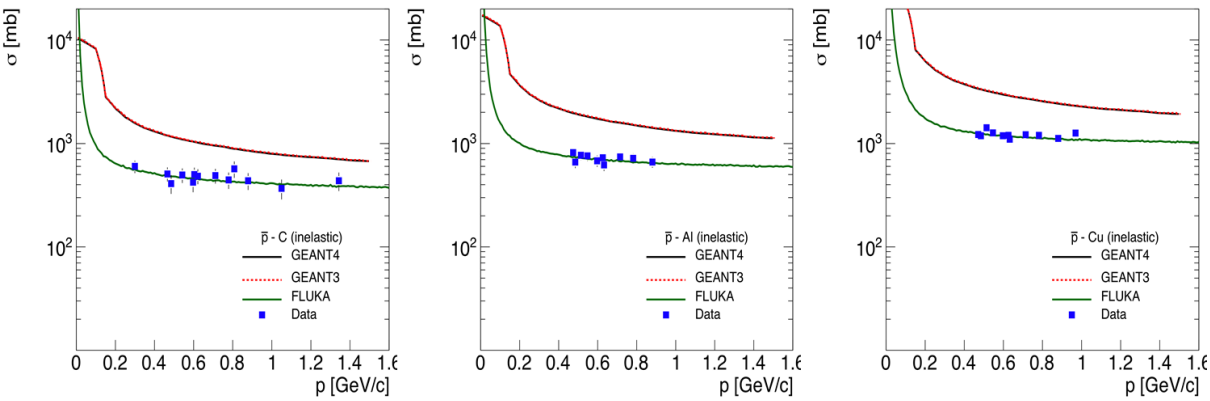

Figure 3.22: [39] The momentum dependence of the antiproton – Nucleus inelastic cross-section for C(left), Al(middle) and Cu(right). The different curves represent the parameterization used in GEANT3 (dashed red line), GEANT4 (solid black line) and FLUKA (solid green line). The full points are the cross-section values measured experimentally.

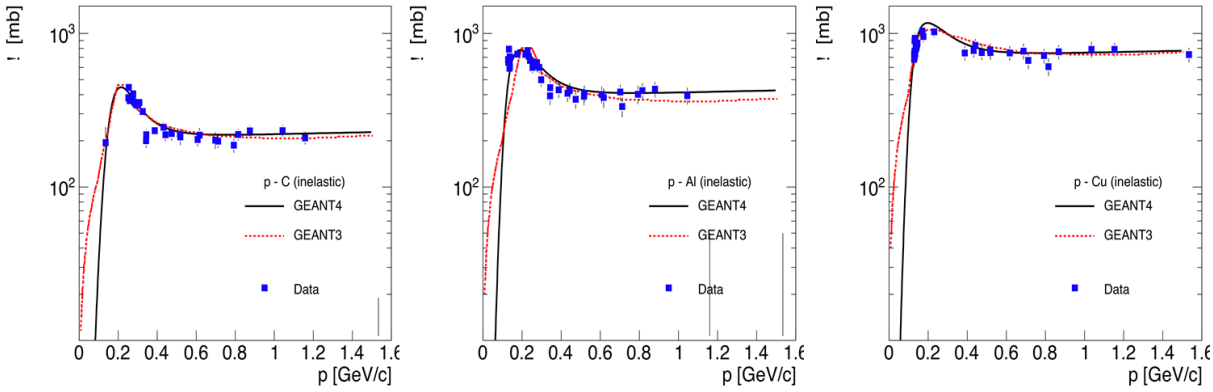

Figure 3.23:[39] The momentum dependence of the proton – Nucleus inelastic cross-section for C(left), Al(middle) and Cu(right). The different curves represent the parameterization used in GEANT3 (dashed red line), GEANT4 (solid black line) and FLUKA (solid green line). The full points are the cross-section values measured experimentally

Though for proton – nucleus, GEANT3 and GEANT4 describe the data points, the discrepancy between the GEANT3 and the FLUKA curves that describe the experimentally measured values for antiproton – nucleus is clearly seen. To account for this difference, the absorption correction factors were scaled to match the correct (FLUKA) cross section parameterization. Final values were fitted and extrapolated to high transverse momentum. Correction functions are used for antiprotons, but we rely on the information from FLUKA even for protons and negative kaons where the difference is much smaller. Functions can be seen on Figure. 3.24.

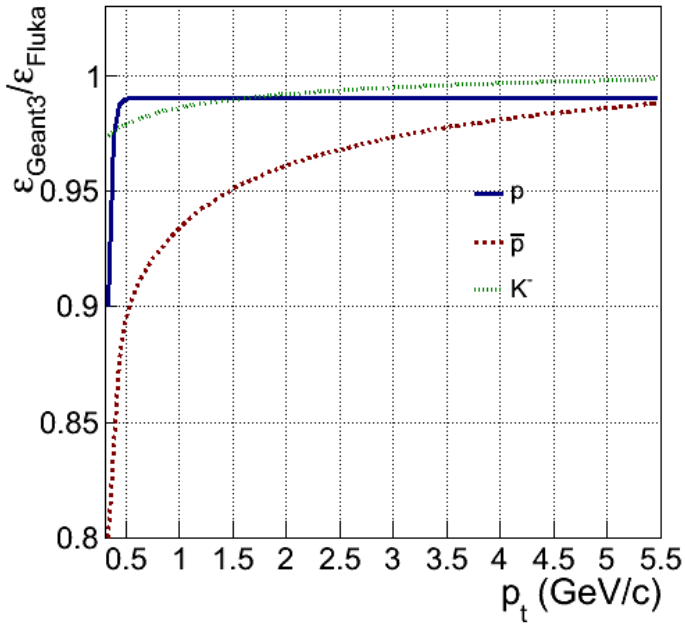

Figure 3.24: Functions corresponding to ratio of absorption efficiency extracted using Geant3 and Fluka transport code.

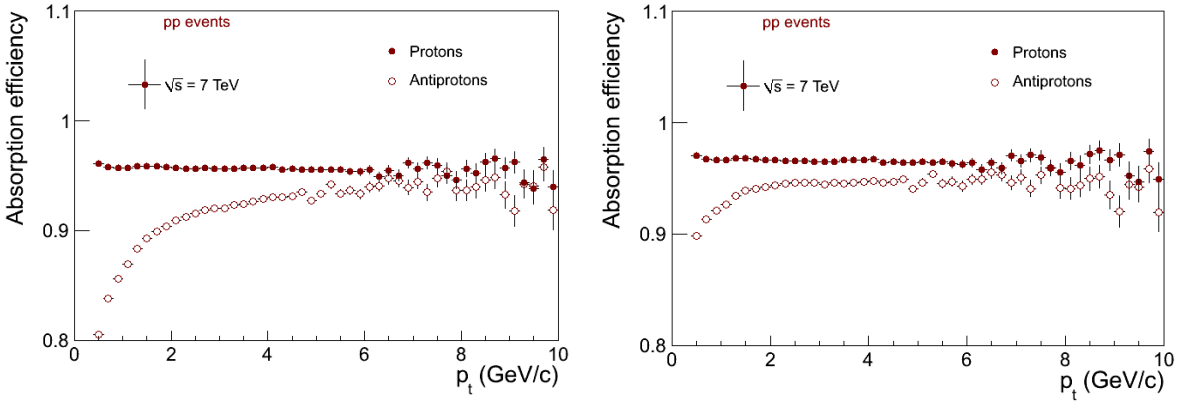

Figure 3.25: Absorption efficiency of protons (full points) and antiprotons (open points) before (left) and after (right) correction for proper inelastic cross section

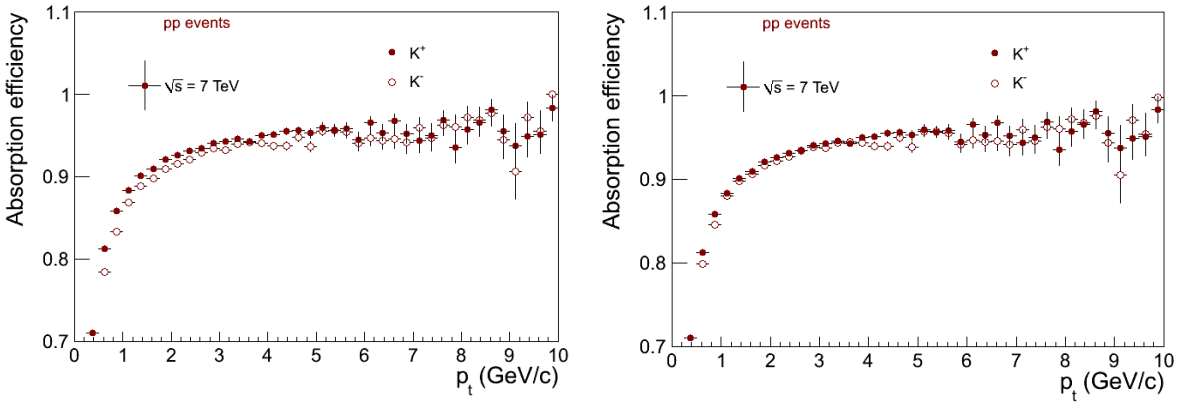

Figure 3.26: Absorption efficiency of K^+ (full points) and K^- (open points) before (left) and after (right) correction for proper inelastic cross section

3.2.3 Secondary particles produced in material

Significant background from secondary particles produced in material can be seen in proton and Λ sample. In both cases the contamination affects only particle sample and antiparticles are background free.

3.2.3.1 Protons

Secondary protons pushed form the material can be distinguished from either primary or feed-down protons in distance of closest approach (*dca*) distribution. The feature of particles produced in material is rather flat distribution in *dca*.

The effect is more pronounced at low p_t. You can see on the Figure 3.27 that background can be decreased by cut on *dca* but some fraction will still remain in the sample since there are secondary particles even at small *dca* values.

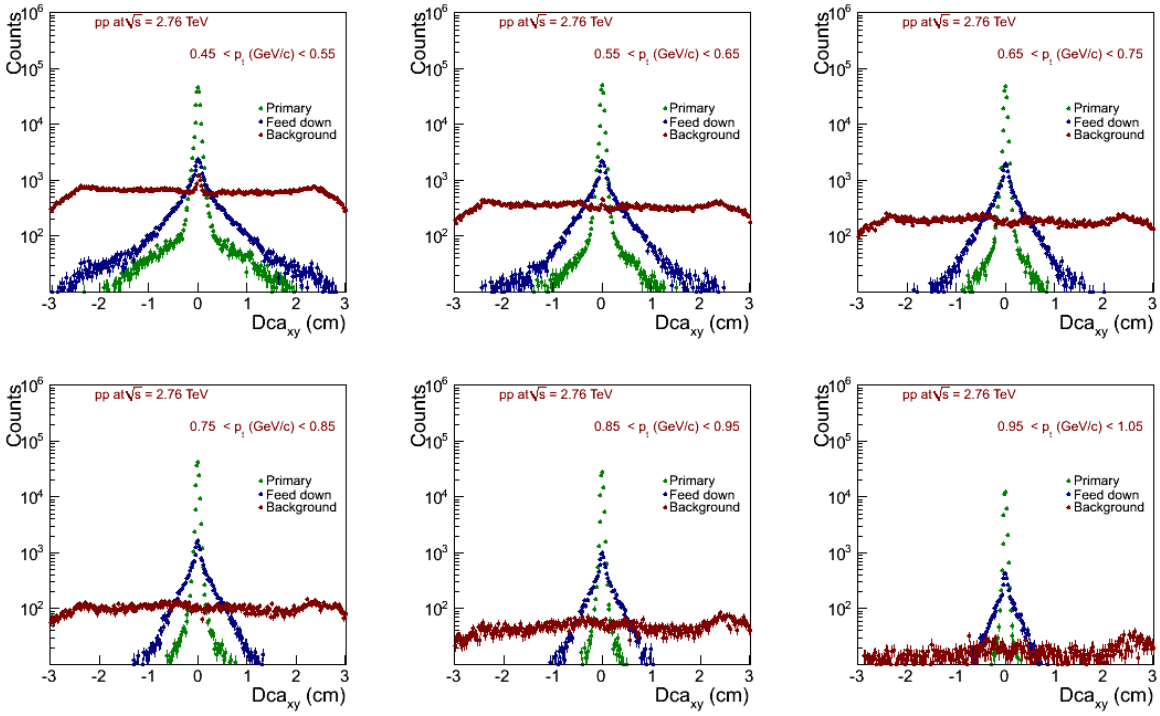

Figure 3.27: The dca distributions in transverse momentum bins of monte carlo PYTHIA protons. Protons are divided to primary(green) secodary originating from weak decay(blue) and secondary originating from interactions of other particles with detector material(red).

Corresponding plots for antiprotons are showing its background free nature:

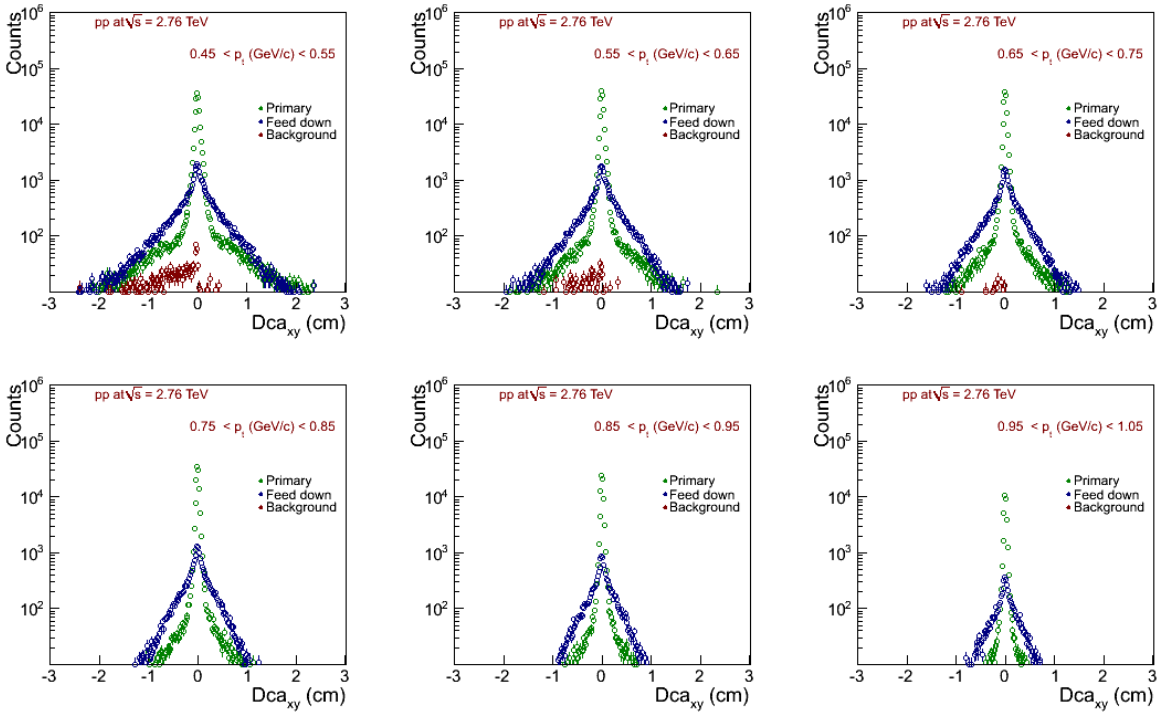

Figure 3.28: The dca distributions in transverse momentum bins of monte carlo PYTHIA antiprotons. Antiprotons are divided to primary(green) secodary originating from weak decay(blue) and secondary originating from interactions of other particles with detector material(red).

When we look at data *dca* distributions, we can see that distinct feature of proton distribution is long tail coming from background.

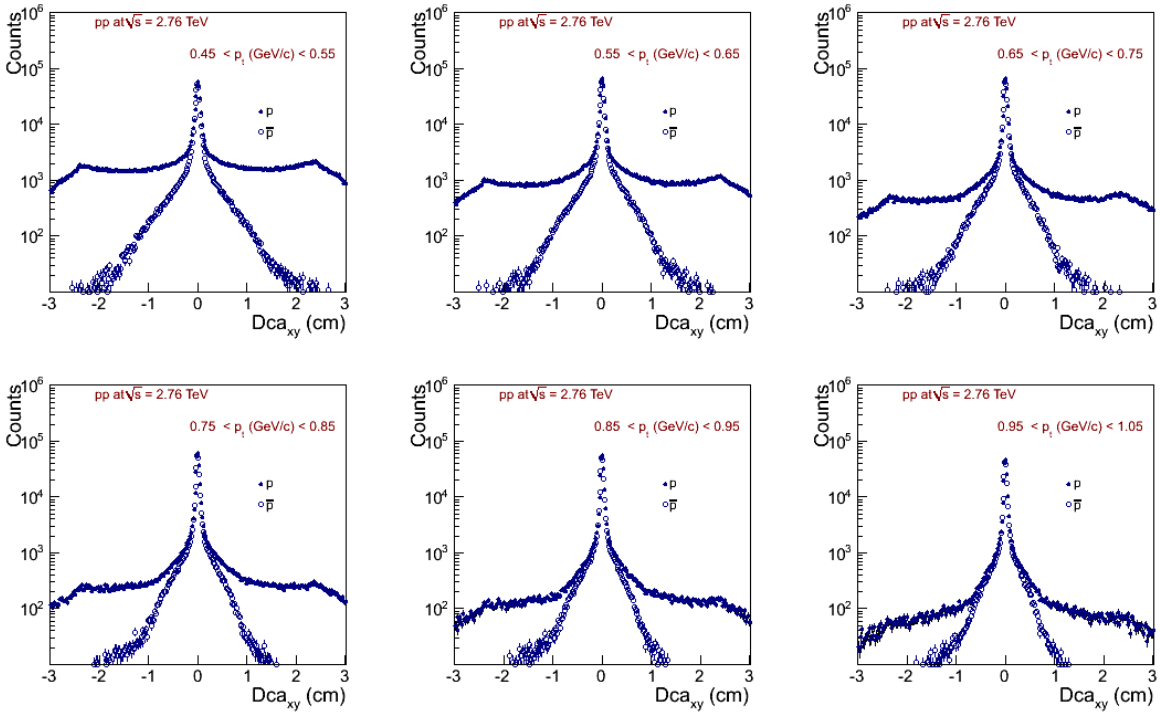

Figure 3.29: The dca distributions in transverse momentum bins of data protons (full points) and antiprotons(open points).

Interesting effect is visible on proton tails – the peaks at ≈ ±2.5 cm. These are from background and are described in Monte Carlo simulation too. Origin of these peaks we can reveal when we take a look on distribution of production vertex in x-y plane (see Figure 3.30)

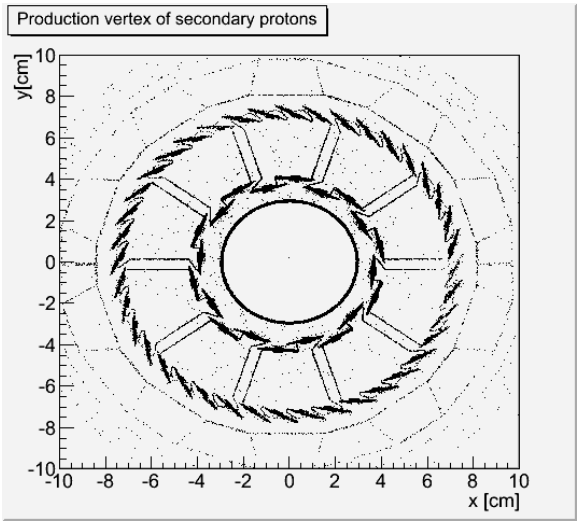

Figure 3.30: Production vertex of secondary protons with origin in interactions of other particles with material. Beam pipe and ALICE SPD is clearly visible.

Here we can see beam pipe and first layer of SPD – in their material budget most of the secondary protons are created.

The particles pushing out protons from material are:

- pions (211)
- Kaons – $K^{\pm}$(321) and K^{0}_{L}(130) ,fraction coming from K^{0}_{S}(310) is negligible
- protons(2212), neutrons(2112)

The pion group is the biggest one others are quite small in comparison,

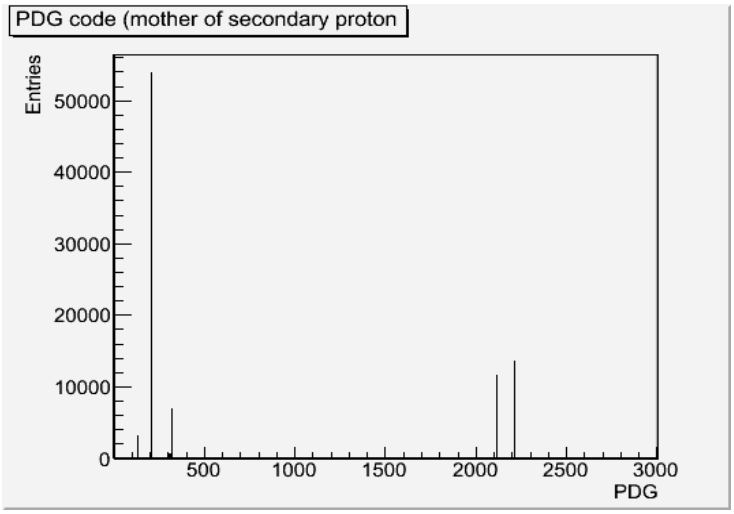

Figure 3.31: PDG code of mother of secondary monte carlo proton pushed from detector material.

Correction procedure

Correction procedure for this effect is based on fitting the data dca distribution of protons with sum of MC template histograms. This possibility is driven by fact that dca distribution of (anti)protons is properly described in Monte Carlo.

For this we are using framework included in ROOT as a class names TfractionFitter.

3.2.3.2 Λ

Secondary Λ produced in material can be distinguished from either primary or feed-down Λ in Cosine of pointing angle distribution (*cpa*). The feature of particles produced in

material is rather flat distribution in cosine of pointing angle and also in dca of Λ to primary vertex.

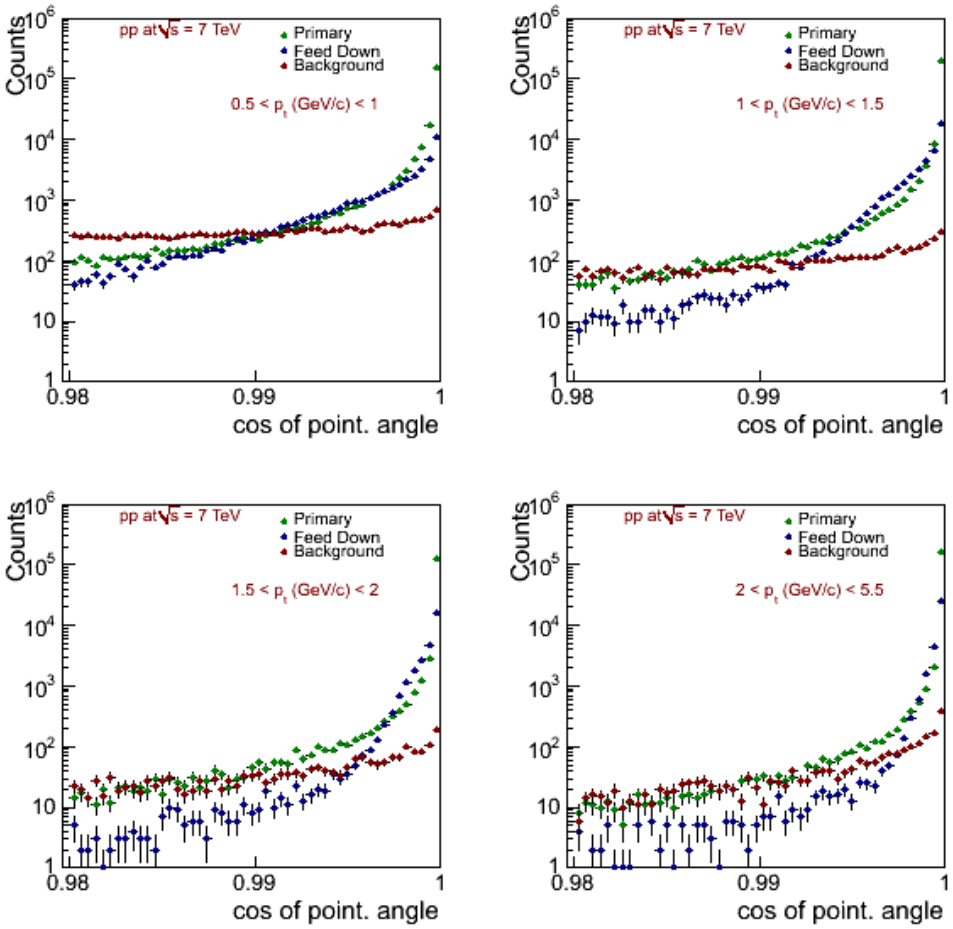

Figure 3.32: The cosine of pointing angle distributions in transverse momentum bins of Monte Carlo PYTHIA Λ. Λs are divided to primary(green) secodary originating from weak decay(blue) and secondary originating from interactions of other particles with detector material(red).

The effect is more pronounced at low p_t. You can see on the Figure 3.32, that background can be decreased by cut on cosine of pointing angle but a fraction will still remain in the sample since there are secondary particles with cosine of pointing angle close to unity.

The contamination by secondary particles coming from material results slowly decreasing *cpa* distribution for Λ then $\bar{\Lambda}$. This can be seen on Figure 3.33.

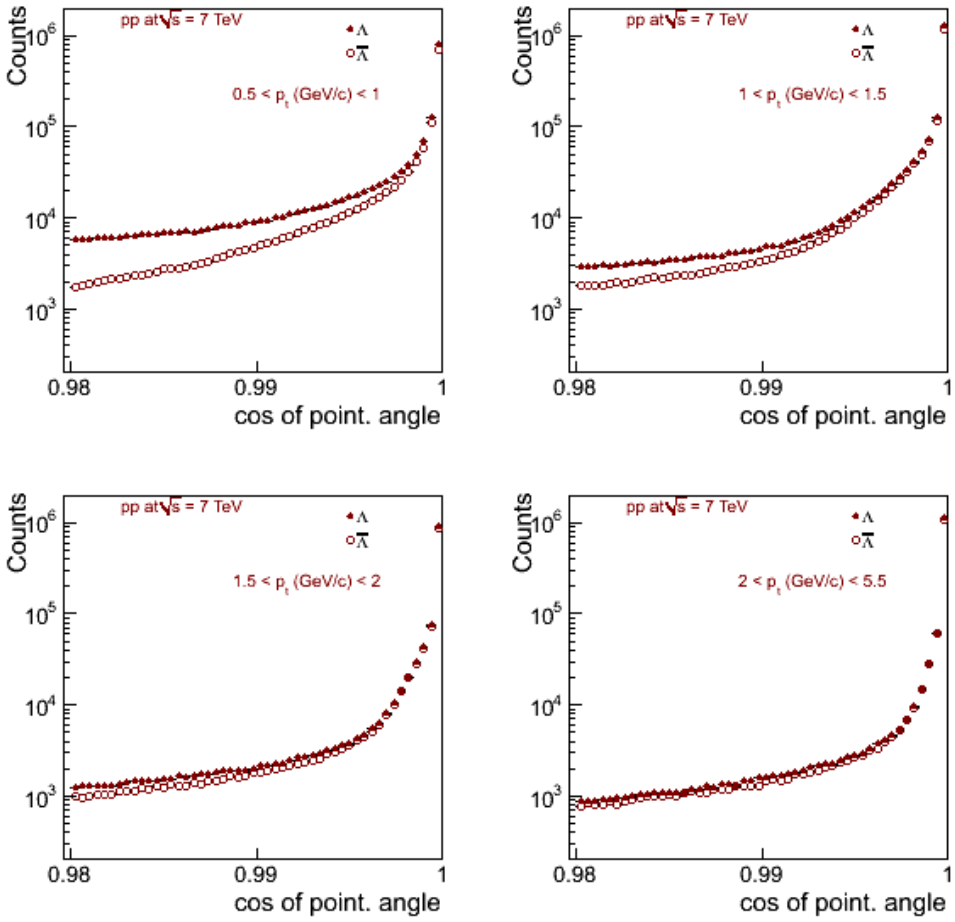

Figure 3.33: The cosine of pointing angle distributions in transverse momentum bins of data Λ (full points) and $\bar{\Lambda}$. (open points) candidates. Distributions corresponds to signal+background selected in invariant mass distribution in 10MeV/c^2 window around nominal mass of Λ.

Since $\bar{\Lambda}$ are background free and the cosine of pointing angle distribution comes together at $p_t \approx 2GeV/c$ we can conclude that the contamination vanishes at this value in transverse momentum.

It is interesting to see where this contamination comes from, what the particles are creating secondary Λ in material. All these particles need to be strange, since there is no strangeness in detector material. The fractions of secondary Λ coming from different sources – having different mothers can be seen on Figure. 3.34.

Material produced secondaries can be divided into the following groups:

- Primary background – Λ is made directly by its mother in interaction.

- Secondary background – Σ_0 is made in interaction; decays immediately to $\Lambda + \gamma$ with 100% branching ratio

The mother particles which are interacting with material are the following

- Kaons – $K^{\pm}$ and K^0_L ,fraction coming from K^0_S is negligible
- Charged Σ
- Λ – high energy Λ can create Σ_0 or another Λ

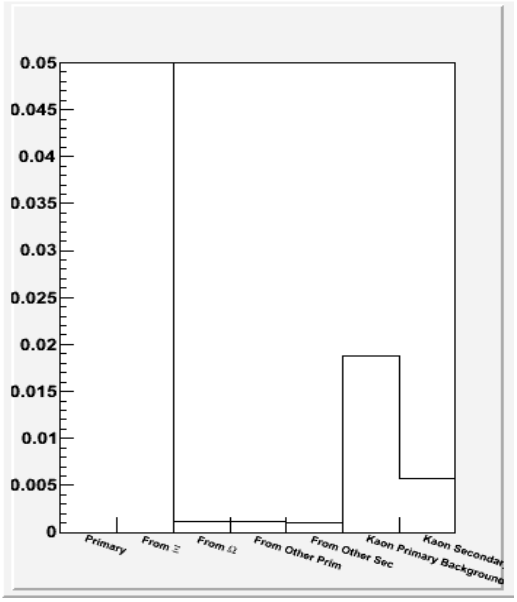

Figure 3.34: Primary and secondary fractions of Λ. Secondary are divided into groups corresponding to mother particle.

The fraction created by kaons (directly or indirectly) is most significant, other two parts are very small – comparable with Λ coming from Ω decays.

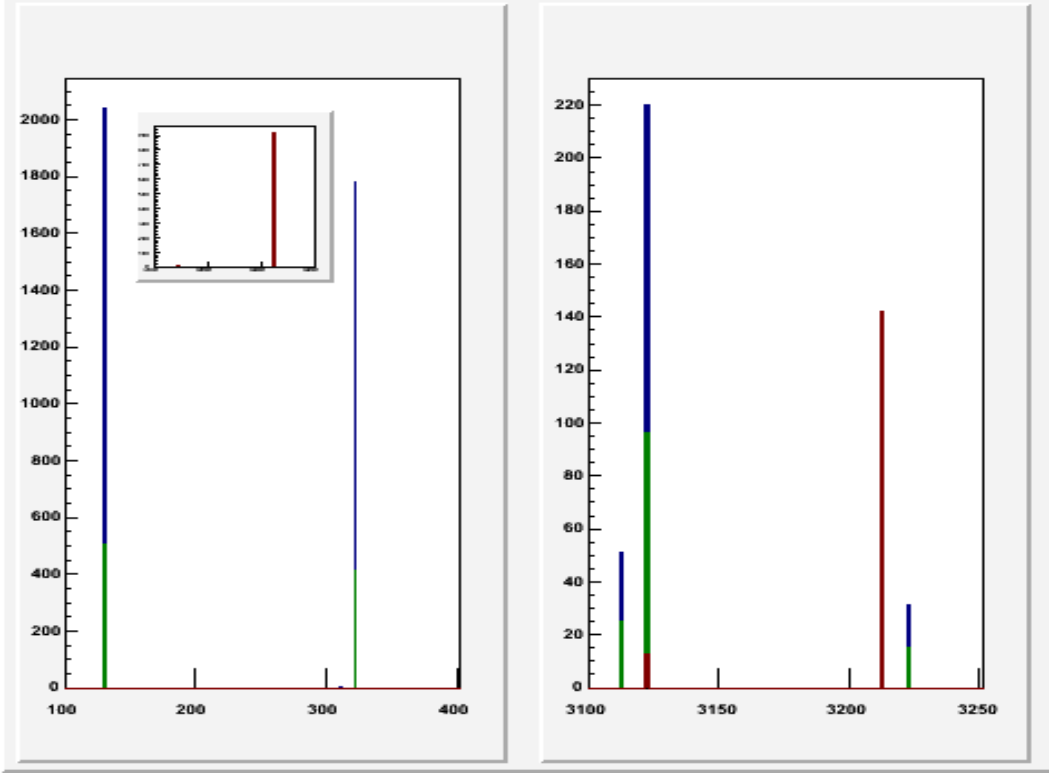

Figure 3.35: PDG code of mother of secondary monte carlo Λ with origin in interactions in detector material. Mothers are divided into primary(blue) secondary(green) and mothers of secondary(red).

Correction procedure

The correction procedure for this effect is similar that for protons, so it is based on fit of *cpa* distribution with template histograms, but there is a difference driven by fact that *cpa* distribution is not properly described in Monte Carlo. This is illustrated on Figure 3.36.

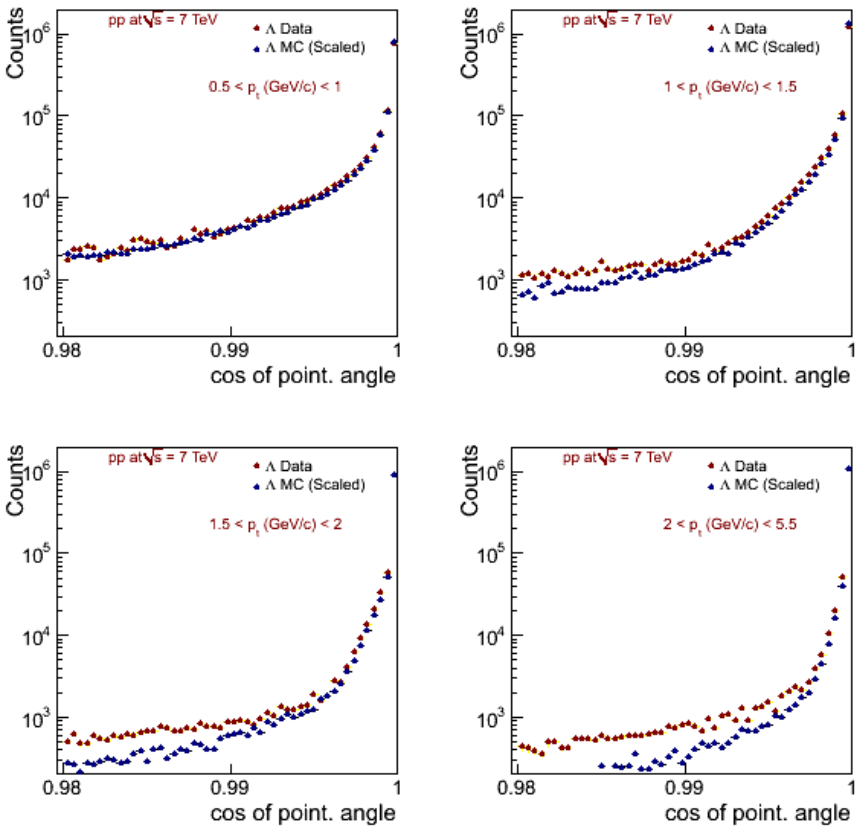

Figure 3.36: The cosine of pointing angle distributions in transverse momentum bins of data Λ (red) and monte carlo Λ (blue) candidates. Data distributions corresponds to signal extracted from invariant mass distribution. Monte carlo distribution is for „truth" Λ and was normalized to have the same integral as data distribution

The difference is increasing with transverse momentum. Even when we are using the same method to extract the *cpa* distribution of signal from data and Monte Carlo we can see the same behavior (see Figure 3.37).

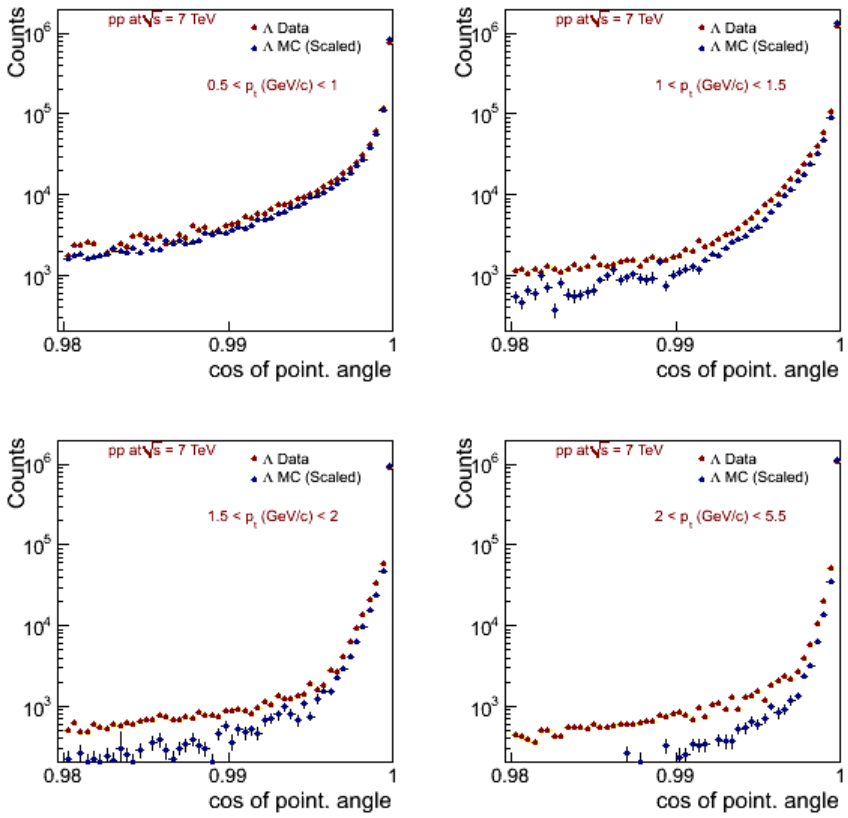

Figure 3.37: The cosine of pointing angle distributions in transverse momentum bins of data Λ (red) and monte carlo Λ (blue) candidates. Both distributions corresponds to signal extracted from invariant mass distribution. Monte carlo distribution was normalized to have the same integral as data distribution

Due to this fact, and because, as was shown before $\bar{\Lambda}$ are background free, we are using the $\bar{\Lambda}$ distribution as a primary-like template. For background we are using the Monte Carlo distribution, assuming that the shape of this effect is properly described.

Two methods were used for background evaluation and the difference between them was included into systematic uncertainty.

First method is using as input distributions for Λ and $\bar{\Lambda}$ the *cpa* distribution of pure signal. These can be extracted from three dimensional *cpa-p_t-invariant mass* histograms. You can see these distributions on Figure 3.38

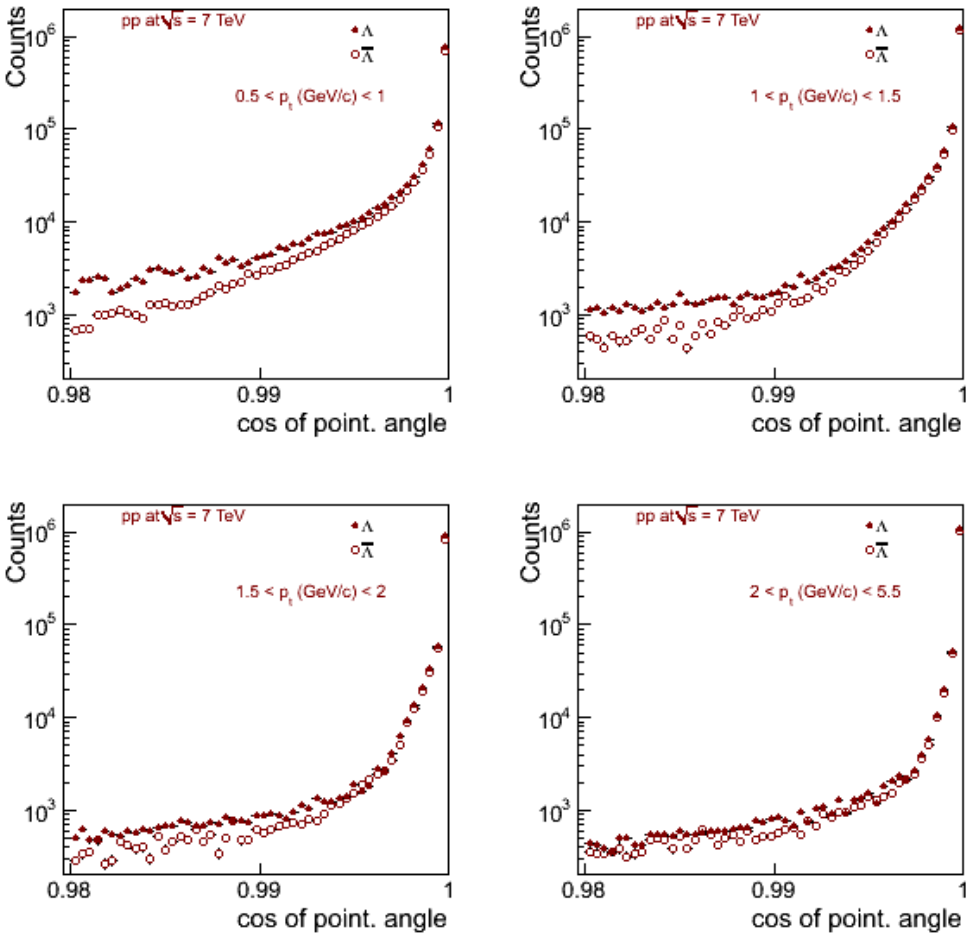

Figure 3.38: The cosine of pointing angle distributions in transverse momentum bins of data Λ (full points) and antiΛs (open points) candidates. Distributions corresponds to signal extracted from invariant mass distribution.

Clear difference can be seen in comparison with distribution of signal + background in mass window. The tails in higher *cpa* have faster decrease, but the overall p_t dependent difference between Λ and $\bar{\Lambda}$ due to secondaries produced in material is still there.

One can see on Figure 3.38 that with increasing *cpa* the points are starting to be seriously displaced. This is due to fast decreasing signal to background ratio in this regions.

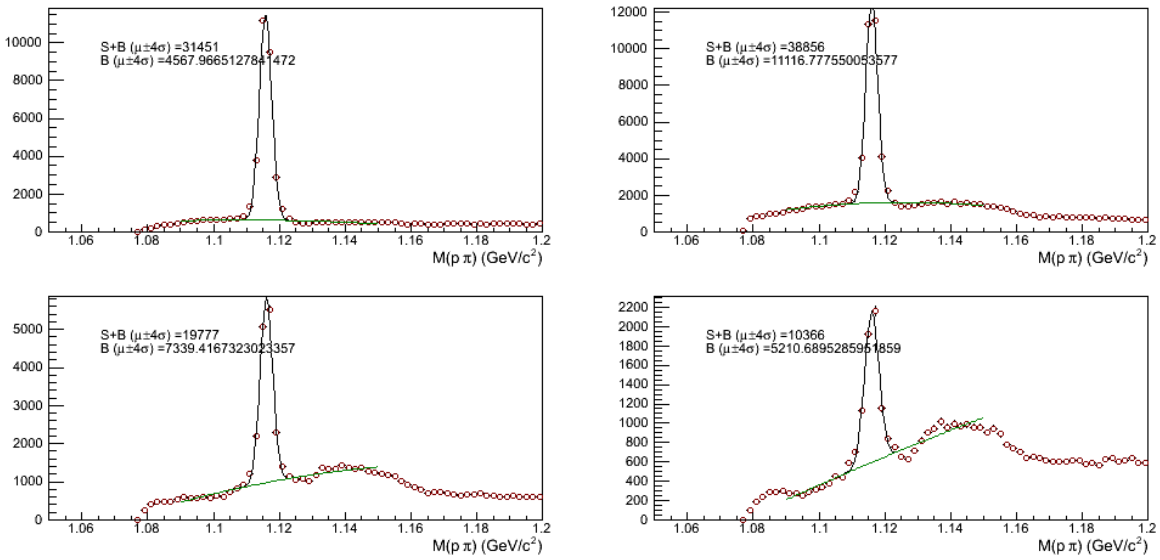

Figure 3.39: Invariant mass distribution with Λ hypothesis for different transverse momenta intervals and cosine of pointing angle ~0.997.

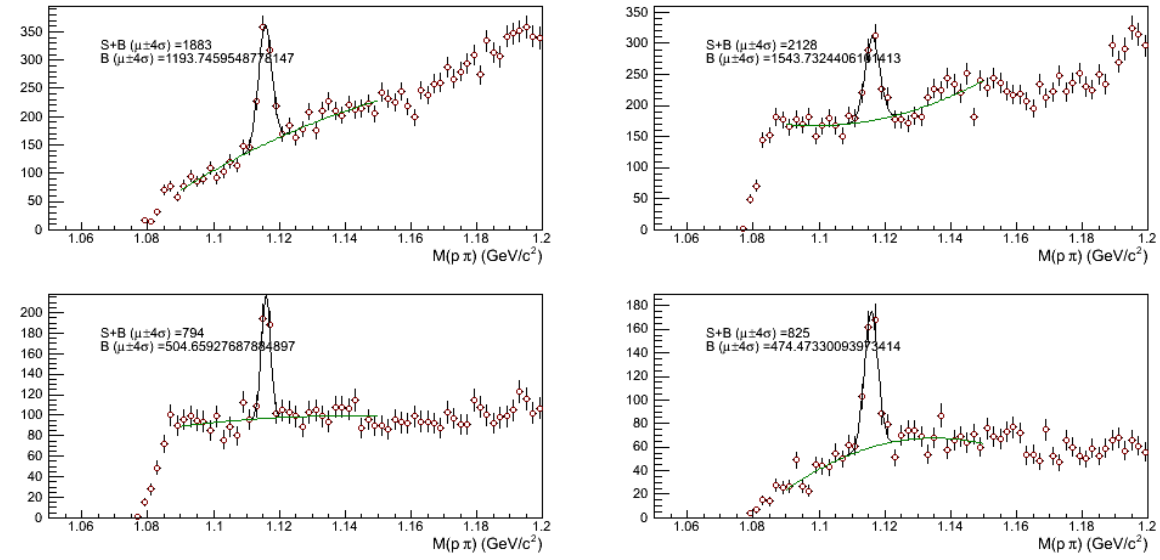

Figure 3.40: Invariant mass distribution with Λ hypothesis for different transverse momenta intervals and cosine of pointing angle ~0.98.

Due to these displacements the method is quite unstable and when we are changing the signal to background extraction procedure, we can see quite large differences. Because of this, another method was developed and is used as a default one.

Second method is using *cpa* distributions of signal + background in invariant mass window around nominal mass. The distributions are shown on Figure 3.41. As you can see on the Figure 3.8 the signal to background ratio is not the same for Λ and $\bar{\Lambda}$, so when using

these distributions we have to correct the correction factors for this effect. Since the combinatorial background has similar flat shape in *cpa* as we seen for material produced secondaries, there is possible to use

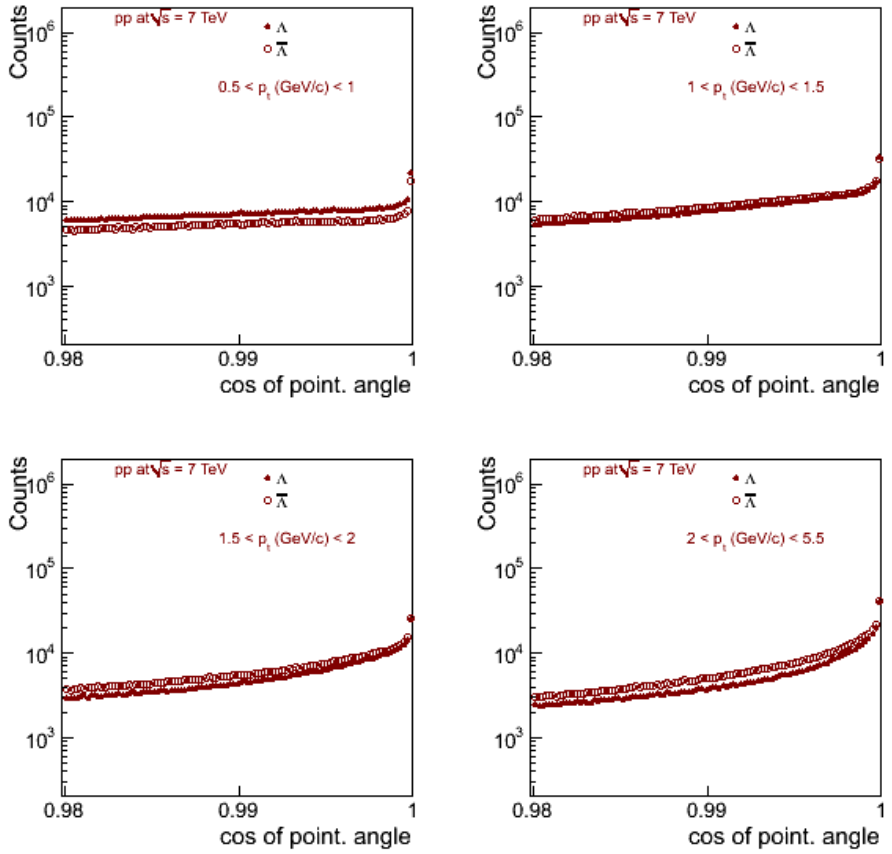

Figure 3.41: The cosine of pointing angle distributions in transverse momentum bins of data Λ (full points) and $\bar{\Lambda}$ (open points) candidates. Distributions corresponds to pure background selected in invariant mass distribution more then 10MeV/c^2 away from nominal mass of Λ.

Final fraction of secondary Λ as a function of transverse momentum you can see on Figure 3.42.

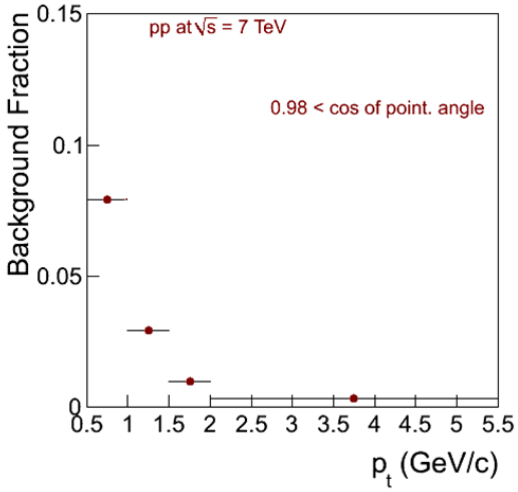

Figure 3.42: Fraction of secondary Λ in data sample in proton-proton collisions at √s = 7TeV selected with cosine of pointing angle larger then 0.98 with origin in interaction of other particles with detector material.

3.2.4 Feed Down correction

We are correcting our ratios in case of protons and Λ for secondary particles coming from the following week decays

$$\begin{aligned} \Lambda &\rightarrow p + \pi^- \\ \bar{\Lambda} &\rightarrow \bar{p} + \pi^+ \\ \Xi^- &\rightarrow \Lambda + \pi^- \\ \overline{\Xi^+} &\rightarrow \bar{\Lambda} + \pi^+ \end{aligned} \qquad (3.9)$$

We considered the fractions of (anti)protons in the sample coming from Ξ and Ω negligible and cancelling out in the ratio. Λ coming from prompt decay of neutral Σ are considered as physical primary.

Because primary and secondary Λ have similar spectra shape, we can use integrated correction for feed down contamination from Ξ decays. This was tested directly using Monte Carlo simulation. Using Monte Carlo, the ratio $r_{feed-down}$ of the reconstructed Ξ candidates to the number of reconstructed Λ candidates from Ξ decays is

$$r_{feed-down} = \frac{(N_{\Xi})_{MC}}{(N_{\Lambda \leftarrow \Xi})_{MC}}. \qquad (3.10)$$

Assuming that this ratio is the same in both Monte Carlo and data, the whole feed down contribution to the spectra is estimated by dividing the number of reconstructed Ξ in data by the ratio extracted from Monte Carlo

$$(N_{\Lambda \leftarrow \Xi})_{Data} = \frac{(N_{\Xi})_{Data}}{r_{feed-down}}. \qquad (3.11)$$

Correction for secondary (anti)protons coming from Λ decays is done using dca distributions in the same way as it is done for secondary protons produced in material.

3.2.5 Cut efficiency

The effect of the differences in the efficiencies of the analysis cuts for the proton and antiprotons was taken also into account. The reason for this observed charge asymmetry is that particles undergoing elastic scattering in the inner detectors can still be reconstructed in the TPC but the corresponding ITS hits will in general not be associated to the track if the scattering angle is large. The physical mechanism responsible is the corresponding differences in the elastic cross-sections for proton and antiproton. Figure 3.43, shows the momentum dependence of the (anti)proton – Nucleus elastic cross-section for GEANT3. The full points (when available) are the cross-section values measured experimentally.

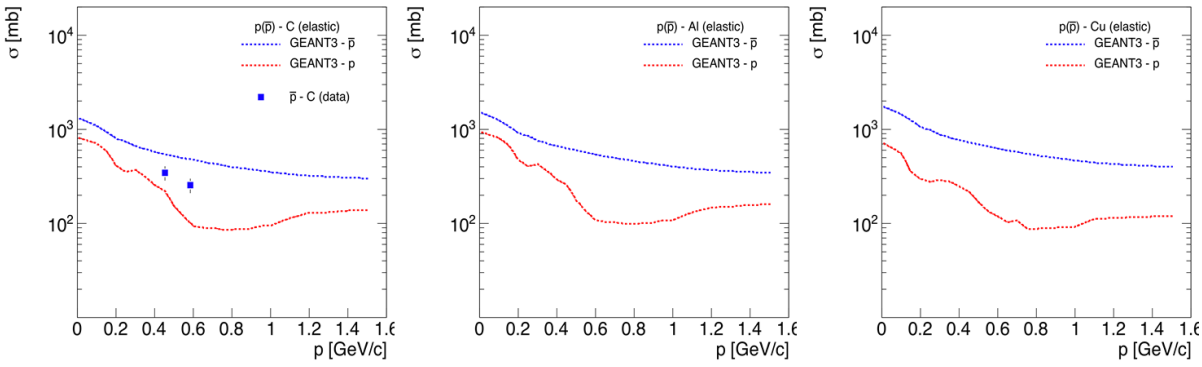

Figure 3.43:[39] The momentum dependence of the (anti)proton – Nucleus elastic cross-section for C(left), Al(middle) and Cu(right). The curves represent the parameterization used in GEANT3 for protons (red) or antiprotons (blue). The full points are the cross-section values measured experimentally.

As in the case of the inelastic cross-section, the parameterization used in GEANT3 is in agreement with the proton–Nucleus experimentally measured values, whereas it disagrees with the antiproton–Nucleus ones. Concerning elastic scattering, where only a limited data set is available for comparison, GEANT3 cross sections are about 25% above FLUKA, the latter being again closer to the measurements. We therefore used the FLUKA results to account for the difference of proton and antiproton cross sections. The resulting correction was estimated to be ~ 3.5%.

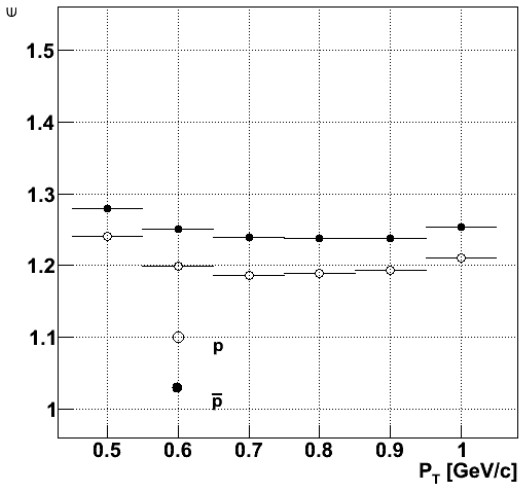

Figure 3.44: Correction factors for cut efficiency as function of transverse momentum for protons(open point) and antiprotons(full points).

Final correction factors as a function of transverse momentum for protons and antiprotons you can see on Figure 3.44.

4 Results

4.1 Data sample

The data used for this analysis were collected during the 2010 LHC pp run at collision energy √s = 900 GeV and 7 TeV and in March 2011 at collision energy √s = 2.76 TeV.

900 GeV	2.76 TeV	7 TeV
7M	40M	180M

Table 4.1: Number of analyzed proton-proton events per collision energy

The first step of the analysis is to select a suitable event sample. For the analysis, events were selected based on the online trigger [32]. In addition, at least one of the following criteria was requested to be fulfilled as an offline trigger:

- two fired chips in the SPD
- one fired chip in the SPD and a beam-beam flag in either V0A or V0C
- beam-beam flags on both V0A and V0C.

Furthermore, in order for the events to be included in the analysis, they should not be flagged as beam-gas by either V0A or V0C.

Events passing both triggers were then selected only if the primary vertex was reconstructed and if the position of the reconstructed vertex diamond was within the selected area.

Total numbers of analyzed events passing these selections are summarized in Table 4.1.

4.2 Analysis details

Several quality criteria are defined for the track selection. Each track is required to have been reconstructed in the TPC in the initial outward-in step of tracking and then

successfully refitted in the final back-propagation to the primary vertex . It is also required that each track has at least 80 TPC clusters out of a maximum of 159.

Number of TPC clusters	80
Number of TPC clusters (dE/dx)	80
TPC refit	Yes

Table 4.2: Track quality cuts used for proton tracks or daugter tracks in case of Λ, Ξ and Ω

In antiproton-to-proton analysis to reduce the contamination from background tracks (i.e. originating from the interaction of a particle with the material), the selected tracks were required to have at least two associated ITS clusters. Furthermore, a track must have at least one associated ITS cluster on either of the SPD layers. To further reduce the contamination from background and secondary tracks (i.e. (anti)protons originating from the weak decay of Λ), a cut on the distance of closest approach in xy plane (dca_{xy}) of the track to the primary vertex was set.

dca_{xy}	< 0.2 cm
Number of ITS clusters	2
Hit on SPD1 || SPD2	Yes

Table 4.3: Track quality cuts used to decrease a fraction of non-primary tracks in the proton sample

The Λ, Ξ and Ω are identified by applying selections on the characteristics of their daughter tracks (see Table 4.4 and Table 4.5) and using their weak decay topologies in the channels listed in Table 3.1.

Λ	**900GeV**	**7TeV**
Cosine of pointing angle	> 0.9	> 0.98
DCA Positive to prim. vertex (cm)	> 0.05	
DCA Negative to prim. vertex (cm)	> 0.05	
DCA between daughters (cm)	< 0.5	< 1.5
Decay radius (cm)	> 0.2	

Table 4.4: V^0 topological selections used in reconstruction of secondary vertices for Λ analysis

	900 GeV	7 TeV	
	Ξ	**Ξ**	**Ω**
DCA Bachelor to prim. vertex(cm)	> 0.01	> 0.03	
DCA Positive to prim. vertex (cm)	> 0.01	> 0.02	
DCA Negative to prim. vertex (cm)	> 0.01	> 0.02	
DCA V^0 to prim. vertex (cm)	> 0.001	> 0.05	
Cascade decay radius (cm)	> 0.2	> 0.04	
V^0 decay radius (cm)	> 0.2	> 1.0	
Cosine of pointing angle(V^0 in casc.)	> 0.97	> 0.97	
DCA btw. V^0 daughters in cascade (cm)	< 3.0	< 2.0	< 0.4
DCA btw. cascade daughters (cm)	< 3.0	< 2.0	< 0.5
Cosine of pointing angle(cascade)	> 0.85	> 0.97	> 0.98

Table 4.5: Cascade topological selections used in reconstruction of secondary vertices for Ξ and Ω analysis

The momentum as well as the particle identification (PID) relied for this analysis on the information from the TPC detector. The *dE/dx* resolution of the TPC is 5% and depends slightly on number of TPC clusters and inclination angle. To ensure the best identification efficiency and the lowest possible contamination, the minimum number of TPC clusters used for the energy loss calculation was set to 80.

The (anti)protons were selected by defining a band with a 3σ width with respect to teoretical Bethe-Bloch parametrization.

For Λ, Ξ and Ω the particle identification of daughter tracks helps substantialy to decrease the background, especialy in the low p_t – high $|y|$ areas. The selection here concerns all daughters.

Additional cuts are used in case of Λ and Ω. We are excluding the candidates falling into 10 MeV mass window around K^0_s or Ξ nominal mass.h

4.3 Systematic uncertainity

Sources of systematic uncertainities are driven mainly by used corrections but small part is comming also from analysis procedure. The following sources of systematic uncertainity were taken into acount:

- Uncertainity of amounth of the material in central part of detector - driven by absorption efects
- Uncertainity of experimental value of inelastic and elastic (only protons) cross section addapted in the transport code GEANT3 or FLUKA - driven by absorption efects
- Uncertainities of correction procedures itself
- Effects of the reasonable variation of the selections and cuts
- Uncertainity of the extracted signal - driven by the description of the background shape

The amount of material in the central part of ALICE is very low, corresponding to about 10% of a radiation length on average between the vertex and the active volume of the TPC. It has been studied with collision data and adjusted in the simulation based on the analysis of photon conversions. The current simulation reproduces the amount and spatial distribution of reconstructed conversion points in great detail, with a relative accuracy of a few percent. Based on these studies, we assign a systematic uncertainty of 7% to the material budget. By changing the material in the simulation by this amount, we find a variation of the final ratio of 0.5%.

The experimentally measured p–A reaction cross sections are determined with a typical accuracy better than 5% [38]. We assign a 10% uncertainty to the absorption correction as calculated with FLUKA, which leads to a 0.8% uncertainty in the ratio R.

By comparing GEANT3 with FLUKA and with the experimentally measured elastic cross-sections, the corresponding uncertainty was estimated to be 0.8%, which corresponds to the difference between the correction factors calculated with the two models.

Was verified that variation of cuts and selections within reasonable ranges have small effect on the measured ratio. Namely the topological selection used in reconstruction

of V^0 and cascade vertices, sharpness of particle identification and ranges of additional cuts were taken into account.

Three methods for signal/background evaluation were used in paralel. Difference between these methods is comming from different aproximations of the background shape. The estimated difference is around 0.4% and incereses when statistic is low.

Uncertainity comming from the correction procedures, namely correction for absorption, cross section and secondaries produced in the material was found to be very small.

The influence of beam-gas and beam-halo background events was estimated to be negligible based on simulation studies. The studies in real conditions during the period of data taking confirmed our estimates. To further investigate the potential effect of these events to our measurement, the whole analysis chain was applied to the overall data sample without imposing any requirement on either the online or the offline trigger. The resulting values of the ratio were in agreement with the ones reported in this note up to the fourth digit. The systematic uncertainty from this contribution is < 0.1%.

Systematic uncertainties from different sources are added in quadrature and leads into total uncertainty of about 1.5%. Uncertainties in percents from different sources and for samples at various collision energies are summarized in the Table 4.6 for protons and in Table 4.7 for strange baryons.

Source		**p**
Material budget		0.5 %
Inelastic cross section		0.8 %
Elastic cross section		0.8 %
Selections		0.4 %
Corrections	Cross section	< 0.1 %
	Absorption	< 0.1 %
	Background	0.6 %
	Cut efficiency	< 0.1 %
	Feed down	0.6 %
TOTAL		**1.4 %**

Table 4.6 : Systematic uncertainty of the $\bar{p}/p$ ratio

Source		Λ (%)	Ξ (%)	Ω (%)
Material budget			0.5	
Inelastic cross section			0.8	
Selections		0.3 - 0.1 - 0.2	4.2 - 0.9 - 0.7	3.8 – 1.7
Corrections	Cross section		< 0.1	
	Absorption		< 0.1	
	Background	0.2	-	
Signal/Background extraction		0.3 - 0.5 – 0.3	0.9 - 0.4 – 0.2	1.7 – 0.4
TOTAL		**1.3 - 1.2 – 1.1**	**4.4 - 1.4 – 1.2**	**4.3 – 2.0**

Table 4.7: Systematic uncertainty of the $\bar{\Lambda}/\Lambda$, $\overline{\Xi^+}/\Xi^-$ and $\overline{\Omega^+}/\Omega^-$ ratio.

4.4 Rapidity and transverse momentum dependence

4.4.1 $\bar{p}/p$

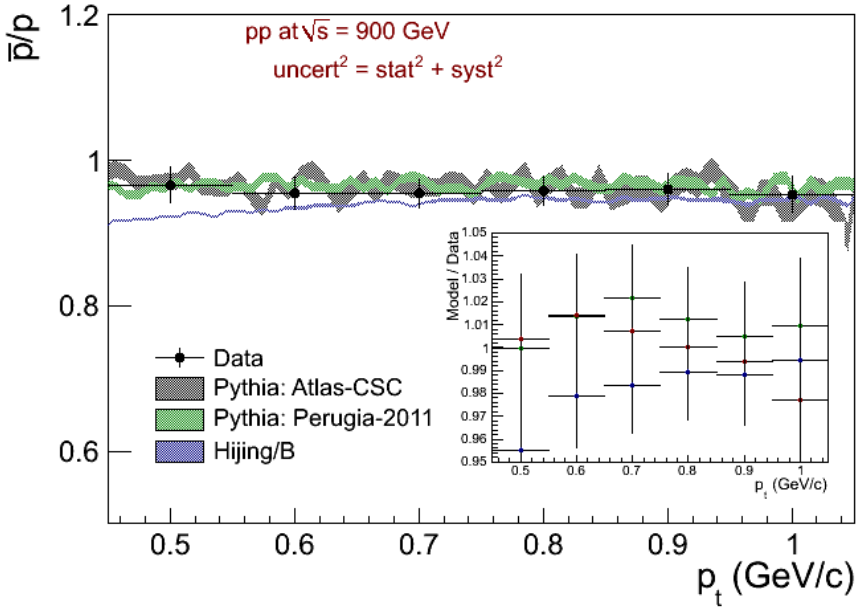

Figure 4.1: $\bar{p}/p$ ratio as function of transverse momentum at $\sqrt{s}$ = 900 GeV. Data points are compared with different monte carlo predictions. Inset is showing model over data ratios.

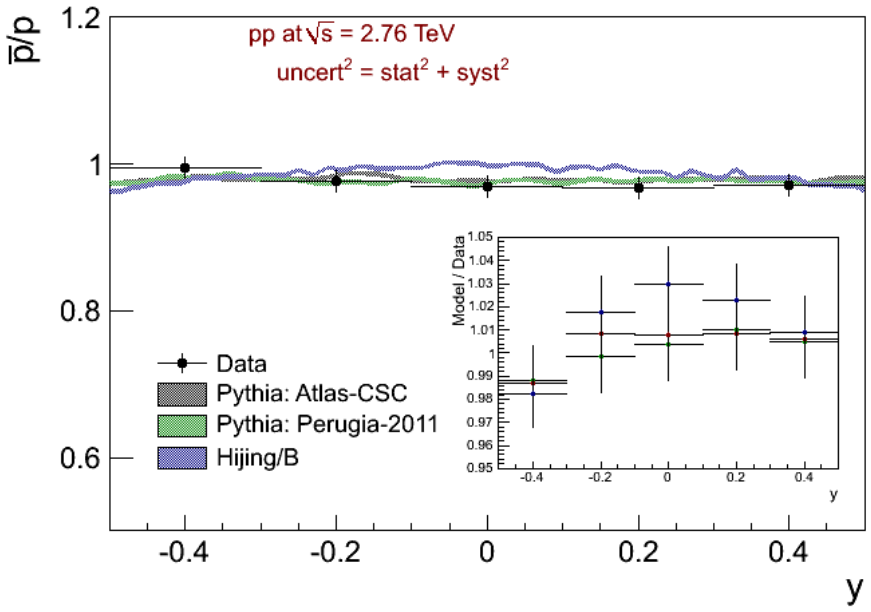

Figure 4.2: $\bar{p}/p$ ratio as function of rapidity at $\sqrt{s}$ = 2.76 TeV. Data points are compared with different monte carlo predictions. Inset is showing model over data ratios.

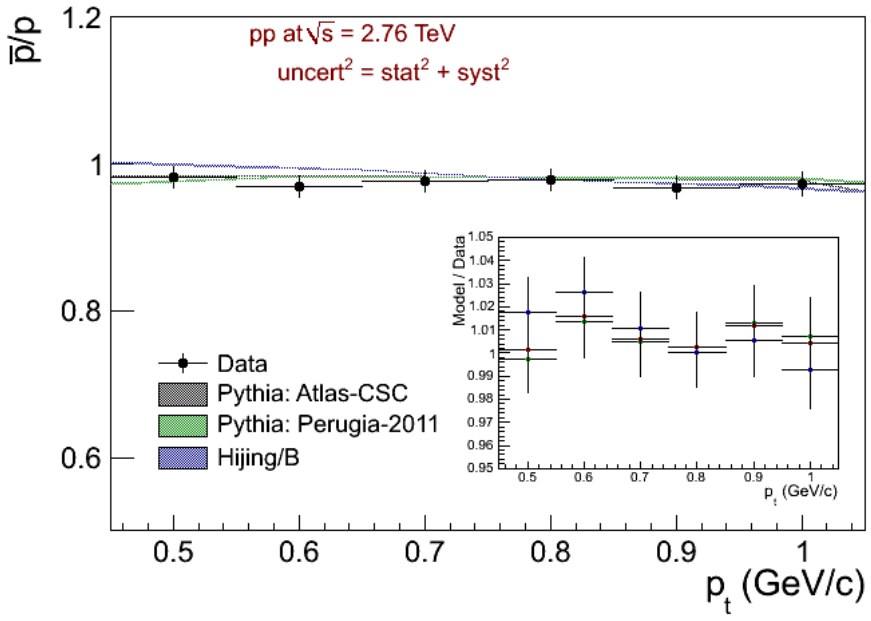

Figure 4.3: $\bar{p}/p$ ratio as function of transverse momentum at $\sqrt{s}$ = 2.76 TeV. Data points are compared with different monte carlo predictions. Inset is showing model over data ratios.

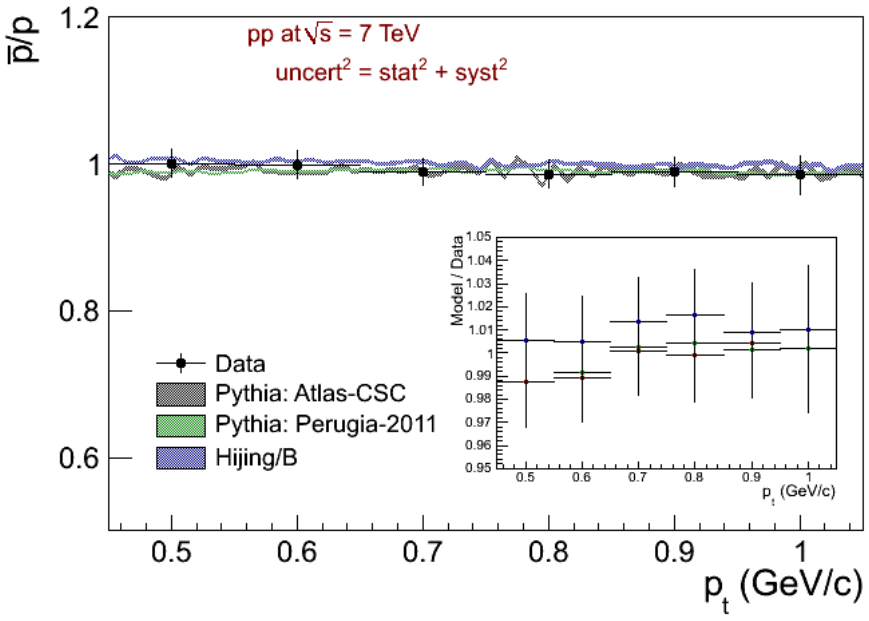

Figure 4.4: $\bar{p}/p$ ratio as function of transverse momentum at $\sqrt{s}$ = 7 TeV. Data points are compared with different monte carlo predictions. Inset is showing model over data ratios.

For $\bar{p}/p$ ratio we dont see any sign of rapidity or transverse momentum depenedence. Data points are well described by PYTHA tunes: Atlas-CSC and Perugia-2011 and by HIJING/B.

4.4.2 $\bar{\Lambda}/\Lambda$

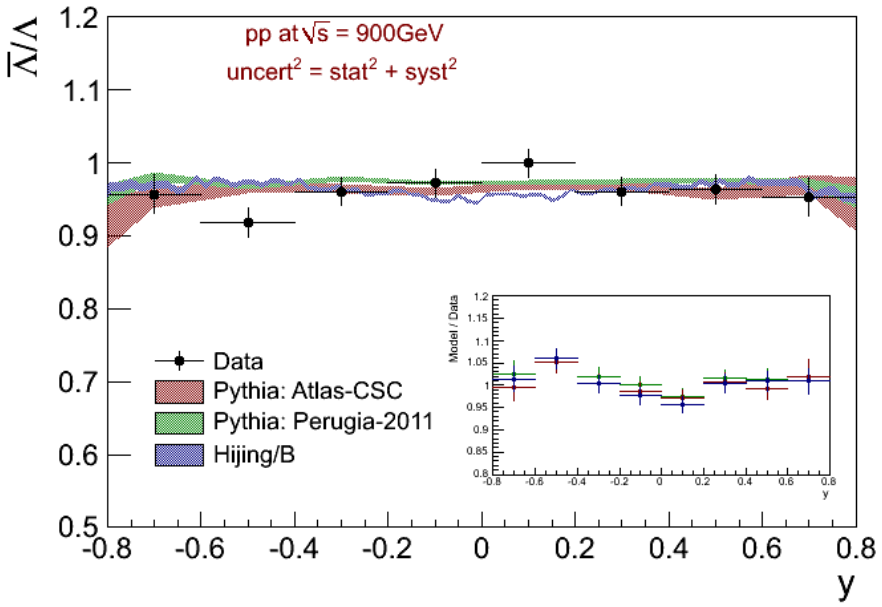

Figure 4.5: $\bar{\Lambda}/\Lambda$ ratio as function of rapidity at $\sqrt{s}$ = 900 GeV. Data points are compared with different monte carlo predictions. Inset is showing model over data ratios.

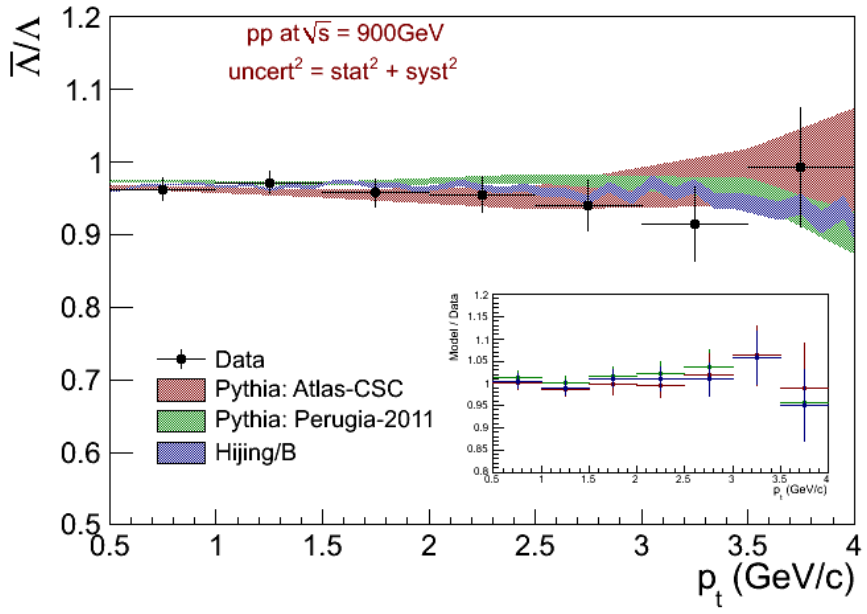

Figure 4.6: $\bar{\Lambda}/\Lambda$ ratio as function of transverse momentum at $\sqrt{s}$ = 900 GeV. Data points are compared with different monte carlo predictions. Inset is showing model over data ratios.

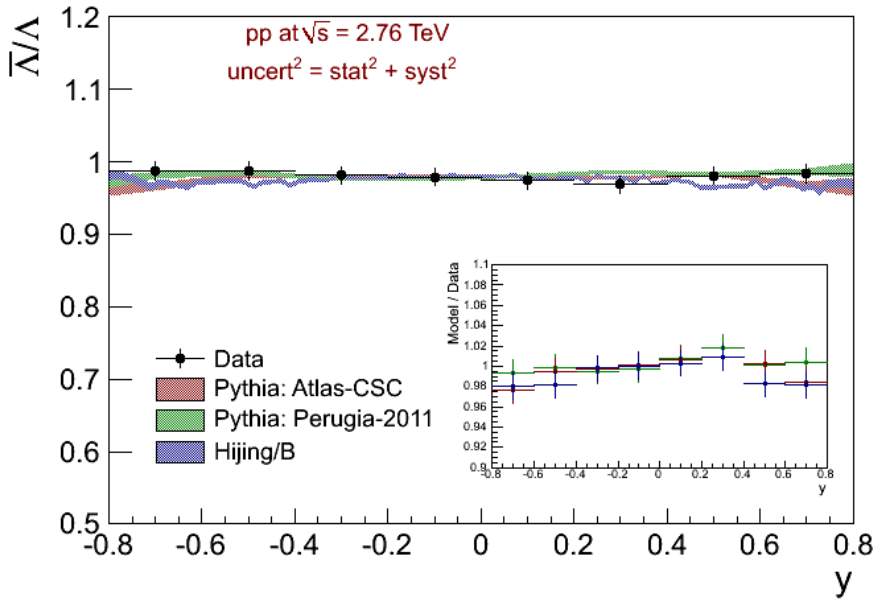

Figure 4.7: $\bar{\Lambda}/\Lambda$ ratio as function of rapidity at $\sqrt{s}$ = 2.76 TeV. Data points are compared with different monte carlo predictions. Inset is showing model over data ratios.

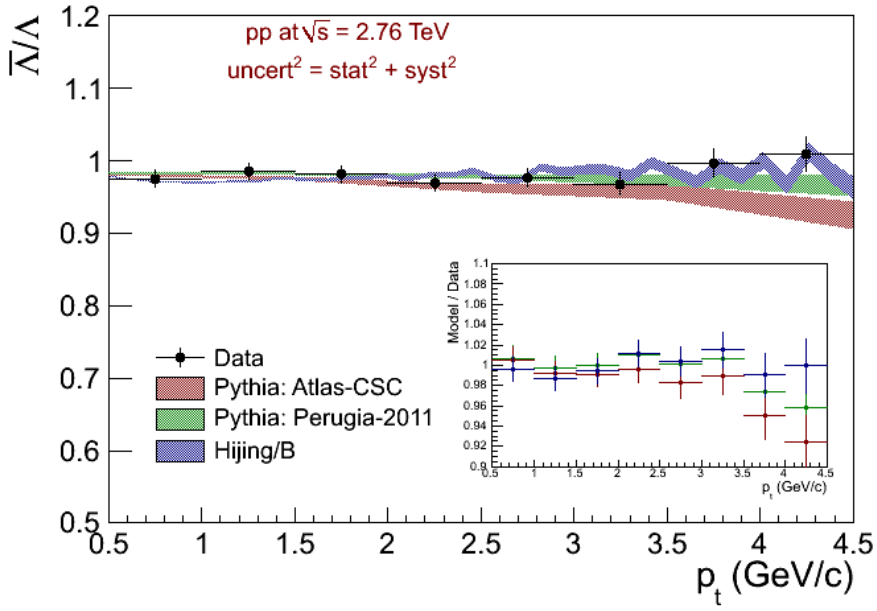

Figure 4.8: $\bar{\Lambda}/\Lambda$ ratio as function of transverse momentum at $\sqrt{s}$ = 2.76 TeV. Data points are compared with different monte carlo predictions. Inset is showing model over data ratios.

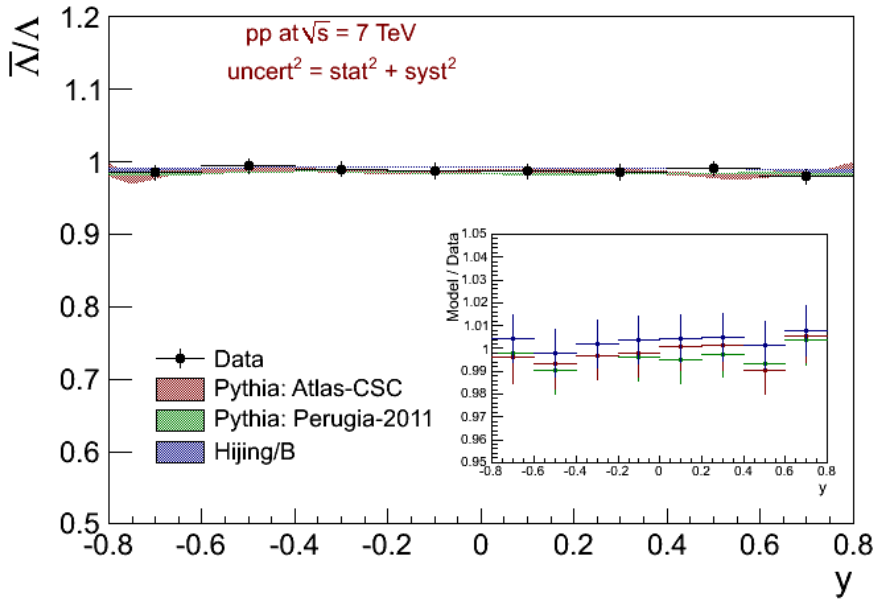

Figure 4.9: $\bar{\Lambda}/\Lambda$ ratio as function of rapidity at $\sqrt{s}$ = 7 TeV. Data points are compared with different monte carlo predictions. Inset is showing model over data ratios.

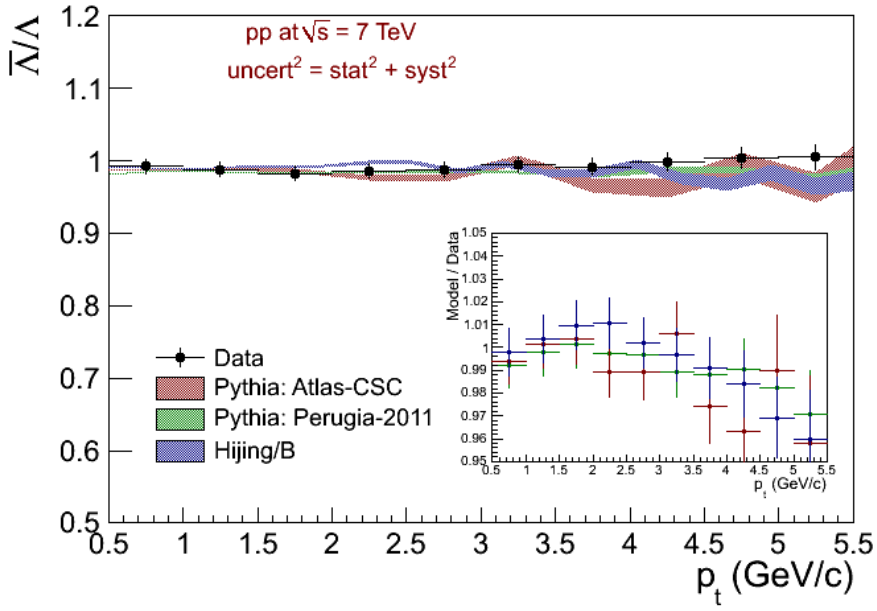

Figure 4.10: $\bar{\Lambda}/\Lambda$ ratio as function of transverse momentum in the area 0.5< p_t (GeV/c) <5.5 at $\sqrt{s}$ = 7 TeV. Data points are compared with different monte carlo predictions. Inset is showing model over data ratios.

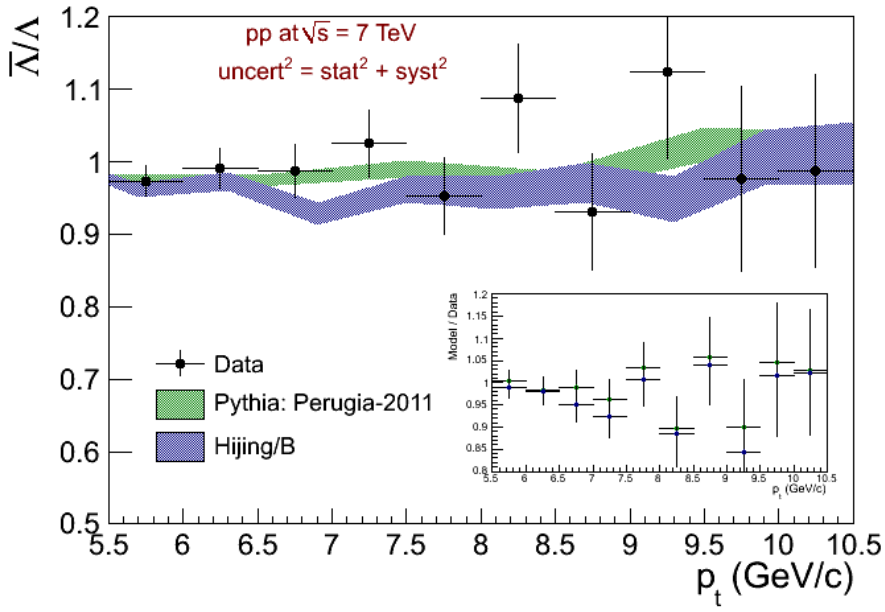

Figure 4.11: $\bar{\Lambda}/\Lambda$ ratio as function of transverse momentum in the area 5.5< p_t (GeV/c) <10.5 at √s = 7 TeV. Data points are compared with different monte carlo predictions. Inset is showing model over data ratios.

For $\bar{\Lambda}/\Lambda$ ratio we dont see any sign of rapidity or transverse momentum depenedence. Data points are well described by PYTHA tunes: Atlas-CSC and Perugia-2011 and by HIJING/B.

At √s = 7TeV two phase space regions were analyzed separatelly. The first one in low p_t up to 5.5 GeV/c was analyzed in two dimensions using all corrections described in section 3.2. The second one in p_t higher then 5.5 GeV/c was analyzed in transverse momentum only and on top of that, no correction were applied. This was induced by fact that all the corrected effect vanish, and are negligible in this region. Mid rapidity ratios in both regions are compatible (see Table 4.8)

$0.5 < p_t$ (GeV/c) < 5.5	5.5 < p_t (GeV/c) < 10.5
0.989±0.001±0.010	0.986±0.013±0.008

Table 4.8: Mid-rapidity $\bar{\Lambda}/\Lambda$ ratio at √s = 7 TeV in different p_t areas. Values are printed with statistical and systematical uncertainity

4.4.3 $\overline{\Xi^+}/\Xi^-$

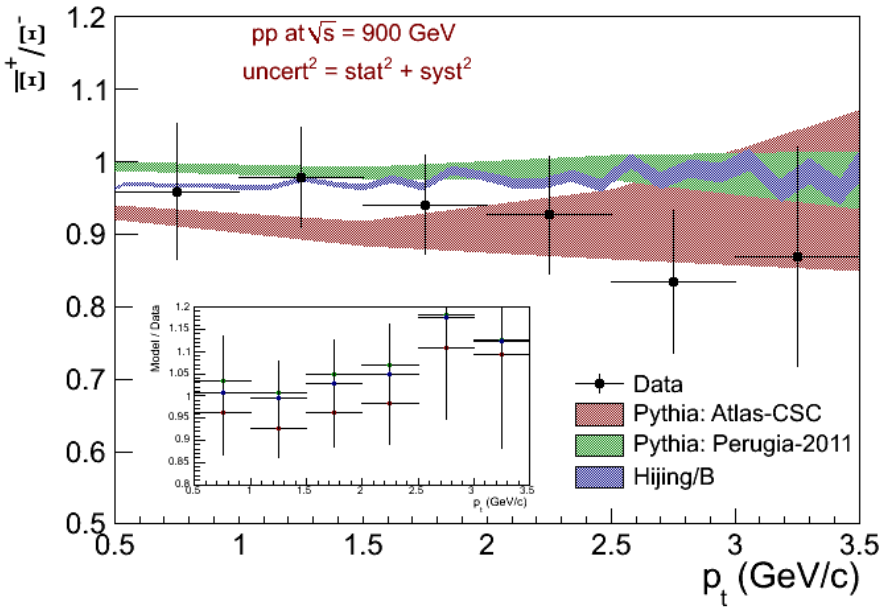

Figure 4.12: $\overline{\Xi^+}/\Xi^-$ ratio as function of transverse momentum at √s = 900 GeV. Data points are compared with different monte carlo predictions. Inset is showing model over data ratios.

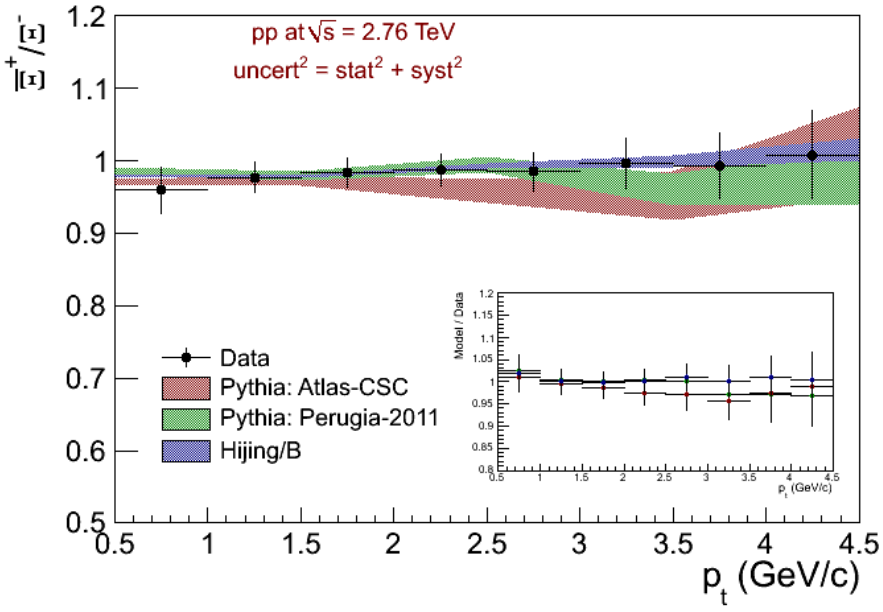

Figure 4.13: $\overline{\Xi^+}/\Xi^-$ ratio as function of transverse momentum at √s = 2.76 TeV. Data points are compared with different monte carlo predictions. Inset is showing model over data ratios.

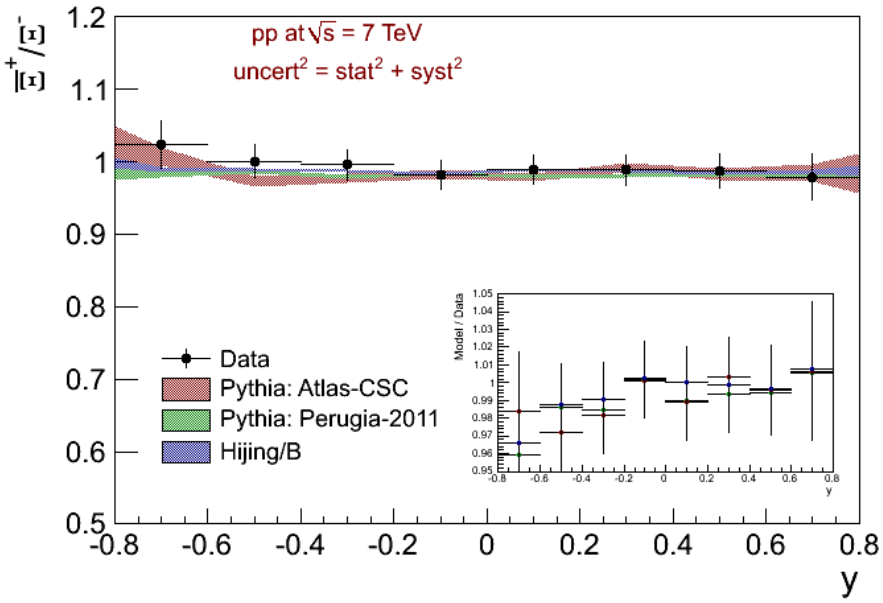

Figure 4.14: $\overline{\Xi^+}/\Xi^-$ ratio as function of rapidity at √s = 7 TeV. Data points are compared with different monte carlo predictions. Inset is showing model over data ratios.

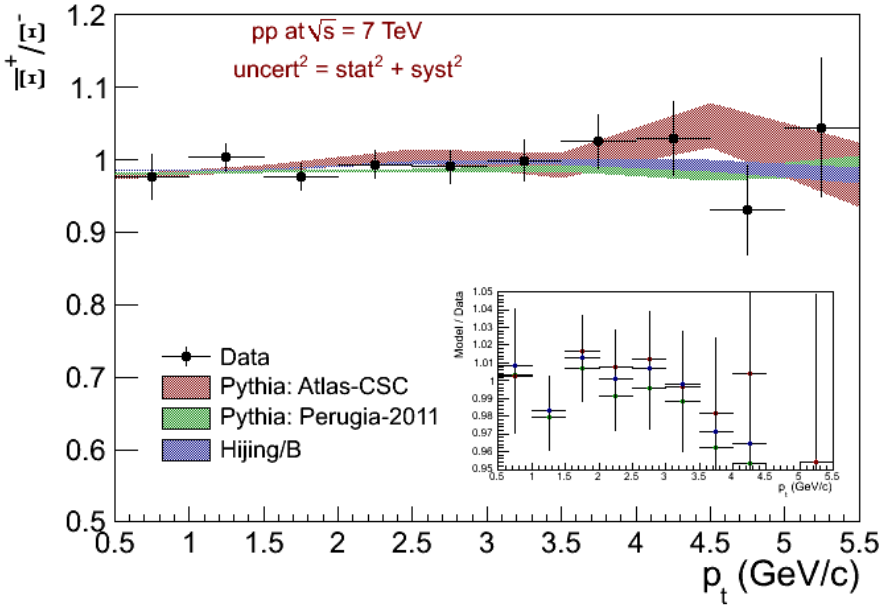

Figure 4.15: $\overline{\Xi^+}/\Xi^-$ ratio as function of transverse momentum at √s = 7 TeV. Data points are compared with different monte carlo predictions. Inset is showing model over data ratios.

For $\overline{\Xi^+}/\Xi^-$ ratio we dont see any sign of rapidity or transverse momentum depenedence. Data points are well described by PYTHA tunes: Atlas-CSC and Perugia-2011 and by HIJING/B.

4.4.4 $\overline{\Omega^+}/\Omega^-$

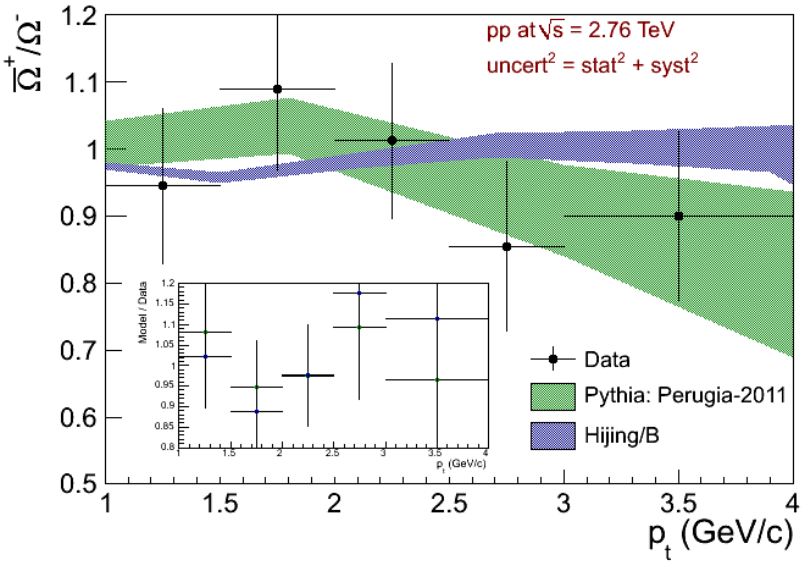

Figure 4.16: $\overline{\Omega^+}/\Omega^-$ ratio as function of transverse momentum at √s = 2.76 TeV. Data points are compared with monte carlo predictions. Inset is showing model over data ratios.

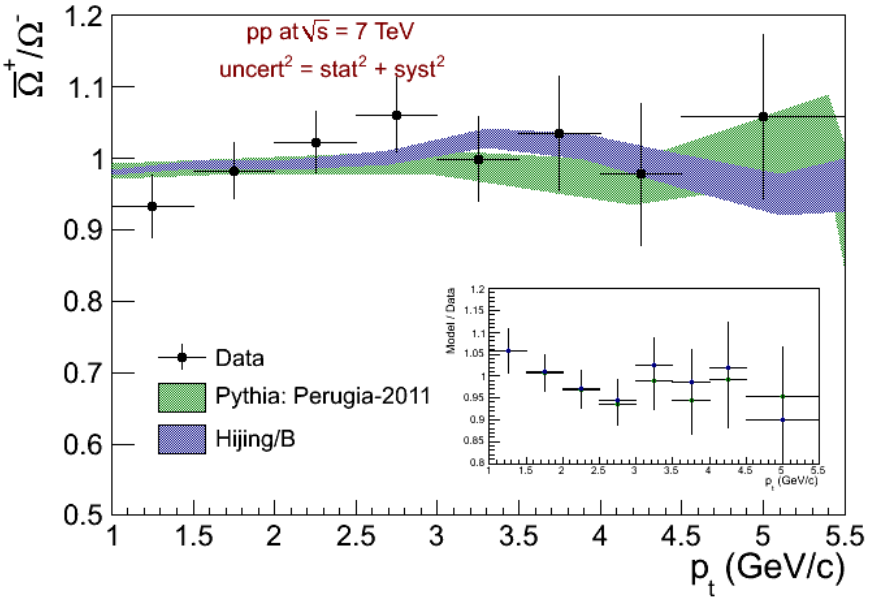

Figure 4.17: $\overline{\Omega^+}/\Omega^-$ ratio as function of transverse momentum at √s = 7 TeV. Data points are compared with monte carlo predictions. Inset is showing model over data ratios.

For $\overline{\Omega^+}/\Omega^-$ ratio we dont see any sign of transverse momentum depenedence. Data points are well described by PYTHA tunes: Atlas-CSC and Perugia-2011 and by HIJING/B.

4.5 Dependence on strangeness and collision energy

4.5.1 Central rapidity ratios

Final corrected antibaryon-to-baryon ratio integrated within the rapidity and transverse momentum phase space for different particle species (see Table 4.13) and √s is summarized in Table 4.9 and Figure 4.18. Comparisons with different Monte Carlo predictions are on Figures 4.19-21.

	p	**Λ**	**Ξ**	**Ω**
900 GeV	0.957±0.006±0.014	0.963±0.006±0.012	0.938±0.028±0.044	No statistics
2.76 TeV	0.975±0.004±0.014	0.979±0.002±0.011	0.982±0.008±0.014	0.964±0.05±0.043
7 TeV	0.991±0.005±0.014	0.989±0.001±0.010	0.992±0.006±0.012	0.997±0.016±0.02

Table 4.9: Central rapidity ratios. Values are integrated in $|y| < 0.5$ for $\bar{p}/p$ and in $|y| < 0.8$ for the rest. Uncertainities corresponds to statistical and systematical ones.

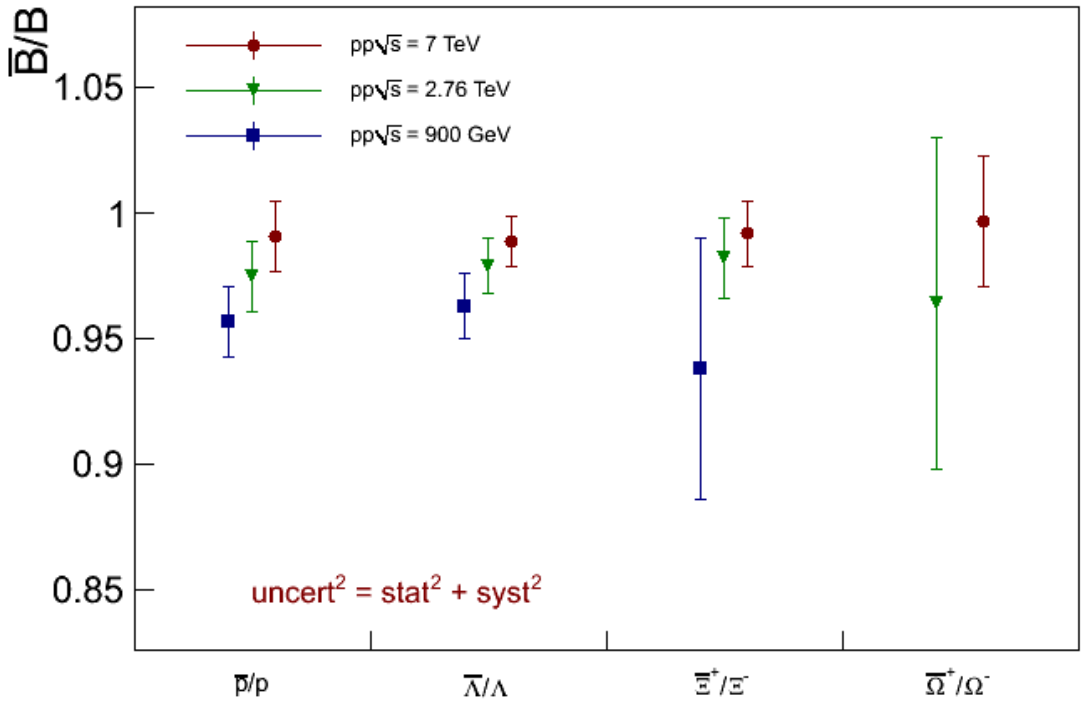

Figure 4.18: Central rapidity ratios. Values are integrated in $|y| < 0.5$ for $\bar{p}/p$ and in $|y| < 0.8$ for the rest.

At 900 GeV and 2.76 TeV we can still see a small excess of baryons over antibaryons for protons, Λ and Ξ (only 2.76 TeV), but at 7 TeV the ratio is compatible with unity for all measured baryons. The ratios at 0.9 and 7 TeV are significantly different for protons Λ and Ξ since the systematic uncertainitites are fully correlated. The fact that ratio at 7 TeV is compatible with unity sets an stringent limit on amouth of transported baryon number over 9 units in rapidity. The existence of large values of antibaryon-to-baryon asymmetry even at infinite energy (A = 0.035 [11]), as was predicted by models using α = 1 for pure gluonic process of baryon number transfer is therefore excluded.

Measured values are compared with various Monte Carlo predictions. All the predictions respesents „standard models“ (α = 0.5) of baryon number transport and are describing the data well.

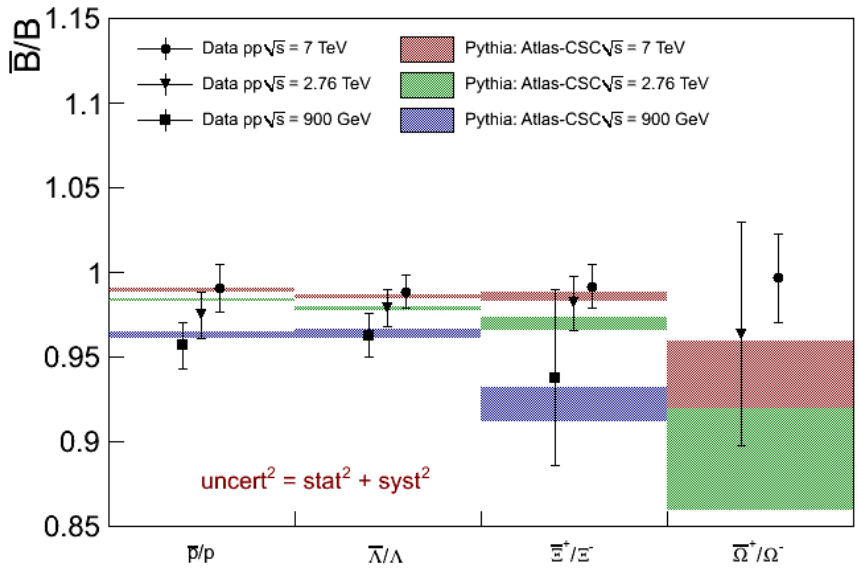

Figure 4.19: Central rapidity ratios. Comparison with PYTHIA: Atlas – CSC. Values are integrated in $|y| < 0.5$ for $\bar{p}/p$ and in $|y| < 0.8$ for the rest.

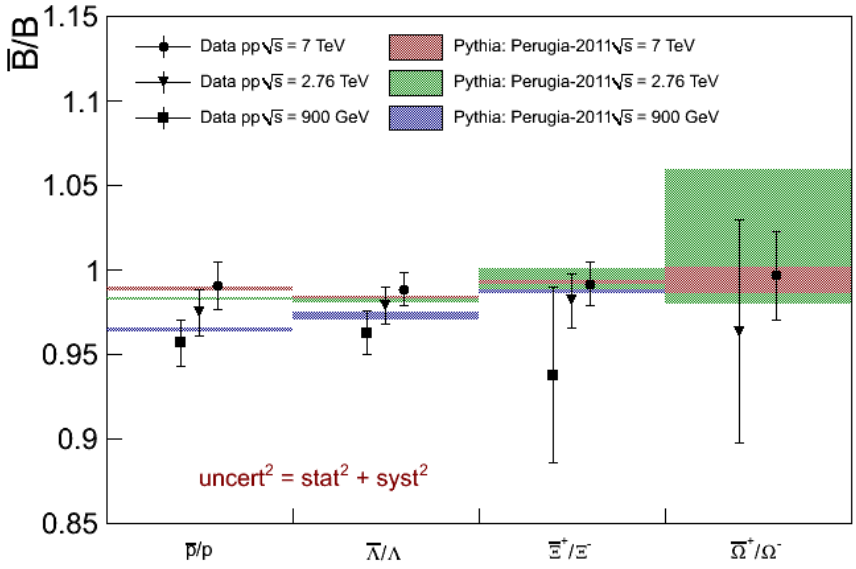

Figure 4.20: Central rapidity ratios. Comparison with PYTHIA: Perugia – 2011. Values are integrated in $|y| < 0.5$ for $\bar{p}/p$ and in $|y| < 0.8$ for the rest.

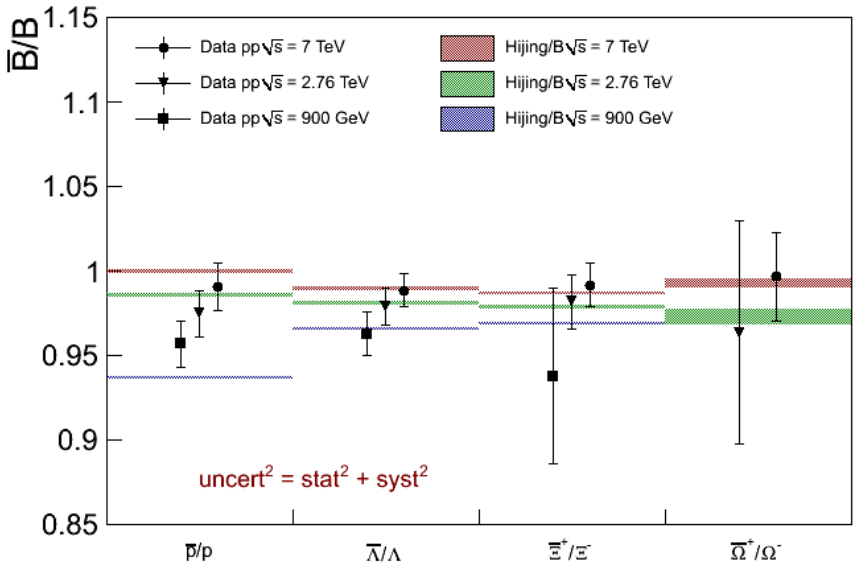

Figure 4.21: Central rapidity ratios. Comparison with HIJING/B (version 2.0). Values are integrated in $|y| < 0.5$ for $\bar{p}/p$ and in $|y| < 0.8$ for the rest.

4.5.2 Rapidity interval dependence

Equivalent consideration as was done in the motivation in section 1.4.1 can be done now with presence of experimental points.

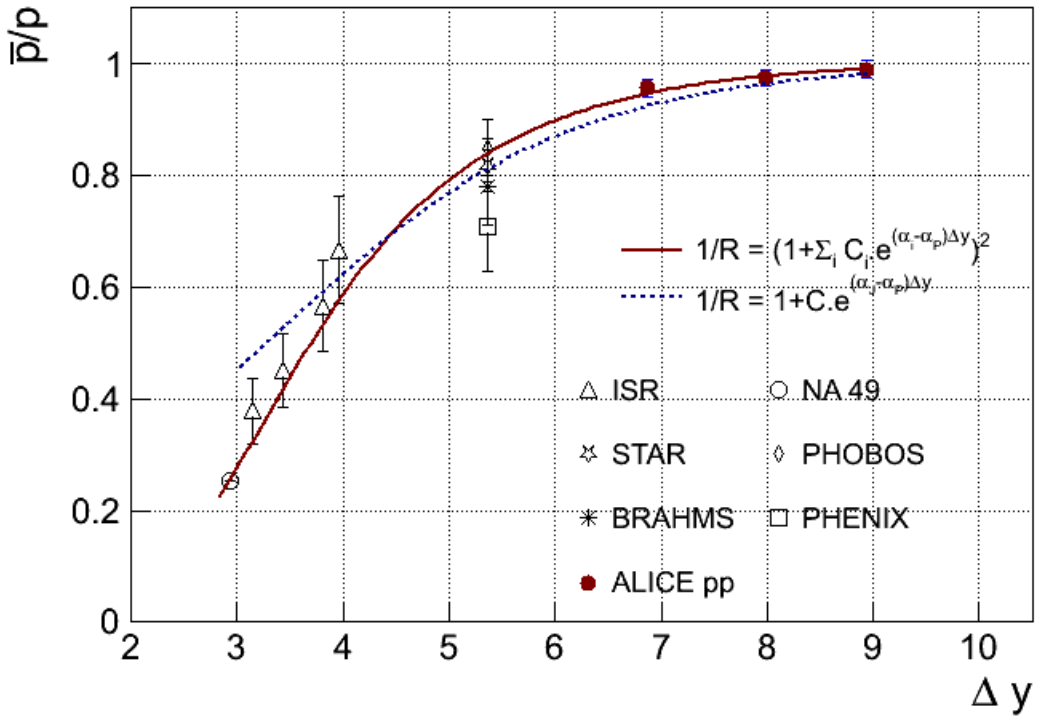

Figure 4.22: Central rapidity $\bar{p}/p$ ratio as a function of rapidity interval Δy. Parametrization using all diagrams (1.18) (red) or only two (1.20) (blue) is shown.

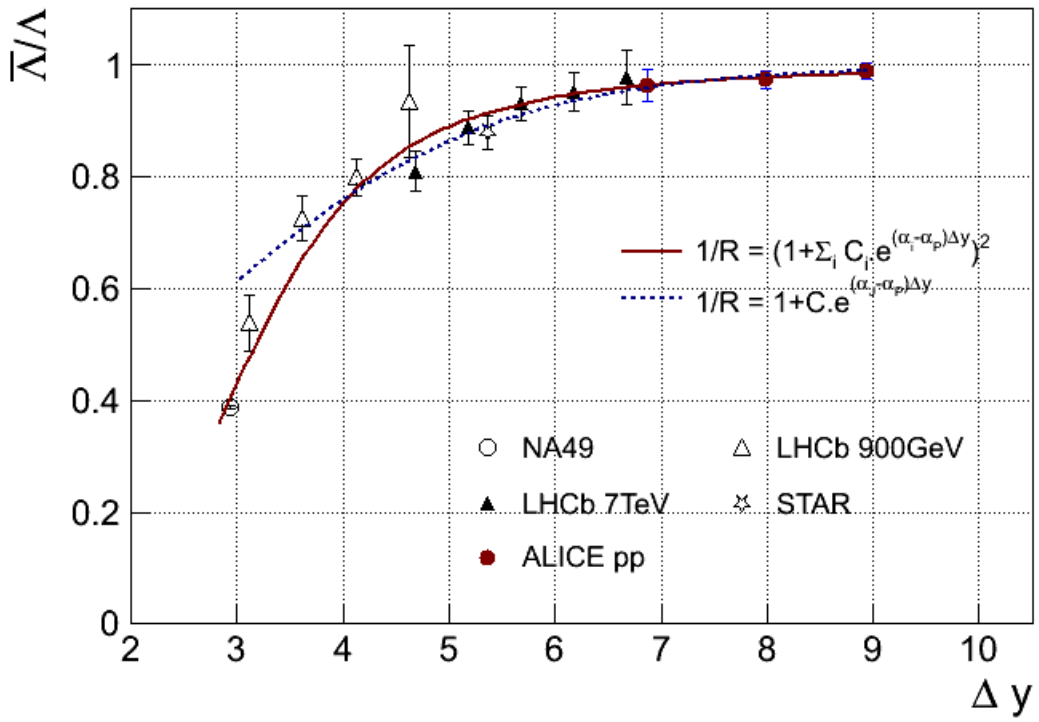

Figure 4.23: Central rapidity $\bar{\Lambda}/\Lambda$ ratio as a function of rapidity interval Δy. Parametrization using all diagrams (1.18) (red) or only two (1.20) (blue) is shown.

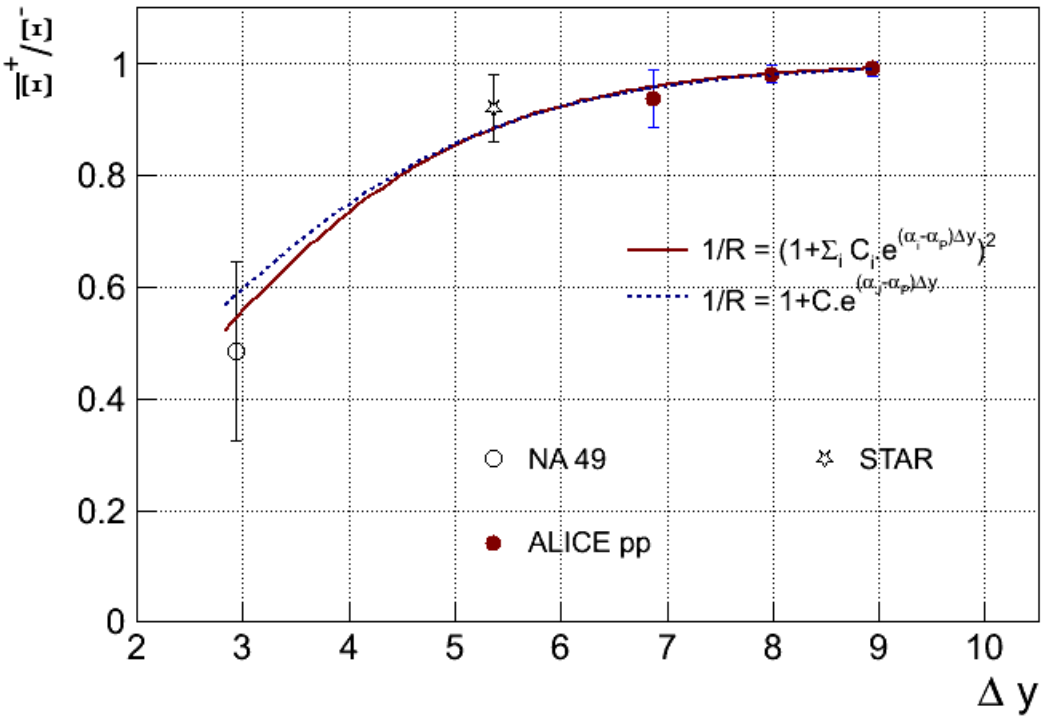

Figure 4.24: Central rapidity $\overline{\Xi^+}/\Xi^-$ ratio as a function of rapidity interval Δy. Parametrization using all diagrams (1.18)(red) or only two (1.20)(blue) is shown.

We can parametrize the rapidity interval dependence of $\bar{p}/p$, $\bar{\Lambda}/\Lambda$ and $\overline{\Xi^+}/\Xi^-$ ratio with presence of our points and previous experimental measurements in proton-proton collisions [18-22] using functions (1.18) and (1.20). The constants that are adjusted to experimental points using pomeron intercept α_p = 1.2 and junction intercepts as summarized in the Table 1.1 are summarized in the Table 4.10 and Table 4.11.

	Diquark-SJ(-1/2)	**Quark-SJ(1/2)**	**SJ itself(1)**
$\bar{p}/p$	81 ± 10	3.35 ± 0.52	0.01 ± 0.03
$\bar{\Lambda}/\Lambda$	50 ± 7	1.78 ± 0.28	0.01 ± 0.02
$\overline{\Xi^+}/\Xi^-$	0(set)	1.97 ± 1.8	0.007 ± 0.05

Table 4.10: Results of parametrization using function (1.18). Constants are corresponding to processes with different junction intercept (value in the bracket) according to configuration in which the baryon number is transported.

	$C(\alpha_J=1/2)$
$\bar{p}/p$	9.91 ± 0.92
$\bar{\Lambda}/\Lambda$	5.20 ± 0.43
$\bar{\Xi}^+/\Xi^-$	4.52 ± 2.28

Table 4.11: Results of parametrization using function (1.20)

As was said already in previous section, the ratio is convergating to unity - is at 7 TeV compatible with unity for all baryon species. This leads to negligibility of the process using α = 1 as can be seen on Table 4.10.

Lets have a look at Figures 4.22-24. The high energy points can be properly decribed also by parameterization (1.20) which is using only process with one junction exchange and value α = ½. We can see that at low energy the contribution of diquarks process cannot be neglected. These points are properly described only by function (1.18) which is including the contribution of diquark-SJ process and also two junction exchange processes. Function (1.18) is missing part of the transport and lies significantly higher then NA49 measurements for protons and Λ.

We can compare the Figure 4.22 with Figures 1.15, 1.16 and see the evolution of antiproton-to-proton ratio is consistent with prediction for α = ½. Measuremed values of antiproton-to-proton ratio at 0.9 and 7 TeV are also consistent with coresponding QGSM prediction for α =0.5 (0.96, 0.99). Prediction for α = 0.9 (0.89, 0.95) is significantly lower then our measurement (see Table 4.9).

We can conclude that

- the process with $\alpha_J = 1$ doesnt improve the quality of the fit, and its contribution is compatible with zero.
- results are consistent with predictions using $\alpha_J = 0.5$ for string junction – itlself configuration
- any significant contribution to antibaryon-to-baryon ratio at central rapidity due to an exchange which is not suppressed with increasing rapidity interval is disfavored
- the process with $\alpha_J = -1/2$ included in parameterization (1.18) does improve the fit at low values of Δy (~3)

4.5.3 Strangeness dependence

We can draw all the parameterizations onto one plot and we can see that it describes also strangeness dependence well. At least for $\bar{p}/p$ and $\bar{\Lambda}/\Lambda$ the functions are well separated. Due to large uncertainity of the paramaterizations of $\overline{\Xi^+}/\Xi^-$ and $\overline{\Omega^+}/\Omega^-$ ratio we cant make any conclusion for multistrange baryons.

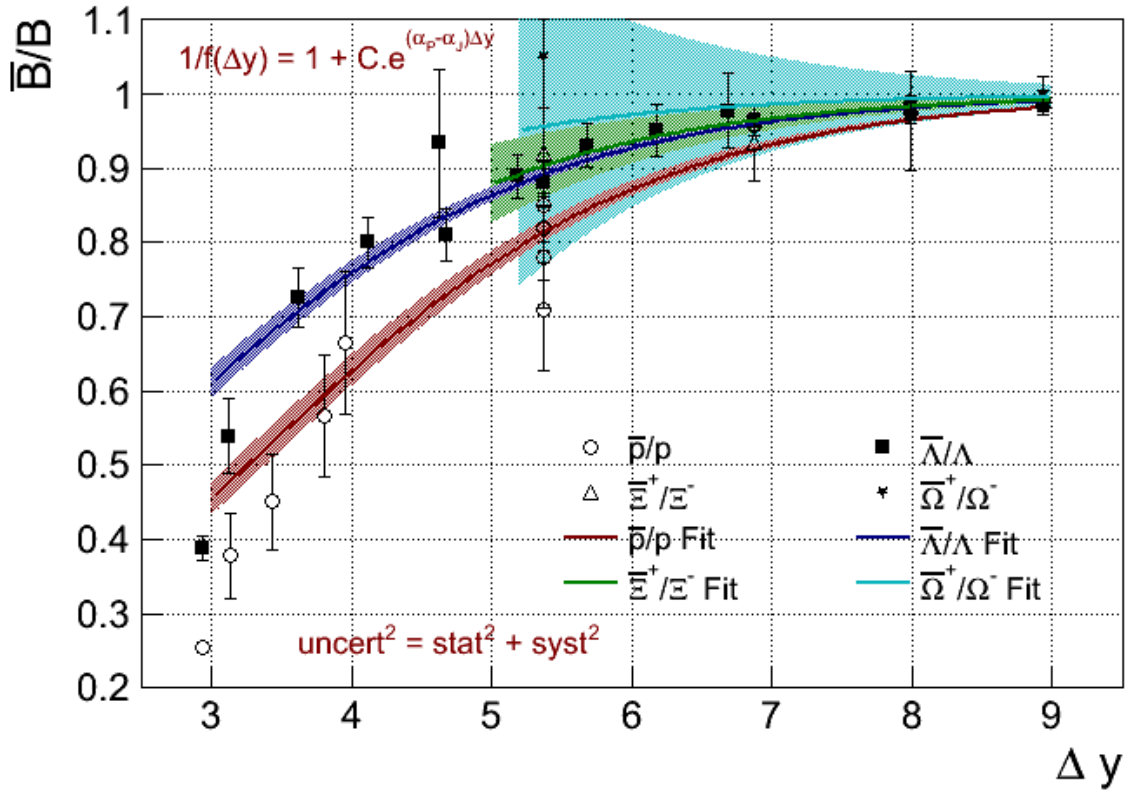

Figure 4.25: Central rapidity ratio as a function of rapidity interval for measured baryons. Parametrization with function (1.20) is showed. Shaded areas around the functions correspond to uncertainity of the function coming from uncertainity of adjusted parameter.

By using the constants from Table 4.10 and Table 4.11 in the following way:

$$R(\Lambda) = \frac{C_{\bar{\Lambda}/\Lambda}}{C_{\bar{p}/p}} \quad \text{or} \quad R(\Xi) = \frac{C_{\overline{\Xi^+}/\Xi^-}}{C_{\bar{p}/p}}$$

we can partially fill the Table 1.2 with experimental results

	Diquark-SJ	QuarkSJ(1.18)	QuarkSJ(1.20)
Λ	*0.62 ± 0.85*	**0.53 ± 0.23**	**0.53 ± 0.21**
Ξ	-	*0.59 ± 0.57*	*0.45 ± 0.3*

Table 4.12: Relative factors for strange baryons with respect to proton for different processes of baryon number transport

The value describing difference between $\bar{p}/p$ and $\bar{\Lambda}/\Lambda$ using functions (1.18) and (1.20) have reasonable uncertainities and are compatible with prediction value 0.6 noted in the Table 1.2. Uncertainities of the other values are too large to give meaningful statement.

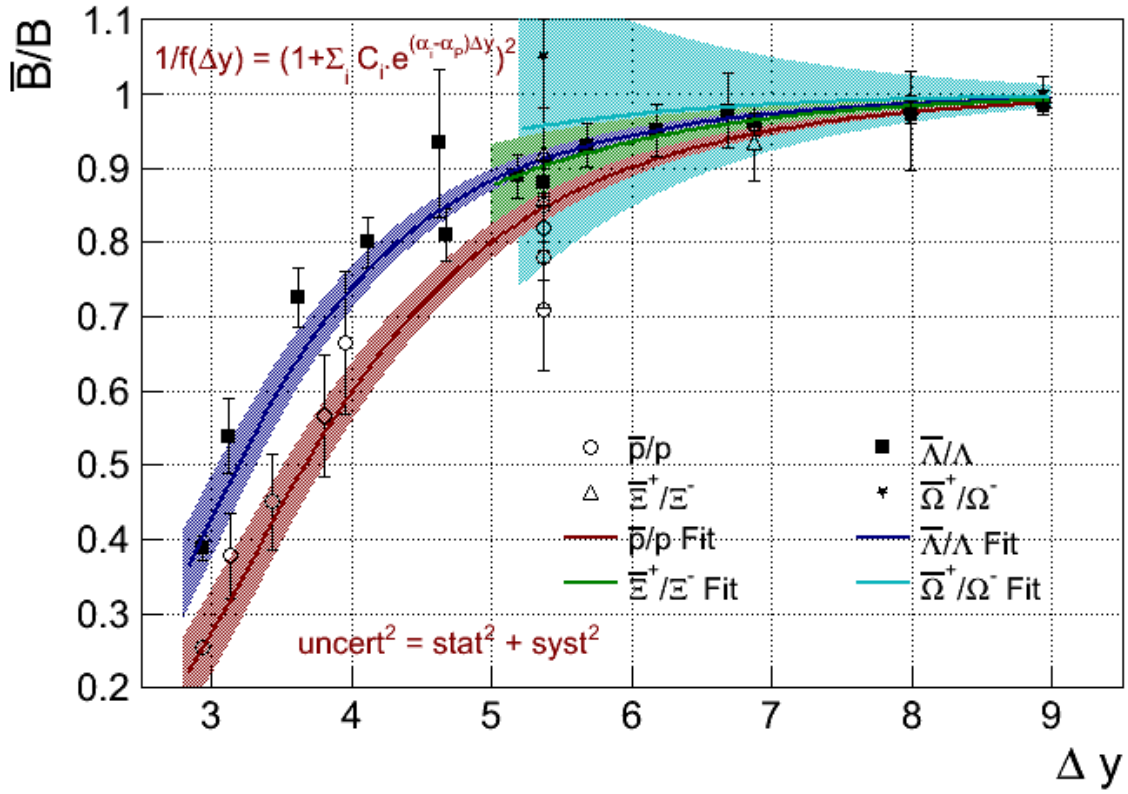

Figure 4.26: Central rapidity ratio as a function of rapidity interval for measured baryons. Parametrization with function (1.18) is showed. Shaded areas around the functions correspond to uncertainity of the function coming from uncertainity of adjusted parameters.

4.6 Multiplicity dependence

Charged particle multiplicity estimator for this measurement is based on the number of ITS standalone tracks + number of tracklets (vectors connecting pair of SPD1 and SPD2 clusters and pointing to vertex within some angular tolerance) for the particles not reconstructed as a full track.

The multiplicity distributions you can find on the Figure 4.27. Distribution is divided into multiplicity bins with respect to reasonable statistics in each bin. The weighted mean and standard deviation σ of the multiplicity distribution in the bin range was set as center and x error bar of a point in multiplicity dependence of the ratio.

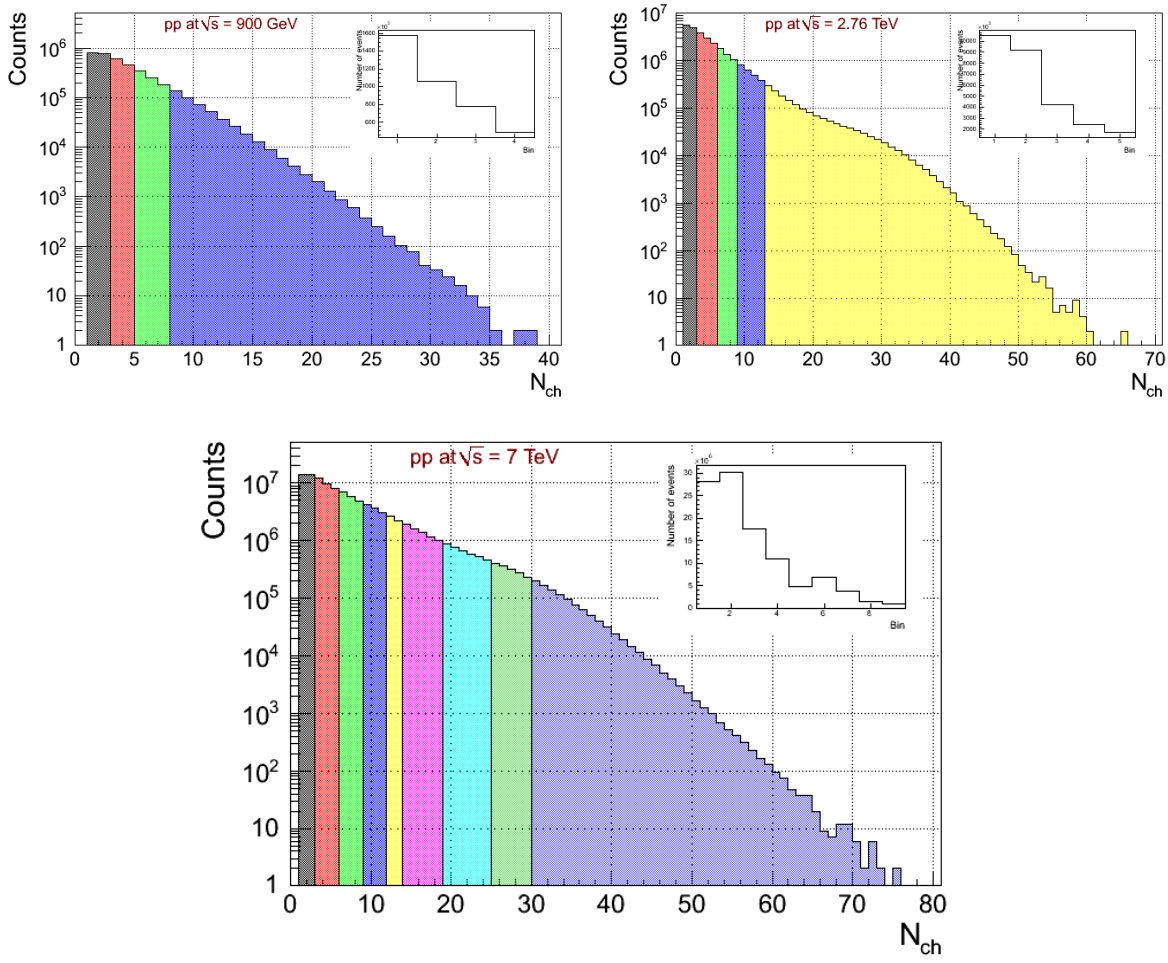

Figure 4.27: Charged particle multiplicity distributions of data sample at √s = 900 GeV (up left), 2.76 TeV (up right) and 7 TeV (down). Distributions are divided into multiplicity bins used in $\bar{p}/p$ ratio analysis. Inset is showing number of events per bin.

4.6.1 $\bar{p}/p$

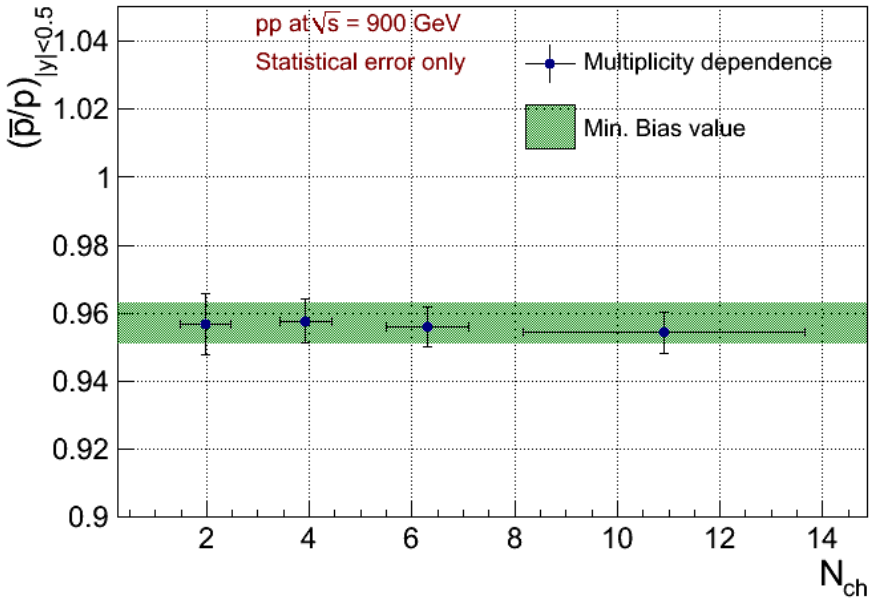

Figure 4.28: $\bar{p}/p$ ratio as function of charged particle multiplicity at $\sqrt{s}$ = 900 GeV. The ratio is calculated for the interval $|y| < 0.5$. The error bars corresponds to statistical ones.

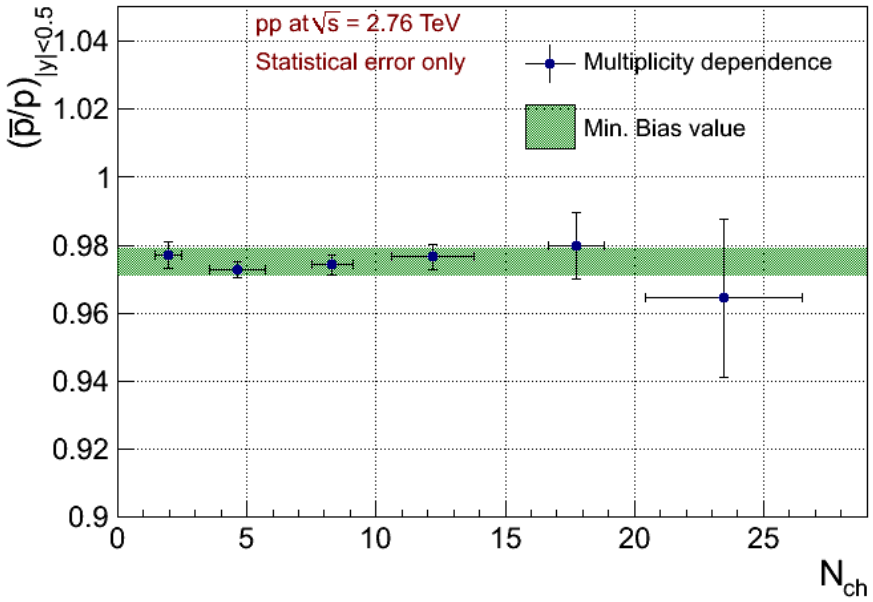

Figure 4.29: $\bar{p}/p$ ratio as function of charged particle multiplicity at $\sqrt{s}$ = 2.76 TeV. The ratio is calculated for the interval $|y| < 0.5$. The error bars corresponds to statistical ones.

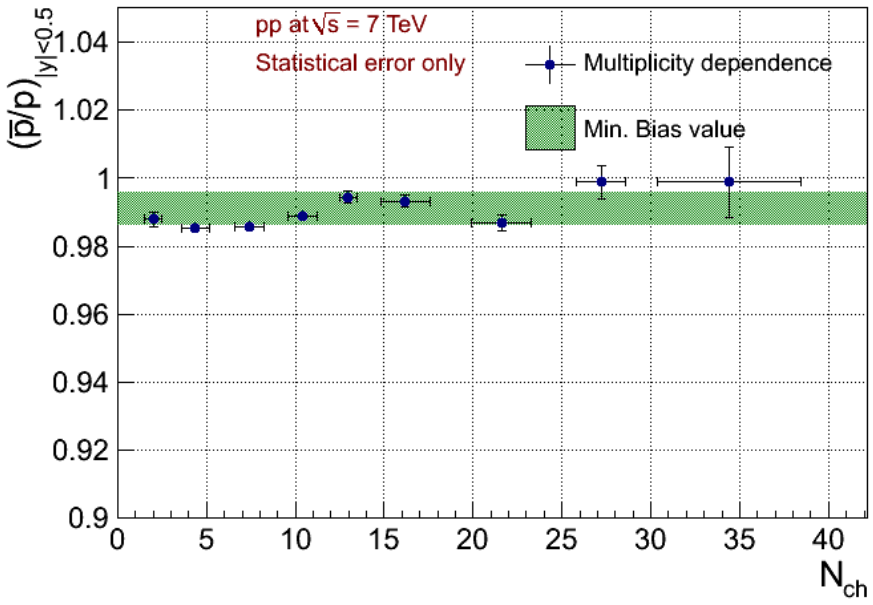

Figure 4.30: $\bar{p}/p$ ratio as function of charged particle multiplicity at $\sqrt{s}$ = 7 TeV. The ratio is calculated for the interval $|y| < 0.5$. The error bars corresponds to statistical ones.

The $\bar{p}/p$ ratio is not showing any sign of charged multiplicity depenedence.

4.6.2 $\bar{\Lambda}/\Lambda$

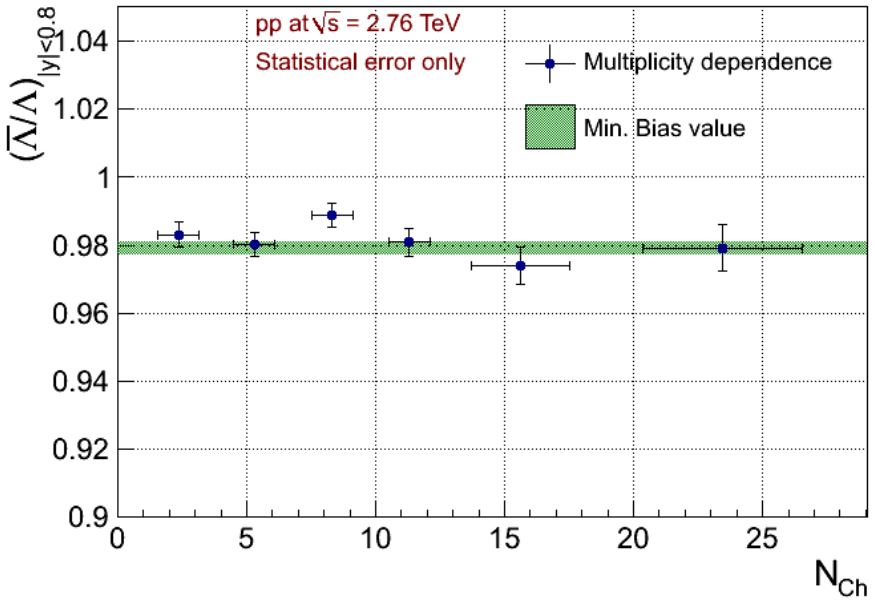

Figure 4.31: $\bar{\Lambda}/\Lambda$ ratio as function of charged particle multiplicity at $\sqrt{s}$ = 2.76 TeV. The ratio is calculated for the interval $|y| < 0.8$. The error bars corresponds to statistical ones.

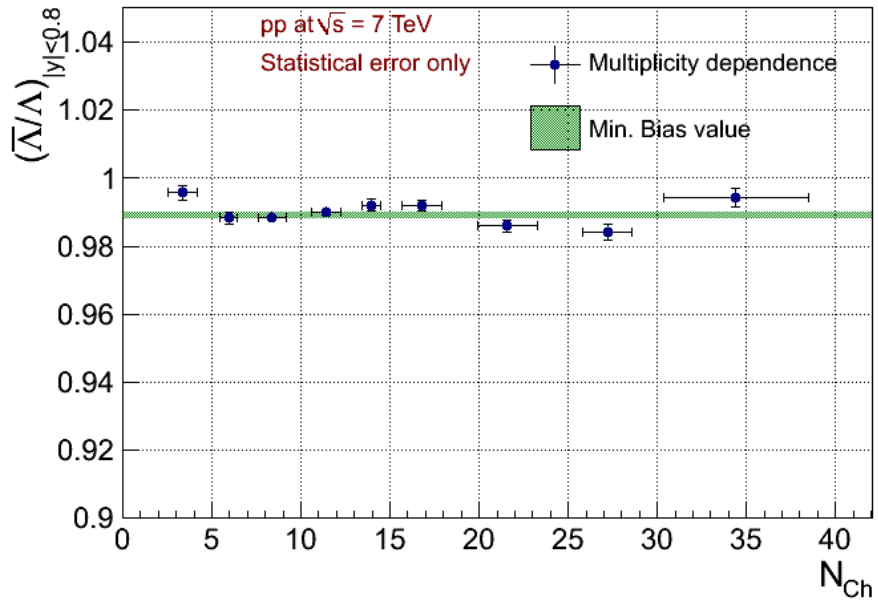

Figure 4.32: $\bar{\Lambda}/\Lambda$ ratio as function of charged particle multiplicity at $\sqrt{s}$ = 7 TeV. The ratio is calculated for the interval |y| < 0.8. The error bars corresponds to statistical ones.

The $\bar{\Lambda}/\Lambda$ ratio is not showing any sign of charged multiplicity depenedence.

4.6.3 $\overline{\Xi^+}/\Xi^-$

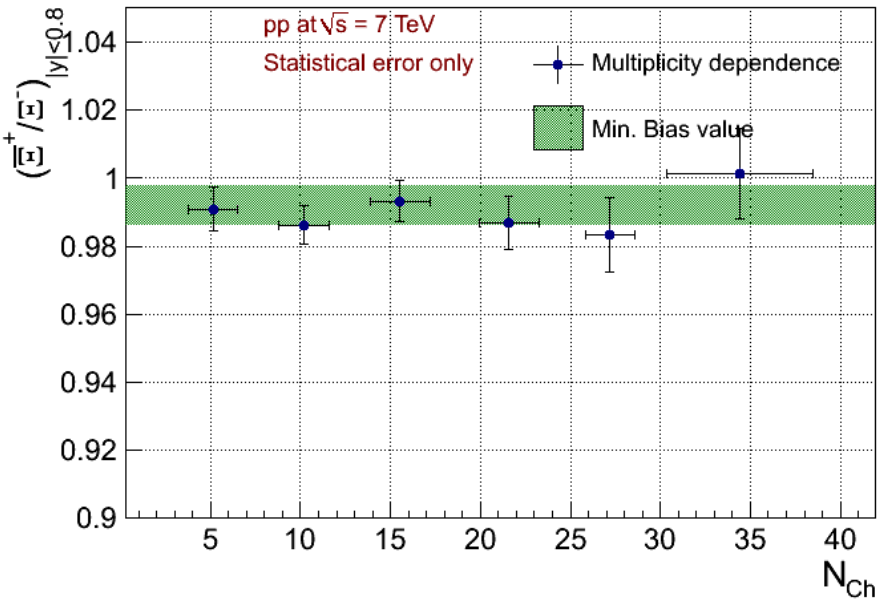

Figure 4.33: $\overline{\Xi^+}/\Xi^-$ ratio as function of charged particle multiplicity at $\sqrt{s}$ = 7 TeV. The ratio is calculated for the interval |y| < 0.8. The error bars corresponds to statistical ones.

The $\overline{\Xi^+}/\Xi^-$ratio is not showing any sign of charged multiplicity depenedence.

4.7 Summary

In summary we report the ratio of the midrapidity anti-baryon to baryon yield for proton, Λ, charged Ξ and charged Ω baryons in proton-proton collisions a √s = 0.9, 2.76 and 7 TeV. Within the fiducial acceptance region (see Table 4.13) the ratio is found to be very close to unity and independent of both rapidity and transverse momentum (see Figure 4.1 – 4.17). We don't see any sign of charged multiplicity dependence too (see Figure 4.28 – 4.33).

	√s (TeV)	**p**	**Λ**	**Ξ**	**Ω**
y	0.9 – 2.76 – 7	0.5		0.8	
p_t (GeV/c)	0.9	0.45 – 1.05	0.5-4.0	0.5-3.5	-
	2.76		0.5-4.5	0.5-4.5	1.0-4.0
	7		0.5-10.5	0.5-5.5	1.0-5.5

Table 4.13: Fiducial acceptance region

At 900 GeV we still see small excess of baryons over antibaryons for protons, Λ and Ξ. At 2.76 TeV the excess is even smaller and significant only for protons and Λ. At 7 TeV ratio is compatible with unity for all analyzed baryon species (see Figure 4.18 and Table 4.9). Antibaryon – to baryon ratio is rising with collision energy and converging to unity at 7 TeV for all baryon species (see Figure 4.25 and 4.26). Results are consistent with model predictions using for the baryon-number transport a t-channel exchange with the Regge-trajectory intercept of $\alpha_J \approx 0.5$. Any significant contribution to baryon–antibaryon asymmetry at central rapidity due to an exchange, which is not suppressed with increasing rapidity interval ($\alpha_J \approx 1$), is disfavored. In another words results are consistent with standard models ($\alpha_J \approx 0.5$) of baryon-number transport and set tight limits on any additional contributions to baryon-number transfer over very large rapidity intervals in proton – proton collisions.

Conclusion

In this thesis I presented the results of the study of antibaryon-to-baryon ratio in proton-proton collisions measured by ALICE experiment.

Two models of baryon structure representing two possibilities of carrier of baryon number were presented. By using parametrization of central rapidity ratio as a function of rapidity interval (1.18) derived in this thesis (generalization of a function used in dedicated ALICE paper [17]) I can disclaim the composite quark model with respect to previous experimental results from RHIC [20] (see Figure 1.13). The new results from ALICE experiment only strengthen this argument (see Figure 4.22). Parametrization outgoing from string junction model is describing the data well (see Figure 1.14 and 4.22 – 4.24). The baryon number is carried rather by string junction then by valence quarks.

In this analysis, due to symetricity of the experiment which leads to the fact that many detector effects such as the acceptance, the reconstruction and the particle identification ones are the same for particles and anti-particles and thus cancel out in the ratio, I am applying correction only for the particle-antiparticle asymmetric effects. This leads to decrease of the systematic uncertainty and better precision of the measurement.

I analyzed the data of proton-proton collisions at three LHC energies $\sqrt{s}$ = 900 GeV, 2.76 and 7 TeV. In particular the rapidity, transverse momentum and charged particle multiplicity dependencies of antibaryon-to-baryon ratio are presented. On the top of this, strangeness and rapidity interval dependence of the central rapidity ratio was investigated. Data points were compared with several Monte Carlo predictions. Central rapidity ratios, with participation of previous experimental results were parameterized as a function of rapidity interval and strangeness using functions derived in chapter 1. Using the parameterization derived in this thesis I can properly describe rapidity interval dependence and partially describe strangeness dependence of central rapidity ratio.

The main conclusions implied by results of this thesis are:

- Within the fiducial acceptance region (see Table 4.11) the $\bar{p}/p$, $\overline{\Lambda}/\Lambda$, $\overline{\Xi^+}/\Xi^-$ and $\overline{\Omega^+}/\Omega^-$ ratio is found to be very close to unity and independent of rapidity,

transverse momentum (see Figure 4.1 – 4.17) and charged particle multiplicity (see Figure 4.28 – 4.33).

- At $\sqrt{s}$ = 900 GeV we see small excess of baryons over antibaryons for protons, Λ and charged Ξ. At $\sqrt{s}$ = 2.76 TeV we still see small excess of baryons over antibaryons for protons and Λ. At 7 TeV ratio is compatible with unity for all analyzed baryon species (see Figure 4.18 and Table 4.9).
- Antibaryon – to baryon ratio is rising with collision energy and converging to unity at 7 TeV for all baryon species (see Figure 4.25 and 4.26).
- Any significant contribution to baryon-antibaryon asymmetry at central rapidity due to an exchange, which is not suppressed with increasing rapidity interval ($\alpha_J \approx 1$), is disfavored.
- Results are consistent with standard models of baryon-number transport ($\alpha_J \approx 0.5$) and set tight limits on any additional contributions to baryon-number transfer over very large rapidity intervals in proton – proton collisions.
- Rapidity interval dependence of antibaryon-to-baryon ratio can be well described by Regge model inspired parameterizations (1.18) in whole Δy range (see Figure 4.25).
- Strangeness dependence of the ratio can be partially described (with respect to the uncertainties) by Regge model inspired parameterizations (1.18) and (1.20) of baryon asymmetry (see Figure 4.25 and 4.26).

Preliminary results of the analysis were presented on several international conferences and published in the conference proceedings. Notably I presented the preliminary results on conference "Physics at LHC (PLHC)" 2010 in Hamburg and 2011 in Perugia. Part of the results, transverse momentum dependence of the $\bar{p}/p$ ratio at $\sqrt{s}$ = 900 GeV and 7 TeV and parameterization of rapidity interval dependence of $\bar{p}/p$ ratio using function (1.20), was published in Physics Review Letters [17]. In the present time we are working on publication dedicated to the rest of the results showed in this thesis.

References

[1] A. Casher, H. Neuberger and S. Nussinov, Phys. Rev. **D20** (1980) 179

[2] B. Baier et al., Nucl. Phys. **B484** (1997) 265

[3] M. Vasiliev et al., Phys. Rev. Lett. **83** (1999) 2304

[4] D. B. Lichtenberg and L. J. Tassie, Phys. Rev. **155**, 1601 (1967)

[5] M. Imachi, S.Otsuki, and F. Toyoda, Prog. Theor. Phys. **52**, 341 (1974)

[6] X. Artru, Nucl. Phys. **B85** (1975) 442

[7] E. Gotsman and S. Nussinov, Phys. Rev. **D 22** (1980) 624

[8] A. Capella et al., Phys. Rep. **236**, 225 (1994);

[9] A.B.Kaidalov and K. A. Ter-Martirosyan, Sov. J. Nucl. Phys.**39**, 1545 (1984).

[10] G. C. Rossi and G. Veneziano, Nucl. Phys. **B123**, 507 (1977).

[11] B. Z. Kopeliovich, Sov. J. Nucl. Phys. **45**, 1078 (1987);

[12] B. Z. Kopeliovich and B. Povh, Z. Phys. **C 75**, 693 (1997);
Phys. Lett. **B 446**, 321 (1999).

[13] D. Kharzeev, Phys. Lett. **B 378**, 238 (1996).

[14] C. Merino et al., Eur. Phys. J. **C 54**, 577 (2008);
C.Merino, M. M. Ryzhinskiy, and Yu. M. Shabelski, arXiv:0906.2659.

[15] S. E. Vance and M. Gyulassy, Phys. Rev. Lett. **83**, 1735 (1999).

[16] A. B. Kaidalov, L. A. Ponomarev, and K. A. Ter-Martirosyan, Sov. J. Nucl. Phys. **44**, 468 (1986).

[17] ALICE collaboration: Phys. Rev. Lett. **105**, 072002 (2010

[18] T. Anticic et al. (NA49 Collaboration), Eur. Phys. J. C **65**, 9 (2010).
T. Susa et al. (NA49 Collaboration), Nucl.Phys. A**698** (2002) 491-494

[19] A. M. Rossi et al., Nucl. Phys. **B84**, 269 (1975);
M.Aguilar-Benitez et al., Z. Phys. **C 50**, 405 (1991).

[20] B. I. Abelev et al. (STAR Collaboration), Phys. Rev. **C 79**, 034909 (2009);
I.G. Bearden et al. (BRAHMS Collaboration), Phys. Lett. **B 607**, 42 (2005); B.B. Back et al. (PHOBOS Collaboration), Phys. Rev. **C 71**, 021901 (2005);
S. S. Adler et al. (PHENIX Collaboration), Phys. Rev. **C 69**, 034909 (2004).

[21] B. I. Abelev et al. (STAR Collaboration), Phys. Rev. C **75** (2007) 64901

[22] LHCb collaboration: JHEP08(2011)034

[23] P. D. B. Collins, An Introduction to Regge Theory and High Energy Physics

(Cambridge University Press, Cambridge, England, 1977).

[24] ALICE Collaboration: Technical Design Report of the Inner Tracking System. 1999

[25] ALICE Collaboration: Technical Design Report of the Time-Projection Chamber. 2000.

[26] ALICE Collaboration: Technical Design Report of the Time-Of-Flight Detector. 2000.

[27] ALICE Collaboration: Technical Design Report of the Transition-Radiation Detector. 2001.

[28] ALICE Collaboration: Technical Design Report of the High-Momentum Particle Identification Detector. 1998.

[29] ALICE Collaboration: Technical Design Report of the Photon Spectrometer. 1999.

[30] ALICE Collaboration: TechnicalDesign Report of the Forward Detectors. 2004.

[31] ALICE Collaboration : Physics Performance Report, Volume I J. Phys. G: Nucl. Part. Phys. 30 (2004) 1517-1763

[32] ALICE Collaboration : Physics Performance Report, Volume II J. Phys. G: Nucl. Part. Phys. 32 (2006) 1295-2040

[33] Billoir P 1984 Nucl. Instrum. Methods **A 225** 352

[34] W. Blum et al., Particle Detection with Drift Chambers, 2nd ed., Springer Verlag, 2008.

[35] ALICE Collaboration: Eur. Phys. J. C (2011) **71**: 1594

[36] R. Brun et al., GEANT3 User Guide (CERN Data Handling Division DD/EE/841, 1985);
R. Brun et al., CERN Program Library Long Write-up, W5013, GEANT Detector Description and Simulation Tool, 1994.

[37] A. Fasso et al., CERN-2005-10, INFN/TC05/11, SLAC-R-773 (2005);
G. Battistoni et al., AIP Conf. Proc. **896**, 31 (2007).

[38] G. Bendiscioli and D. Kharzeev, Riv. Nuovo Cimento Soc.Ital. Fis. 17, 1 (1994);
R. F. Carlson, At. Data Nucl. Data Tables 63, 93 (1996).

[39] P. Christakoglou, ALICE Internal Note Report No. ALICE-INT-2010-006, 2010.

[40] B. Sitar, G.I. Merson, V.A. Chechin, Yu.A. Budagov (1988) Ionization Measurements in High Energy Physics. Springer-Verlag (1993), 121